University of Alberta

Deterministic and Stochastic Models of Drug Transport and Reaction Kinetics in Heterogeneous Media

by

Rebeccah E. Marsh

A thesis submitted to the Faculty of Graduate Studies and Research in partial fulfillment of the requirements for the degree of Doctor of Philosophy

Department of Physics

Edmonton, Alberta
Spring 2007

Library and Archives Canada

Published Heritage Branch

395 Wellington Street
Ottawa ON K1A 0N4
Canada

Bibliothèque et Archives Canada

Direction du Patrimoine de l'édition

395, rue Wellington
Ottawa ON K1A 0N4
Canada

Your file Votre référence
ISBN: 978-0-494-29709-4
Our file Notre référence
ISBN: 978-0-494-29709-4

NOTICE:
The author has granted a non-exclusive license allowing Library and Archives Canada to reproduce, publish, archive, preserve, conserve, communicate to the public by telecommunication or on the Internet, loan, distribute and sell theses worldwide, for commercial or non-commercial purposes, in microform, paper, electronic and/or any other formats.

The author retains copyright ownership and moral rights in this thesis. Neither the thesis nor substantial extracts from it may be printed or otherwise reproduced without the author's permission.

AVIS:
L'auteur a accordé une licence non exclusive permettant à la Bibliothèque et Archives Canada de reproduire, publier, archiver, sauvegarder, conserver, transmettre au public par télécommunication ou par l'Internet, prêter, distribuer et vendre des thèses partout dans le monde, à des fins commerciales ou autres, sur support microforme, papier, électronique et/ou autres formats.

L'auteur conserve la propriété du droit d'auteur et des droits moraux qui protège cette thèse. Ni la thèse ni des extraits substantiels de celle-ci ne doivent être imprimés ou autrement reproduits sans son autorisation.

In compliance with the Canadian Privacy Act some supporting forms may have been removed from this thesis.

While these forms may be included in the document page count, their removal does not represent any loss of content from the thesis.

Conformément à la loi canadienne sur la protection de la vie privée, quelques formulaires secondaires ont été enlevés de cette thèse.

Bien que ces formulaires aient inclus dans la pagination, il n'y aura aucun contenu manquant.

Canada

Abstract

Pharmacokinetics describes the course of a drug through the body and is the main quantitative tool used in all stages of drug discovery, development, and administration. Most pharmacokinetic models are based on the assumption that drug transport and reaction kinetics occur in a homogenous environment. However, the spaces in the body are usually confined and heterogeneous. Consequently, the transport and chemical reaction processes occurring within them can become anomalous. Evidence of this result includes emergent power law behaviour. The objective of this thesis is to apply concepts from physics to develop more physiologically-accurate models of drug processes occurring in the body in the presence of spatial and/or temporal heterogeneity.

Several complementary models were developed to investigate drug elimination kinetics in a heterogeneous environment. Fractal drug kinetics under Michaelis-Menten conditions was developed and implemented using a continuous, deterministic fractal compartmental model. Using a parameter optimization method based on a simulated annealing algorithm, the model was found to provide an improved fit to experimental data for the cardiac drug mibefradil.

The theory of fractal elimination kinetics was then tested using a stochastic method based on an interacting random walk model. It was found that short-term correlations between drug molecules produced Michaelis-Menten elimination kinetics while long-term correlations produced fractal kinetics. By combining both effects, the fractal Michaelis-Menten theory was reproduced. The model was then expanded into a continuous time random walk model to include the effects of temporal heterogeneity in the form of Lévy-distributed long-time trapping of drug molecules in temporary traps.

Power law behaviour does not always indicate fractal kinetics. A two-compartment model for the anticancer drug paclitaxel was used to demonstrate that it can be produced by the competition between two saturable processes. The power exponent of the long-time tail of the concentration-time curve was correlated with the power exponent

describing the nonlinear dose-dependence of two pharmacokinetic measures.

Finally, a physiologically-based flow network model was used to show that the organ-level dynamics of drug metabolism can be reproduced at the level of the functional unit of the liver. Different types of spatial heterogeneity that mimicked pathological conditions were found to lead to either fractal or fractal Michaelis-Menten kinetics.

Acknowledgements

Many people contributed encouragement and assistance throughout this process. I would like to thank my supervisor Dr. Jack Tuszyński for his unfailing support, generosity, and willingness to work around my unusual circumstances. This work was supported in part through his Mathematics of Information Technology and Complex Systems (MITACS) Mathematical Modeling in Pharmaceutical Development (MMPD) project. I would also like to thank my co-supervisor Dr. Terry Riauka for his guidance and for sharing his programming expertise. In addition, my committee members Drs. Massimo Bonensegni, Steve McQuarrie, and Michael Sawyer all provided helpful input. I would especially like to thank Dr. Michael Sawyer as well as Drs. Chris Takimoto and Eric Rowinsky for providing clinical data sets.

The work in Chapter 8 was performed as part of a Mathematics of Information Technology and Complex Systems (MITACS) Industrial Internship. I would like to thank both MITACS for its support and my industrial supervisor Dr. Dennis Coombe for his collaboration and always stimulating conversation.

A special acknowledgement goes to Jennifer Zelmer, who saw this thesis through from beginning to end and patiently provided support and guidance throughout. Also, Diane Symbaluk was instrumental in keeping me focused. Finally, I'd like to thank Ken Bird, for supporting me in so many ways and for believing in me.

Table of Contents

1 Introduction 1
- 1.1 Challenges to Pharmacokinetic Modeling . . . 2
- 1.2 The Role of Physics . . . 2
- 1.3 Hypothesis . . . 3
- 1.4 Original Contributions . . . 4
- 1.5 Organization of the Thesis . . . 5

2 Basic Concepts in Pharmacokinetics 6
- 2.1 Plasma Concentration-Time Curves . . . 6
- 2.2 Pharmacokinetic Parameters . . . 8
- 2.3 Pharmacokinetic Models . . . 9
  - 2.3.1 Compartmental Models . . . 10
  - 2.3.2 Non-Compartmental Models . . . 13
  - 2.3.3 Stochastic Pharmacokinetic Models . . . 14
- 2.4 Nonlinear Pharmacokinetics . . . 15
  - 2.4.1 Michaelis-Menten Kinetics . . . 16
- 2.5 Transient Fractal Kinetics . . . 19
- 2.6 Power Laws and Scaling in Pharmacokinetics . . . 21
  - 2.6.1 Clearance Curves . . . 22
  - 2.6.2 Nonlinear Dose-Dependence . . . 23
  - 2.6.3 Allometric Scaling . . . 23

3 A Parameter Optimization Method Using a Simulated Annealing Algorithm 25
- 3.1 Purpose . . . 25
- 3.2 Background . . . 25
- 3.3 Simulated Annealing Algorithm . . . 26
- 3.4 Methods . . . 29
  - 3.4.1 The PKPhit Program . . . 29
  - 3.4.2 Annealing Schedule . . . 30
  - 3.4.3 Test Models . . . 31
  - 3.4.4 Simulated Data Sets . . . 33
- 3.5 Results . . . 35
  - 3.5.1 Optimum Algorithm Parameters . . . 35
  - 3.5.2 Comparison With Other Algorithms . . . 39

3.5.3 Applicability to Fractal models 41
3.6 Conclusion 42

4 Emergence of Power Laws from Competing Saturable Processes 44
4.1 Purpose 44
4.2 Background 44
4.3 Hypothesis 46
4.4 Methods 46
4.5 Results 48
4.5.1 Power Law Tails 48
4.5.2 Power Law Dose Dependence 51
4.5.3 Simulations 52
4.6 Discussion 59
4.7 Conclusion 59

5 Fractal Michaelis-Menten Kinetics Under Steady State Conditions 61
5.1 Purpose 61
5.2 Background 61
5.2.1 Steady State Fractal Kinetics 62
5.3 Model 64
5.3.1 Asymptotic Behaviour 65
5.4 Methods 66
5.5 Results 67
5.6 Discussion 71
5.7 Conclusion 73

6 Interacting Random Walk Model 74
6.1 Purpose 74
6.2 Model 74
6.3 Reproducing Elimination Kinetics 77
6.3.1 Michaelis-Menten kinetics 77
6.3.2 Fractal-like kinetics 81
6.3.3 Fractal-like Michaelis-Menten kinetics 85
6.3.4 Infusion curves 88
6.4 Conclusion 91

7 Continuous Time Random Walk Model With Lévy Flights 92
7.1 Purpose 92
7.2 Background 92
7.2.1 Temporary Binding of Drug Molecules 93
7.2.2 Lévy Distributions 94
7.2.3 Lévy Flights 98
7.3 Relevance of Lévy Distributions to Pharmacokinetics 99
7.3.1 Continuous time random walks 100
7.4 Model 101
7.5 Method 103

7.6 Results . . . 104
7.6.1 Effect of Lévy-distributed Traps . . . 104
7.6.2 Sensitivity of the Power Exponent . . . 106
7.6.3 Temporary Versus Permanent Trapping . . . 107
7.6.4 Effect of the Elimination Kinetics . . . 109
7.6.5 Predicting the Dose to the Target . . . 112
7.6.6 Infusion curves . . . 115
7.7 Discussion . . . 119
7.8 Conclusion . . . 120

8 Physiologically-Based Flow Network Model for Drug Elimination 121
8.1 Purpose . . . 121
8.2 Background . . . 121
8.2.1 Liver Architecture . . . 121
8.2.2 Functional Unit . . . 122
8.2.3 Diseased states . . . 123
8.2.4 Network Models of the Liver . . . 124
8.3 Model and Methods . . . 125
8.4 Results . . . 128
8.4.1 Regular Lattice . . . 128
8.4.2 Random Permeability Lattice . . . 132
8.4.3 Percolation Lattice . . . 139
8.5 Conclusion . . . 144

9 Conclusion 145
9.1 Summary . . . 145
9.2 Future Directions . . . 146

A Fractals 166
A.1 Definition . . . 166
A.2 Examples . . . 168
A.3 The Fractal Dimension . . . 170
A.4 Fractals in Anatomy and Physiology . . . 174

List of Tables

3.1 Theoretical coefficients for the simulated two-compartment models. 34
3.2 Annealing schedule. 37
3.3 Initial parameter values. 37
3.4 Estimated parameters for the classical two-compartment model. The input parameters necessary for the Gauss-Newton and simplex algorithms are listed in Table 3.5. 40
3.5 Initial and bounding parameter values necessary for the Gauss-Newton and simplex algorithms to achieve the accuracy shown in Table 3.4. 40
3.6 Estimated parameters for Model 2 with fractal trapping. 41
3.7 Estimated parameters for Model 3 with fractal elimination. 42

4.1 Mean population values reported by Kearns et al. [88] for the three-compartment model parameters. 48
4.2 The power law exponent α quantifying the tail of paclitaxel concentration-time curves. 49
4.3 The power law exponent β quantifying the dose dependence of pharmacokinetics parameters for 1-h paclitaxel infusions. 52
4.4 The power law exponent β describing the graphs in Fig. 4.6. 56

5.1 Summary of models for the enzyme-mediated kinetics of drug elimination. 67
5.2 The slope γ of the log(concentration) versus log(time) curve between $t =$ 30 min and $t = 1440$ min. Values are given as mean (standard deviation). 67
5.3 One-compartment parameters for the drug concentration in the jugular vein of dogs following a 10-min infusion of 1 mg/kg of mibefradil. 69
5.4 Comparison between the values for the fractal reaction order X predicted from the slope γ and obtained from the model fit. 71

7.1 Lévy distribution parameters 102
7.2 Power law tail exponent between $x = 0$ and $x = 3000$ for the distribution of values drawn randomly from the quantiles for $\alpha = 1.4$. 103
7.3 Power exponent γ for drug molecules undergoing simple elimination and Lévy trapping with different values of α. 104
7.4 The power exponent for $\alpha = 1.6$ as a function of the Lévy scale, σ. 106
7.5 The mean power exponent γ and standard deviation as a function of the number of values. 106

7.6 The mean power exponent γ and standard deviation as a function of the lattice size, L. 107
7.7 Power law exponent for Lévy trapping with $\alpha = 1{,}6$ with simple elimination, for different relative strengths of the temporary and permanent trapping. 107
7.8 Pharmacokinetic parameters. 113

8.1 Anatomical values for the liver. 123
8.2 Flow rate as a function of the σ for a random permeability lattice. 133
8.3 Effect of the standard deviation σ of the permeability on the shape of the molar fraction of PAC-OH curve. 137
8.4 Flow rate as a function of the σ for a percolation lattice. 139
8.5 Effect of p on the shape of the molar fraction of PAC-OH curve. 143

9.1 Summary of models. 145

List of Figures

2.1 An example of a plasma concentration-time curve for a drug undergoing absorption, distribution, metabolism, and elimination in the body following an intravenous infusion. 7

2.2 Enzyme-mediated reaction. E, S, ES, and P represent the enzyme, substrate, enzyme-substrate complex, and product, respectively 17

2.3 (a) Velocity v of a Michaelis-Menten reaction as a function of the reactant concentration, where $v_{\max}$ is the maximum rate of the reaction. (b) Lineweaver-Burk plot, where C is the drug concentration and K_M is the Michaelis-Menten constant. 17

3.1 The simulated annealing algorithm. The operator mod (x_1, x_2) returns the remainder of x_1 divided by x_2. 28

3.2 A two-compartment mamillary model. 32

3.3 A two-compartment catenary model. 33

3.4 The simulated data sets for (a) Model 1, (b) Model 2, and (c) Model 3. . 36

4.1 A compartment model with both saturable distribution to compartment 2 and saturable elimination from compartment 1, as well as an optional linear binding compartment 3. 47

4.2 Pharmacokinetic data obtained for 3-h infusions of paclitaxel, replotted from Kearns et al. [88] for three dose levels (open circles, 135 mg/m^2; solid circles, 175 mg/m^2; open triangles, 225 mg/m^2). (A) Log-lin plot showing the non-exponential nature of the tails of the curves. (B) Log-log plot showing three distinct power law regions. 50

4.3 The effect of the infusion time (IT) on the shape of the concentration-time curve. (Open circles, IT = 1 h; solid circles, IT = 3 h; open triangles, IT = 6 h; solid triangles, IT = 24 h.) 53

4.4 The effect of the strength of the linear binding compartment on the shape of the concentration-time curve. The tail becomes exponential for high k_{13} values. (Open circles, $k_{13} = 0\,\mathrm{h}^{-1}$; solid circles, $k_{13} = 2.2\,\mathrm{h}^{-1}$; open triangles, $k_{13} = 8.8\,\mathrm{h}^{-1}$.) 54

4.5 The effect of the dose on the shape of the concentration-time curve for a hypothetical two-compartment model with $K_M^d << K_M^e$. (Open circles, 40 mg; solid circles, 50 mg; open triangles, 60 mg; solid triangles, 75 mg; open squares, 100 mg.) The model parameters were $v_{\max}^d = 10.0\,\text{mg} \cdot \text{L}^{-1}\text{h}^{-1}$, $K_M^d = 0.1\,\text{mg} \cdot \text{L}^{-1}$, $k_{21} = 0.5\,\text{h}^{-1}$, $v_{\max}^e = 1.0\,\text{mg} \cdot \text{L}^{-1}\text{h}^{-1}$, $K_M^e = 5.0\,\text{mg} \cdot \text{L}^{-1}$, and $V_d = 5.0\,\text{L}$. 55

4.6 The dose-dependence of AUC and C_{max}. The model parameters are those described for Fig. 4.5. 57

4.7 The relationship between β and α for a three-compartment model. The value for β was determined for 3-h infusions of 135, 175, 200, 250, and 300 mg/m^2 of paclitaxel (open circles, AUC; solid circles, C_{max}.) The model parameters were $K_M^d = 0.1\,\text{mg} \cdot \text{L}^{-1}$, $k_{21} = 0.68\,\text{h}^{-1}$, $v_{\max}^e = 18.8\,\text{mg} \cdot \text{L}^{-1}\text{h}^{-1}$, $K_M^e = 5.5\,\text{mg} \cdot \text{L}^{-1}$, $k_{13} = 2.2\,\text{h}^{-1}$, $k_{31} = 0.65\,\text{h}^{-1}$, and $V_d = 4.0\,\text{L}$. The parameter $v_{\max}^d$ varied between $5.1\,\text{mg} \cdot \text{L}^{-1} \cdot \text{h}^{-1}$ and $20.4\,\text{mg} \cdot \text{L}^{-1} \cdot \text{h}^{-1}$. 58

5.1 Concentration-time curve for mibefradil data for Dog 3. (A) Log-log plot showing the long-time power law tail from 30 min to 1440 min. The dashed line is the regression line with $\gamma = -0.597 \pm 0.024$. (B) The same data but the dashed line now represents the best-fit curve found using the SSFMM model with $X = 2.74$. 70

6.1 The probability p that a molecule will move to an empty elimination (E) site, given the number N_e of currently populated E sites, with $N_e^{\max} = 15$ (open circles), $N_e^{\max} = 30$ (solid circles), and $N_e^{\max} = 45$ (open triangles). 78

6.2 (a) Reaction rate as a function of plasma occupation with $N_e^{\max} = 30$. The solid line represents a moving-average trendline. (b) Reciprocal Lineweaver-Burk plot of the same data. The solid line represents the best-fit obtained by regression analysis, with corresponding values of $v_{\max} = 1.14 \pm 0.01$ and $K_M = 317 \pm 8$ ($R^2 = 0.958$). 79

6.3 (a) The plasma occupation following a bolus dose of 10,000 drug molecules undergoing short-term interactions. (b) The decline is first linear and then transitions to exponential. 80

6.4 Reaction rate as a function of plasma occupation following a bolus dose of 10,000 molecules undergoing short-term interactions with $N_e^{\max} = 15$ and $\Omega = 100$ (closed triangles), $\Omega = 5$ (open triangles), $\Omega = 2$ (closed circles), and $\Omega = 1$ (open circles). The $\dot{X}_P$ and X_P values were averaged over 5 runs. 82

6.5 (a) The plasma occupation following a bolus dose of 10,000 drug molecules undergoing long-term interactions ($\Omega = 1$). (b) The decline follows a stretched exponential. 83

6.6 The power law dependence of k on t for a lattice with long-term correlations ($\Omega = 1$). 84

6.7 (a) The plasma occupation following a bolus dose of 10,000 molecules undergoing both short-term and long-term correlations ($N_e^{\max=15}$ and $\Omega = 1$). The decline is (b) first linear and then transitions to (c) a power law. 86
6.8 The probability distribution of drug residence times θ for a system undergoing combined short- and long-term interactions ($N_e^{\max} = 15$ and $\Omega = 1$). 87
6.9 (a) Area under the plasma curve and (b) the maximum plasma concentration as a function of the infusion rate for a system with no temporary traps and elimination following linear (open circles), fractal (solid circles), Michaelis-Menten (open triangles), or fractal Michaelis-Menten (solid triangles) elimination kinetics. 89
6.10 Plasma occupation curves for a system with (a) Michaelis-Menten elimination kinetics and (b) fractal Michaelis-Menten kinetics. The infusion rate is, from top to bottom: 100, 10, 5, 3, and 1 molecule per time step . 90

7.1 Lévy probability density functions for $\beta = 1$, $\sigma = 1$, and $\mu = 0$. 97
7.2 Lévy probability density functions for $\alpha = 0.8$, $\sigma = 1$, and $\mu = 0$. 97
7.3 (a) The plasma occupation as a function of time for $N = 10,000$ molecules undergoing simple elimination and Lévy-distributed trapping with $\alpha = 1.6$. (b) Closeup of the the power law segment between $t = 30$ and $t = 1000$. 105
7.4 The plasma occupation for $N = 10,000$ molecules undergoing simple elimination and Lévy-distributed trapping. From top to bottom, $f_E/f_T = 0.1, 0.2, 0.6, 1.0, 1.4, 2.0$. 108
7.5 The plasma occupation for $N = 10,000$ molecules undergoing saturable elimination and Lévy-distributed trapping. From top to bottom, $N_E^{\max} = 15, 30, 45, 10,000$. 110
7.6 The plasma occupation for $N = 10,000$ molecules undergoing fractal elimination and Lévy-distributed trapping. From left to right, $\Omega = 100, 5, 3, 2, 1$. 110
7.7 The plasma occupation for $N = 10,000$ molecules undergoing Lévy-distributed trapping and simple (S) elimination or steady steady fractal (SSFMM) elimination ($N_E^{\max} = 15$). 111
7.8 The target occupation as a function of time for $N = 10,000$ molecules undergoing Lévy-distributed trapping with $\alpha = 1.6$ and fractal Michaelis-Menten (SSFMM), Michaelis-Menten (MM), fractal (F), or simple (S) elimination. 113
7.9 The target occupation as a function of the plasma occupation for $N = 10,000$ molecules undergoing Lévy-distributed trapping with $\alpha = 1.6$ and Michaelis-Menten (MM), fractal Michaelis-Menten (SSFMM), simple (S), or fractal (F) elimination. 114
7.10 Area under (a) the plasma occupation curve and (b) the target occupation curve for Lévy-distributed traps with elimination following linear (open circles), fractal (solid circles), Michaelis-Menten (open triangles), and fractal Michaelis-Menten (solid triangles) kinetics. 116

7.11 Maximum (a) plasma and (b) target occupation number for Lévy-distributed traps with elimination following linear (open circles), fractal (solid circles), Michaelis-Menten (open triangles), and fractal Michaelis-Menten (solid triangles) kinetics. 117
7.12 The target occupation number as a function of the plasma occupation number for Lévy traps and (a) linear or (b) fractal Michaelis-Menten elimination. The curves represent an infusion rate of, from inside to outside, 100, 10, 5, and 1 molecules per time step. 118

8.1 The liver. (a) The macrostructure. The hepatic artery and portal vein bring blood rich in oxygen, nutrients, and drug molecules in from the left. (b) The vessels branch to form a tree of arterioles and venules. (c) Pairs (represented by open circles) of terminal hepatic arterioles and portal venules empty into a hexagonal lobule. The blood flows towards a central hepatic venule (solid circle) The dotted lines represent sheets of hepatocyte, and the white space between them represents the sinusoids. . 122
8.2 Homogeneous lattice. The grey bands represent sinusoids and the white spaces represent hepatocytes. 125
8.3 Simplified scheme of the Phase I metabolism of paclitaxel (PAC) by the enzyme cytochrome (CYP) P450 3A4 to form the metabolite hydroxy-paclitaxel (PAC-OH). 126
8.4 Contour plot of the molar fraction of paclitaxel on a regular lattice with a constant infusion of 0.01 molar fraction of the drug. The snapshots were taken at 0.00002, 0.00012, 0.00024, 0.00036, 0.00050, and 0.0012 minutes. 129
8.5 (a) The molar fraction of the metabolite PAC-OH as a function of time following a linear reaction on a regular lattice. (b) In the transient regime, the curve exhibits linear behaviour. 130
8.6 (a) The molar fraction of the metabolite PAC-OH as a function of time following a Michaelis-Menten reaction on a regular lattice. (b) Lineweaver-Burke plot. 131
8.7 Lattice with random permeabilities. The shade of grey represents the permeability of the sinusoid (where a darker colour indicates a higher permeability), while the white hepatocyte sites have a constant permeability. 132
8.8 Molar fraction χ of the metabolite PAC-OH as a function of time for a linear reaction on a lattice with $\sigma = \kappa$. 134
8.9 Initial fractal kinetics of the molar fraction χ of the metabolite PAC-OH showing the power law dependence of k on time for the linear reaction on a random permeability lattice. 134
8.10 (a) Molar fraction of the metabolite PAC-OH as a function of time for a Michaelis-Menten reaction on a random permeability lattice with $\sigma = \kappa$. (b) The initial power law increase, which transitions to (c) a linear increase. 135

8.11 Contour plot of the molar fraction of paclitaxel on a lattice with random permeability ($\sigma = \kappa$), Michaelis-Menten kinetics ($K_M = 2 \times 10^{-8}$ and $v_{\max} = 10,000$ min^{-1}, and a constant infusion of 0.01 molar fraction of the drug. The snapshots were taken at 0.006, 0.016, 0.036, 0.064, 0.1, and 0.4 minutes. 136

8.12 The effect of K_M on the Michaelis-Menten reaction on a random permeability lattice with $\sigma = \kappa$. From top to bottom: $K_M = 2 \times 10^{-14}$, $K_M = 2 \times 10^{-13}$, $K_M = 2 \times 10^{-12}$, and $K_M = 2 \times 10^{-8}$ 138

8.13 Lattice with $p = 0.4$. The grey bands are sinusoids and the white spaces are hepatocytes. 139

8.14 Initial fractal kinetics of the molar fraction χ of the metabolite PAC-OH showing the power law dependence of k on time for a linear reaction on a percolation lattice. 140

8.15 (a) Molar fraction of the metabolite PAC-OH as a function of time for a Michaelis-Menten reaction on a percolation lattice with $p = 0.6$. (b) The initial power law increase, which transitions to (c) a linear increase. 141

8.16 Evolution of the molar fraction of paclitaxel on a percolation lattice with probability $p = 0.6$ of each sinusoid being intact, at $t = 0.0004, 0.0012, 0.002, 0.0042, 0.008, 0.02$ min. 142

A.1 The Koch curve. The initiator is shown in (a) and the generator is shown in (b). Configurations (c) and (d) are formed by replacing every line segment by successively smaller copies of the generator. 169

A.2 The Sierpinski gasket. To generate the next iteration, three copies of the object are arranged to form a figure that is similar in shape but twice the size. 169

A.3 The Weierstrass-Mandelbrot function $C(t)$ with $b = 1.5$ and $-1000 \leq n \leq 1000$. (a) $D = 1.3$. (b) $D = 1.7$. 171

A.4 The Weierstrass-Mandelbrot function $C(t)$ with $b = 1.5$, $D = 1.7$, and $-1000 \leq n \leq 1000$. (a) $0 \leq t \leq 1$. (b) $0 \leq t \leq 0.01$. 172

A.5 A fractal tree with dichotomous branching. At each level, both the radius and the length of the branch are reduced. 175

Chapter 1

Introduction

Humans have a long history of using compounds to achieve therapeutic effects. The Chinese scholar-emperor Shen Nun compiled a book about medical herbs around 2700 B.C., and synthetics compounds were created as early as the fourth century B.C. by Hippocrates [34]. Today, drugs play a crucial role in the way that we diagnose, treat, and prevent disease. Pharmacokinetics – the study of the absorption, distribution, metabolism, and eventual elimination of a drug or chemical from the body – is the main quantitative tool used in all stages of drug formulation and administration. During the development stage, it aids in the design and analysis of laboratory experiments and the elucidation of drug mechanisms. During Phase I and II clinical trials, it is essential in evaluating the drug's effectiveness, optimum dose levels, and preferred routes of administration. During Phase III clinical trials, pharmacokinetics is used to compare the new drug with standard therapies. Finally, in daily clinical practice, it is used to calculate optimum doses for individual patients. The focus of this thesis is to advance our understanding of the way that the body processes drugs and the implications for patient therapy.

1.1 Challenges to Pharmacokinetic Modeling

The quantification of the course of a drug in the body is subject to certain constraints. Firstly, pharmacokinetic data consist primarily of the drug concentration in the plasma at discrete times. However, the site of action of the drug is typically outside the plasma, and crucial information about the actual dose to the target may be unavailable. In addition, clinical procedures and patient comfort limit the number of samples that can be taken, which in turn constrains the number of model parameters that can be fit to the data with sufficient statistical significance. In a literature review of 50 random pharmacokinetic studies performed between 2001 and 2003, it was found that the average number of experimental data points was 12 ± 5, with the overall sampling time ranging between 30 minutes and 28 days. In only 11 of the studies was there additional data for the drug concentration in the urine, endocrine system, dialysate, or expired air.

Compartmental models are the most common type of pharmacokinetic model due to their wide range of applicability and ease of use in a clinical setting. The body is divided into a network of compartments, where a compartment is defined as a kinetically-distinct amount of the drug. In classical pharmacokinetics, each compartment is assumed to be homogeneous and instantaneously well-mixed, such that the transfer of drug between compartments follows linear or Michaelis-Menten kinetics. However, there is evidence that many spaces in the body are heterogeneous and/or poorly-mixed, and thus classical kinetics may be an inadequate model for certain drug processes. The pharmacokinetics of a drug can be altered due to spatial heterogeneity (for example the branching geometry of the vascular system) and/or temporal heterogeneity (for example the long-time trapping of drug molecules in tumour cells).

1.2 The Role of Physics

Mathematical methods have been developed in fields of physics to describe and model transport and reaction processes occurring on or within heterogeneous media. These

techniques include fractal geometry and fractal kinetics, percolation lattices, universality, and scaling. Since a dose of drug can be treated as an ensemble of many identical drug molecules, tools from statistical mechanics, such as random walks and Monte Carlo simulations, can be applied to its analysis. For example, a typical dose the anticancer drug paclitaxel contains on the order of 10^{20} drug molecules. Physical models can relate the macroscopic behaviour of the ensemble to the microscopic behaviour of the individual drug molecules.

By applying a combination of deterministic and stochastic modeling, different aspects of the system can be investigated and modeled. Generally, deterministic models are best for curve fitting and clinical applications, while stochastic models can provide realistic models of fundamental drug processes and a platform to simulate the behaviour under different conditions.

1.3 Hypothesis

In this thesis, it is proposed that the observed nonlinear behaviour of many drugs is a result of the underlying complexity of the course of a drug. While such complexity might seem to preclude models simple enough for clinical applicability, the opposite is in fact true; relatively basic formulas have been developed that accurately describe complex systems. This research aims to apply techniques from physics to develop more accurate and meaningful pharmacokinetic models as well as clinically-relevant information. As such, the goals of this research can be divided into two categories:

1. To increase our understanding of drug behaviour by:
    - reproducing the observed pharmacokinetic behaviour of anticancer and cardiac drugs in the body, especially their long-time power-law tails and nonlinear dose-dependence;
    - developing methods to extrapolate the dose to the target from the observed plasma concentration-time curve;

- introducing the power law tail exponent as a diagnostic tool of drug behaviour;
- exploiting the scaling properties of power laws to relate the observed macroscopic behaviour to underlying microscopic processes and the behaviour at the organ level to that at the level of the functional unit.

2. To improve clinical applications through:

   - better estimates of optimum dose levels, timing, and length of infusion to achieve the maximum therapeutic effect;
   - individualized treatment plans for patients, using new scaling relationships;
   - novel quantitative parameters derived from plasma concentration-time curves that can be used to dynamically evaluate the response of a patient to a treatment regimen.

1.4 Original Contributions

This thesis presents the following new contributions:

- extension of fractal pharmacokinetic theory to include Michaelis-Menten reactions.
- development of a parameter optimization method based on a simulated annealing algorithm to fit fractal compartmental models to experimental data.
- incorporation of the fractal Michaelis-Menten theory into a compartment model that provides an improved fit to data for the cardiac drug mibefradil.
- evidence of correlation between power law dose dependence and power law tails of concentration-time curves for the anticancer drug paclitaxel.
- development of the first stochastic pharmacokinetic model that includes both short-term and long-term interactions between drug molecules. This interacting random walk model supports the analytical theory predicted by the fractal Michaelis-Menten equation.

- expansion of the random walk model into a continuous time random walk that incorporates temporal heterogeneity in the form of drug trapping times as Lévy flights.
- use of a physiologically-based network model to relate the macroscopic fractal behaviour at the organ compartment level to the behaviour at the level of the functional unit of the organ.
- use of a random lattice and a percolation lattice to model the heterogeneity of the structure of both healthy and diseased livers.

1.5 Organization of the Thesis

A review of basic pharmacokinetic concepts is presented in Chapter 2. In Chapter 3, a computational method for parameter optimization based on a simulated annealing algorithm is described. A new equation for Michaelis-Menten kinetics occurring within a heterogeneous environment is derived in Chapter 4 and shown to provide an improved fit to data for the cardiac drug mibefradil. In Chapter 5, clinical data for the anticancer drug paclitaxel is shown to obey power law behaviour that emerges from the competition between two saturable processes. In Chapter 6, an interacting random walk model is developed that reproduces fractal-like elimination kinetics, and in Chapter 7 this model is expanded into a continuous time random walk model that incorporates the effects of long-time trapping of drug molecules within the body. The results of a physiologically-based flow network model for the functional unit of the liver are presented in Chapter 8. Finally, Chapter 9 summarizes the main conclusions of the thesis and provides direction for future research.

Chapter 2

Basic Concepts in Pharmacokinetics

Pharmacokinetics is the quantification of the course of a drug through the body, including its absorption, distribution, metabolism, and excretion. The aim of pharmacokinetic modeling is to describe and predict the behaviour of a drug, with the ultimate clinical goal of maximizing the drug's therapeutic effect while minimizing any toxic effects. Pharmacological data in humans and lab animals such as dogs or mice typically consist of discrete values of the concentration of a drug in a certain volume as a function of time. The work in this thesis will focus on drug concentration values in the plasma obtained through intravenous sampling; however, the methods described can be equally applied to pharmacokinetic data obtained through other methods or for other tissues.

2.1 Plasma Concentration-Time Curves

Drugs can be introduced into the body through a variety of routes, including subcutaneous, intramuscular, oral, buccal, bolus intravenous (IV), and IV infusion. The latter two should be distinguished from the others, since they entail direct input of the drug into the bloodstream and thus involve no absorption processes. In most cases, the dose

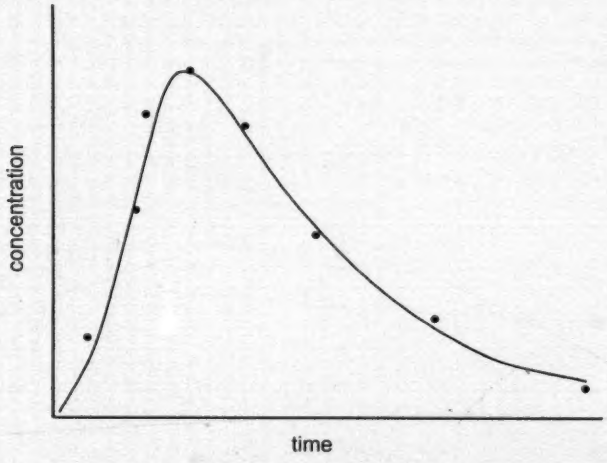

Figure 2.1: An example of a plasma concentration-time curve for a drug undergoing absorption, distribution, metabolism, and elimination in the body following an intravenous infusion.

results in transient pharmacokinetics, and the system progresses in a dissipative manner until all of the drug has left the system. A plot of these values generates a plasma concentration-time curve that first rises as absorption of the drug dominates and then decreases after a maximum concentration value is reached. This decline may be relatively short or may last for several days, and it is mainly governed by the rate of elimination of the drug from the body. The simplest case is illustrated in Fig. 2.1. Unless otherwise indicated, the term "concentration-time curve" will refer to the values for the plasma.

When a dose of drug is given as a bolus directly into the vascular system, the resulting concentration-time curve decreases continuously from a maximum and is called a clearance curve. For drugs rapidly distributed throughout the body, the shape of the curve is determined predominantly by the rate of elimination through enzymatic biotransformation or direct excretion. In this case, the input function is given by

$$I(t) = \begin{cases} D_0 & t = 0 \\ 0 & t > 0 \end{cases}, \tag{2.1}$$

the resulting concentration-time curve is called a clearance (or washout) curve.

Due to its systemic pervasion and relative ease of access, the blood is the dominant material for which pharmacokinetic data are taken. However, because a drug's target is most often outside of the blood, pharmacokinetic data tend to be an indirect signal from which the desired or crucial information must be deduced.

2.2 Pharmacokinetic Parameters

Certain parameters are used to quantitatively describe a pharmacological data set. Pharmacokinetic parameters depend on intrinsic properties of a drug and the physiological system with which it interacts [157]. These include:

Area under the curve (AUC): a measure of the systemic exposure to the drug when calculated for the plasma curve. It reflects the ability of the body to remove a drug, where a larger value indicates a lower ability. The AUC is calculated as

$$AUC = \int_0^\infty C(t)dt. \tag{2.2}$$

Volume of distribution (V_d): the theoretical, apparent volume of fluid in which the total administered dose would have to be distributed in order to achieve the concentration observed in the plasma. It is a ratio between the amount of drug in the body and the observed plasma concentration. Gilette [63] proposed that V_d is directly proportional to the free fraction of drug in the plasma and inversely proportional to the free fraction of drug in other tissues. Thus drugs that are highly bound to plasma proteins will lead to a low apparent V_d and a high plasma concentration, and drugs that are highly bound to tissues will exhibit a high apparent V_d and a low plasma concentration. The volume of distribution is generally only used for linear, stationary systems under steady state conditions.

Clearance (Cl): the volume of plasma cleared of a drug per unit time. Clearance describes the efficiency of irreversible elimination of a drug from the body, an organ, or

a pathway. For total body clearance:

$$F \cdot D = \int_0^\infty Cl \cdot C(t)dt, \tag{2.3}$$

where F is the bioavailability, D is the dose, and $C(t)$ is the drug concentration at time t. For constant clearance:

$$Cl = \frac{F \cdot D}{AUC}. \tag{2.4}$$

Maximum concentration (C_{max}): occurs at a time T_{max} and is usually calculated by fitting an equation to the concentration curve and solving for

$$\frac{dC}{dt} = 0 \Big|_{C=C_{max}}. \tag{2.5}$$

Half-life ($t_{1/2}$): the time required to reduce the drug concentration in the plasma by one-half. While the half-life gives a quantitative measure of the presence of the drug in the body, it is constant only for monoexponential functions [156].

Although most *pharmacokinetic parameters* are defined independently of a model, their calculation may depend on the mathematical model chosen to represent the system [157]. The *model parameters* are those quantities specific to the chosen model, and while they depend on the drug and physiological properties, they also depend on the hypotheses of the model. The next section summarizes the main types of pharmacokinetic models.

2.3 Pharmacokinetic Models

Pharmacokinetic studies can be generalized into two categories: individual-based or population-based. In individual-based studies, pharmacokinetic parameters are estimated independently for each patient. Population-based studies, on the other hand, pool drug concentration values from more than one individual. They account for both random and fixed effects that produce the variability between individuals and within

individuals [152]. Although less data points are required per patient when using this approach, assumptions must be made in combining data from different patients and potentially from different studies. These include the shape of the sampling distributions of the population estimates.

2.3.1 Compartmental Models

In compartmental modeling, the most widely-used type of modeling in pharmacokinetics, the body is represented by a system of compartments that may or may not have anatomical or physiological meaning. A compartment is defined to be an amount of material that acts kinetically like a distinct, well-mixed amount of the material [83]. In other words, every drug molecule in a compartment has the same probability of undergoing a set of chemical or transport processes. The exchange of drug molecules between compartments is described by kinetic rate coefficients. Two compartments merge if they exchange material so rapidly that they are indistinguishable. The models are usually open, with at least one input and one output.

Classical kinetics is based on the law of mass action, which states that the rate of a chemical reaction is directly proportional to the product of the concentrations of the M reactions each raised to the order n_i,

$$v = k \prod_{i=1}^{M} X_i^{n_i}, \tag{2.6}$$

where X_i is the mass of reactant i and k is the kinetic rate coefficient. The reaction order n_i is the number of mass terms that must be multiplied together to get the rate of the reaction [44]. For a single step, n_i is typically equal to the molecularity, which is the number of molecules that are altered during the reaction.

In a one-compartment model, the body is approximated as a single homogeneous compartment. It is important to note that this does not mean that the drug concentration is the same everywhere in the body; rather, the *change* in the drug concentration is

everywhere proportional to the *change* in the plasma concentration. When only one molecule is modified, the linear one-compartment model is described by

$$\frac{d}{dt}X(t) = kX(t). \tag{2.7}$$

The general case of N compartments is represented by a system of coupled ordinary differential equations:

$$\frac{d}{dt}\mathbf{X}(t) = \mathbf{K}\mathbf{X}(t), \tag{2.8}$$

where $\mathbf{X}(t)$ is the column vector

$$\mathbf{X}(t) = \begin{pmatrix} X_1(t) \\ \vdots \\ X_N(t) \end{pmatrix}. \tag{2.9}$$

The matrix $\mathbf{K}$ has dimensions $N \times N$ and elements k_{ij}. Typically, $k_{ij} \neq k_{ji}$ and the matrix $\mathbf{K}$ is not symmetric. A bolus dose D_0 injected into the first compartment takes the form of the initial condition

$$\mathbf{X}(0) = \begin{pmatrix} D_0 \\ 0 \\ \vdots \\ 0 \end{pmatrix}. \tag{2.10}$$

The general solution to Eq. (2.8) is [115]

$$X_i(t) = \sum_{j=1}^{m} a_{ij} \left(\sum_{k=0}^{m_j-1} c_{ijk} t^k \right) \exp\left(\lambda_j t\right), \tag{2.11}$$

where i, j, and k are integers, a_{ij} and c_{ijk} are constants, and $\mathbf{K}$ has m distinct eigenvalues λ_i with multiplicity m_i.

The above equations can be written alternatively in terms of the drug concentration

by using the concept of the volume of distribution introduced in Section 2.2, since

$$X = V_d C. \tag{2.12}$$

For constant V_d, Eq. (2.8) becomes

$$\frac{d}{dt}\mathbf{C}(t) = \mathbf{K}\mathbf{C}(t). \tag{2.13}$$

If an IV infusion is administered instead of a bolus dose, the following matrix would be added to the righthand side of Eq. (2.8) or Eq. (2.13):

$$\mathbf{I}(t) = \begin{pmatrix} i(t) \\ 0 \\ \vdots \\ 0 \end{pmatrix}, \tag{2.14}$$

where $i(t)$ is the infusion rate in units of mass/time.

Advantages of compartmental models include their wide applicability and the fact that they can be formulated in terms of anatomical components or physiological processes. For example, the pharmacokinetics of an anesthetic drug could be modeled by two compartments, one for the plasma and one for the brain. The two compartments would exchange drug molecules at a rate dependent on the permeability of the blood-brain barrier.

Limitations of classical compartmental models lie in their assumptions, the main one being that each compartment is homogeneous and instantaneously mixed. To assess the applicability of compartmental models to a given situation, the relative mixing rates within compartments should be compared to the transfer rates between compartments.

A subset of compartmental models is the so-called physiologically-based pharmacokinetic (PBPK) models [41]. While this term incorrectly implies that classical compart-

mental models have no physiological basis, PBPK models differ by explicitly expressing the kinetic rate coefficients and volumes of distribution in terms of physiological and anatomical parameters such as blood flow and metabolic rates, organ volumes, membrane permeability, and molecular binding constants. There are two general types of PBPK models: flow- or diffusion-limited models and membrane- or perfusion-limited models (see [5] for a comprehensive study involving both types of models). Advantages of PBPK models include transfer coefficients related directly to physiological processes and easier scaling of models between species and from *in vitro* to *in vivo* [41]. Disadvantages of these models include the necessary amount of detailed kinetic information, their relative complexity, and difficulties in validating the parameters and fitting them to experimental data. Some software has been developed to make these models more user-friendly (see for example PKQuest [100]).

2.3.2 Non-Compartmental Models

To address some of the limitations of compartmental models, several non-compartmental approaches have been developed. The method of moments, or mean residence time theory, uses not only the AUC but also quantities like the area under the moment curve (AUMC) and the mean residence time (MRT) to deduce information about a data set [194]. Linear system analysis (LSA) uses procedures such as convolution, deconvolution, and disposition decomposition analysis [190]. Circulatory models describe drug disposition in terms of repeated cycles in the circulatory system, where the residence time of a drug molecule is determined by the cycle time and the number of cycles the molecule undergoes before elimination (see for example [98]).

Advantages of non-compartmental analysis include fewer assumptions and ones that are typically related to the observed behaviour rather than the nature or mechanisms of the underlying system [62]. In addition, they provide general methods that can apply to a wide range of data sets. Both compartmental and non-compartmental methods can be applied to the same system, either in complimentary roles or with non-compartmental

analysis as an initial investigation [164].

It is important to note that in many cases, 'non-compartmental' models can be mapped onto the compartmental framework. For example, Lánský [98] points out that his circulatory model can be studied as a unilateral compartmental model in which the compartments are arranged in series with a feedback loop.

2.3.3 Stochastic Pharmacokinetic Models

Both compartmental and non-compartmental models can be formulated in terms of deterministic and/or stochastic variables. Stochastic components can be incorporated through the use of

- random inputs or initial conditions;
- a random matrix representation for the kinetic rate coefficient $\mathbf{K}$;
- random walk models in which single molecules are followed between compartments or states.

An example of a noncompartmental stochastic model is the circulatory model mentioned in the previous section.

If the random components are added to the kinetic rate coefficients of a compartmental model, the effect is linear [83]. For example, consider the following one-compartment model:

$$\frac{dC}{dt} = fC + i(t) \tag{2.15}$$

$$f = k + \alpha, \tag{2.16}$$

where k and α represent the deterministic and stochastic components, respectively. These equations can be rewritten as a deterministic system with a stochastic input:

$$\frac{dC}{dt} = kC + [\alpha C + i(t)]\,. \tag{2.17}$$

On the other hand, if the random components are added to the concentration values, the effect is nonlinear.

2.4 Nonlinear Pharmacokinetics

The concept of linearity is sometimes poorly defined in the pharmacokinetic literature. In general, a system is considered to be linear when its output is directly proportional to its input. Systems that can be described by a set of linear differential equations guarantee such a property. As discussed in Section 2.3.1, a linear ODE has kinetic order $n = 0$ or $n = 1$ and is expressed for a one-compartment model as

$$\frac{dC}{dt} = kC. \tag{2.18}$$

Linear processes obey the superposition principle, which states that the whole is equal to the sum of its individual components. If the variable y is linearly related to x, then for arbitrary constants k_1 and k_2, the response to $x = k_1x_1 + k_2x_2$ is [190]

$$y = k_1y_1 + k_2y_2. \tag{2.19}$$

The superposition principle implies that molecules behave in a stochastically independent manner [189]. In nonlinear systems, however, the behaviour of one molecule is influenced by that of other molecules [46].

In a clinical setting, nonlinear behaviour of a drug can complicate the design of dosage regimens as well as predictions of the drug's effectiveness and toxicity. The main types of nonlinearity that are discussed in the pharmacokinetic literature fall into two categories: dose-dependence and time-dependence.

Dose-proportionality is a concept common in dose-escalation experiments, which are primarily conducted early in the research of a new drug (such as in Phase I clinical trials). The response of patients to different doses of the drug is measured. If the phar-

macokinetic parameters are unchanged with changes in the dose, the pharmacokinetics of the system is said to be *dose-independent* over the therapeutic range studied [68]. If a doubling of the dose of a drug produces a doubling in one or more pharmacokinetic parameters (typically the AUC or C_{max}), the system is considered to be *dose-proportional* and *linear*. If the parameter values decrease, or increase by a factor other than two, the system is considered to be *dose-proportional* and *nonlinear*.

Time-dependent pharmacokinetics is present when the pharmacokinetic parameters vary with time due to physical alterations in the body, whether in the form of physiological changes related to the body's circadian rhythms (called chronopharmacokinetics) or chemically-induced changes brought about by the introduction of the drug into the body [101].

Both dose-dependency and time-dependency can be present in the same system (i.e. the pharmacokinetic parameters describing a system can vary both in time and with dose), and in fact the sources proposed for both are similar. Lin [103] states that the causes of nonlinear dose-dependent pharmacokinetics can be found in the processes of absorption, tissue distribution, protein binding in both the plasma and tissues, and elimination. Levy [101] breaks down the potential causes of time-dependence into the categories of absorption and elimination parameters, metabolism, plasma binding, renal or hepatic clearance, overall systemic clearance, and enzyme activity. Concentration-dependent pharmacokinetics are usually modeled using Michaelis-Menten kinetics.

2.4.1 Michaelis-Menten Kinetics

The rate of enzyme-catalyzed reactions can deviate from those predicted by classical kinetics. Michaelis-Menten kinetics [126] is the standard formalism for describing these reactions. At high concentrations, saturation of the enzymes limits the maximum reaction rate that can be achieved, while at low concentrations, the rate of formation of the enzyme-substrate complex becomes significant and the reaction becomes dependent on the substrate concentration [133].

$$E + S \rightleftharpoons ES \longrightarrow P + E$$

Figure 2.2: Enzyme-mediated reaction. E, S, ES, and P represent the enzyme, substrate, enzyme-substrate complex, and product, respectively.

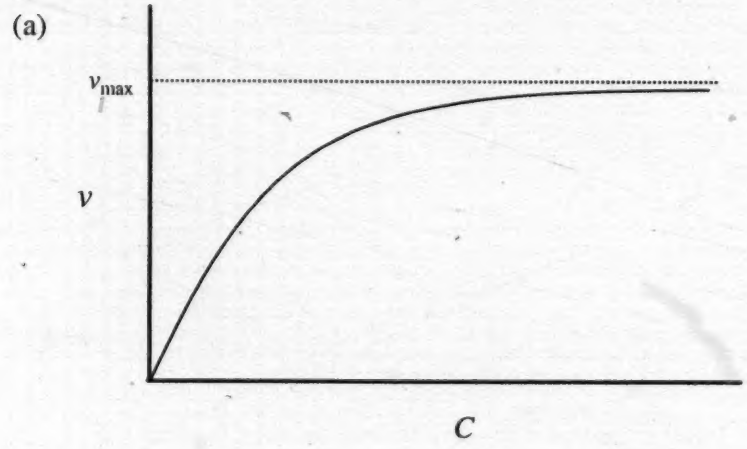

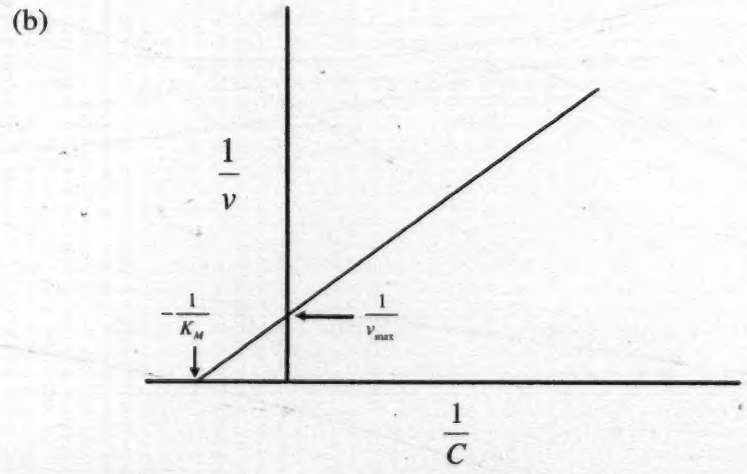

Figure 2.3: (a) Velocity v of a Michaelis-Menten reaction as a function of the reactant concentration, where v_{max} is the maximum rate of the reaction. (b) Lineweaver-Burk plot, where C is the drug concentration and K_M is the Michaelis-Menten constant.

Consider the reaction shown in Fig. 2.2, where E, S, ES, and P represent the enzyme, substrate, enzyme-substrate complex, and product, respectively. If we denote the concentration of the substrate as C, the concentration of the enzyme-substrate as x, and the total concentration of enzymes as e_0, the system is described by the following ordinary differential equations:

$$\frac{dx}{dt} = k_1 (e_0 - x) C - (k_{-1} + k_2) x, \tag{2.20}$$

$$\frac{dp}{dt} = k_2 x. \tag{2.21}$$

Using the Briggs-Haldane treatment [44] to simplify the problem, a quasi-steady-state assumption is made where the concentration of the substrate-enzyme complex is taken to be constant, i.e. $dx/dt = 0$. Therefore,

$$k_1 (e_0 - x) C - (k_{-1} + k_2) x = 0. \tag{2.22}$$

Collecting the terms in x and rearranging gives

$$x = \frac{k_1 e_0 C}{k_{-1} + k_2 + k_1 C}. \tag{2.23}$$

Using the fact that the rate of the reaction is $v = k_2 x$ leads to

$$v = \frac{k_2 e_0 C}{\frac{k_{-1}+k_2}{k_1} + C}. \tag{2.24}$$

Finally, denoting $v_{\max} = k_2 e_0$, $K_M = (k_{-1} + k_2)/k_1$ gives the Michaelis-Menten equation:

$$v = \frac{v_{\max} C}{K_M + C}. \tag{2.25}$$

The parameter $v_{\max}$ is the maximum velocity of the reaction, and the Michaelis-Menten constant K_M is the substrate concentration at half the maximum velocity.

In the low concentration case, where $C << K_M$, Eq. (2.25) reduces to

$$v = \frac{v_{\max}}{K_M}, \tag{2.26}$$

which is first-order kinetics with $k = v_{\max}/K_M$. In the high-concentration case, where $C >> K_M$, Eq. (2.25) becomes

$$v = v_{\max}, \tag{2.27}$$

which is zero-order kinetics with a constant reaction rate.

A plot of v as a function of the concentration reveals a hyperbolic relationship (Fig. 2.3 a). As the concentration increases, v approaches a maximum value. The Michaelis-Menten equation can be rearranged to generate a linear plot (called a Lineweaver-Burk plot, shown in Fig. 2.3 b):

$$\frac{1}{v} = \frac{K_M}{v_{\max}} \frac{1}{X_P} + \frac{1}{v_{\max}}. \tag{2.28}$$

Values for $v_{\max}$ and K_M can be estimated from the slope and y-intercept of the line.

2.5 Transient Fractal Kinetics

Fractals are a mathematical construct that describes certain heterogeneous geometric structures or temporal processes. A introduction to fractal concepts is presented in Appendix A. Anacker and Kopelman [8] found that reactions that occur on or within fractal media exhibit anomalous kinetics that do not follow the classical mass-action form. Specifically, the kinetic rate coefficient becomes time-dependent [94]:

$$k = k_0 t^{-h}, \tag{2.29}$$

where

$$h = 1 - \frac{d_s}{2}. \tag{2.30}$$

The quantity d_s is the spectral dimension that describes the path of a random walker within the medium [7]. The classical case corresponds to $d_s = 2$. The quantity t^{-h} is considered dimensionless, and both k and k_0 are in units of inverse time (h^{-1}). Because Eq. (2.29) has a singularity at $t = 0$ for $h > 0$, Schnell and Turner [170] have suggested a modified form based on the Zipf-Mandelbrot distribution, $k(t) = k_0 (\tau + t)^{-h}$, where the constant τ is the critical time from which the rate constant is driven by fractal effects. However, if τ is very small, Eq. (2.29) is a good approximation.

Equations (2.29) and (2.30) have been supported by experiments of trapping and binary reactions on the Sierpinski gasket, percolation clusters, and lattices with disordered transition rates [8, 75, 94, 93]. While Eq. (2.29) applies to diffusion-limited reactions on fractals, it also applies to any situation for which $h > 0$.

Equation (2.29) has been incorporated into pharmacokinetics through both non-compartmental and compartmental models. The former includes the homogeneous-heterogeneous distribution model introduced by Macheras [107] to quantify the global and regional characteristics of blood flow to organs. The latter includes the fractal compartmental model developed by Fuite et al. [55] in which a classical compartment was used to represent the plasma while a fractal compartment was used to represent the liver. In this formalism, the rate of elimination from the liver is given by

$$v = k_0 t^{-h} C. \tag{2.31}$$

Simulations of the model showed that h plays a significant role in determining the shape of the concentration-time curve [38].

Several attempts have been made to incorporate Eq. (2.29) into the Michaelis-Menten equation to describe concentration-dependent reactions that occur in spatially-constrained conditions. Kosmidis et al. [96] made the substitution $k_1 = k_1^0 t^{-h}$ into Eq. (2.20), producing the formula

$$v = \frac{v_{\max} C}{K_M t^h + C}. \tag{2.32}$$

They also performed Monte Carlo simulations and found that Eq. (2.32) holds mainly when the initial substrate concentration is high, either through an intravenous (IV) bolus adminstration or a high rate of absorption. In addition, they incorporated Eq. (2.32) into a one-compartment model. Berry [25] used Monte Carlo simulations on a 2D lattice to model enzyme reactions in low-dimensional media, and he found that h increases independently with increasing obstacle density on the lattice and increasing initial substrate concentration. Simulations performed by Aranda et al. [13] also confirm these results but suggest that K_{M0} is characterized by multifractality and hence a set of fractal exponents.

2.6 Power Laws and Scaling in Pharmacokinetics

A power law relationship such as the one expressed by the time-dependence of the fractal kinetic rate coefficient has special qualities, such as scale-invariance. The variable y follows a power law function of x if

$$y(x) = ax^b, \tag{2.33}$$

where b determines the shape of the relationship between y and x, and a controls the magnitude of the gain in y. If $|b| < 1$, y increases or decreases more slowly than x, and if $|b| > 1$, y changes more rapidly than x. Equation (2.33) possesses the property of scaling; if x is multiplied by a factor L, the constant changes but y remains proportional to x^b:

$$y(Lx) = \left(aL^b\right) x^b. \tag{2.34}$$

The behaviour of y is said to be self-similar over the range of x for which this relationship holds.

Power laws do not single out any particular value (unlike the mean of the Gaussian distribution). The shape or behaviour of such a system is similar at both small and large scales. If a system with a hierarchical organization produces power-law behaviour

over a wide range of values of a given control parameter, the system is said to be scale-invariant [180]. Since naturally-occurring physical and biological systems are neither perfect nor infinite, it is important to specify the range of values over which a scaling regime holds. In pharmacokinetics, for example, this might consist of the therapeutic dose range and the time over which it is attained.

Evidence of power law behaviour has been found in pharmacokinetics, including the shape of clearance curves, nonlinear dose-dependence of pharmacokinetic parameters, and allometric scaling.

2.6.1 Clearance Curves

There is evidence that the concentration-time curves of many drugs exhibit long-time power law tails of the form

$$C(t) \sim t^{\gamma} \quad \text{for } t > T, \tag{2.35}$$

where γ is negative, and T marks the time of the onset of the tail. Negative power laws were first applied, empirically, to describe the washout of bone-seeking radioisotopes [143, 201]. Subsequently, other types of clearance curves have been fit by a single power law, two sequential power laws, or the gamma function $y(t) = at^{-\alpha}e^{-\beta t}$ [11, 200, 144, 21].

Different explanations for these power law and gamma function fits have been proposed. Wise *et al.* [202] proposed a stochastic random walk model based on the cycling of radionuclides in and out of the plasma. By changing the ratio of the cycling probability to the elimination probability, Wise was able to produce different power law exponents and even two sequential power laws [201]. Because the nine drugs examined by Norwich and Siu [144] were predominately eliminated through the liver, they developed a model based on the anatomy and vasculature of that organ. Their convection-diffusion equations for the functional unit of the liver, the acinus, generated approximate solutions with gamma and power functions. Weiss [193] fit plasma curves with functions of the form $C = At^{-a}e^{-bt}$, which he shows can arise from gamma-distributed residence times.

He compared the model to a random walk with drift.

2.6.2 Nonlinear Dose-Dependence

Dose-proportionality of pharmacokinetic parameters, such as the AUC and C_{max}, can be identified using a simple plot of the pharmacokinetic parameter as a function of the dose. The graph will be a straight line with a zero intercept if the parameter is linearly proportional to dose. As a better diagnostic tool, Gough et al. [68] suggest the following "power model":

$$P = cD^{\beta} \tag{2.36}$$

where P is a pharmacokinetic parameter and D is the dose. When $\log P$ is plotted as a function of $\log D$, the slope of the line will be equal to the parameter β. Two scenarios are discussed: $\beta = 0$ (dose-independence) and $\beta = 1$ (dose-dependence). While they mention that dose-dependence can be linear or nonlinear, their only suggestion for fitting a nonlinear relationship was the addition of higher-order polynomial terms to Eq.(2.36). In their analysis of eight data sets, the authors found that the slopes were consistent within each study, but they compared each to an expected value of one. The authors stress that their model is empirical and their application of the power law is not mechanistic.

2.6.3 Allometric Scaling

To date, the concept of scaling in pharmacokinetics has been limited to allometric scaling equations of the form

$$Y = aW^{b} \tag{2.37}$$

where Y is the dependent biological variable of interest, W is the weight of the organism, a is a normalization constant called the allometric coefficient, and b is the allometric exponent [109]. The clearance, toxicity, maximum concentration, volume of distribution at steady state, and elimination half-life have all been investigated as a function of mass.

Such relationships have been applied to scaling among humans [185, 136], extrapolation between animal and human models (interspecies scaling) [111, 17], and extrapolation from *in vitro* to *in vivo* [16, 110]. For example, Hu and Hayton [79] studied clearance values from the literature for 115 xenobiotics for various species. They found no correlation between log clearance and log body weight for 21% of the substances, but found an average of $b = 0.74 \pm 0.16$ for the others.

Chapter 3

A Parameter Optimization Method Using a Simulated Annealing Algorithm

3.1 Purpose

This purpose of this chapter is to describe the development of an efficient and accurate parameter optimization method, based on the simulated annealing algorithm, to fit a system of differential equations to a set of experimental data.

3.2 Background

Most deterministic pharmacokinetic models are expressed as a set of differential equations, and modeling is most efficient when these equations can be solved analytically to produce algebraic equations that can be fit to experimental data using linear and nonlinear regression techniques. However, some models, especially those with nonlinear or time-dependent terms, lead to equations that can only be solved numerically. In such cases, including the growing set of fractal models, alternate methods must be developed

to estimate the model parameters. The objectives of this chapter are to experimentally determine the optimal implementation of the SA algorithm, test its performance against existing algorithms, and assess its applicability to fitting compartmental models. Specific attention is given to the case of fractal compartmental models, in which one or more kinetic rate coefficients are power functions of time.

Unfortunately, most fractal models cannot be solved analytically. There are several commercially-available software packages, including WinNonLin [1] and Boomer [2], that make use of the Gauss-Newton [74], and Nelder-Mead simplex [137] algorithms to numerically fit differential equations to experimental data. For models based on classical and Michaelis-Menton kinetics, these programs are excellent. However, even with the option of user-defined models, these programs currently do not have the capability to handle power-law time-dependent kinetic rate coefficients. Furthermore, the Gauss-Newton method is a gradient-based method that involves the calculation of derivatives, and the simplex algorithm is sensitive to initial conditions [42]. To fit their model for fractal Michaelis-Menten kinetics to experimental data, Kosmidis et al. [96] used the Levenberg-Marquardt (LM) algorithm. However, the LM algorithm is also gradient-based; therefore, although it is appropriate for fitting their one-compartment model that can be solved analytically, it may not be the best method for fitting model that do not have an algebraic solution. Furthermore, the LM algorithm has the disadvantage of converging towards local minima when the initial parameter estimates are poor [53]. This chapter describes the simulated annealing algorithm and explores its ability to optimize functions through an efficient exploration of the parameter space.

3.3 Simulated Annealing Algorithm

Kirkpatrick and colleagues developed simulated annealing to optimize the design of integrated circuits, and they later applied it to the optimization of many-variable functions [91]. Simulated annealing (SA) derives its name from an analogy to the cooling

of heated metals. As a metal cools, the atoms fluctuate between relatively higher and lower energy levels. If the temperature is dropped slowly enough, the atoms will all reach their ground state. However, if the temperature is dropped too quickly, the system will get trapped in a less-than-optimum configuration. If the energy function of this physical system is instead replaced by an objective function $f(\{x_i\})$, where $\{x_i\}$ is a set of independent variables, then the progression of this function towards the global minimum is analogous to the physical progression towards the ground state.

The SA algorithm also requires a control parameter, T (the effective temperature), a strategy for changing T, and a method for exploring the parameter space. The algorithm, illustrated in Fig. 5.1, begins at a random initial position in parameter space and its corresponding objective function, f_0. The parameters are then perturbed to generate a trial point with a new objective function, f_1, and the move is either accepted or rejected. All downhill moves, corresponding to $\Delta f = f_i - f_{i-1} < 0$, are accepted, while uphill moves, corresponding to $\Delta f > 0$, are accepted in a probabilistic manner using the Metropolis algorithm [125] based on Boltzmann statistics such that

$$P(\Delta f) = \exp\left[-\frac{\Delta f}{T}\right]. \tag{3.1}$$

A random number is generated over the range $(0,1)$, and if $P(\Delta f) > random(0,1)$, the trial point is accepted. Otherwise, the point is rejected and another trial point is generated. The temperature is decreased every n steps, and the step lengths can be adjusted every m steps. The process continues in an iterative manner until the program converges on a solution. This convergence can be expressed as a function of the temperature, the number of iterations, the acceptance rate of new moves, or the absolute or relative change in the objective function.

At the start of the annealing process, the temperature is relatively high compared to the standard deviation of the values computed for the objective function, so the probability of accepting an uphill move is great. Hence, the random walk is able to

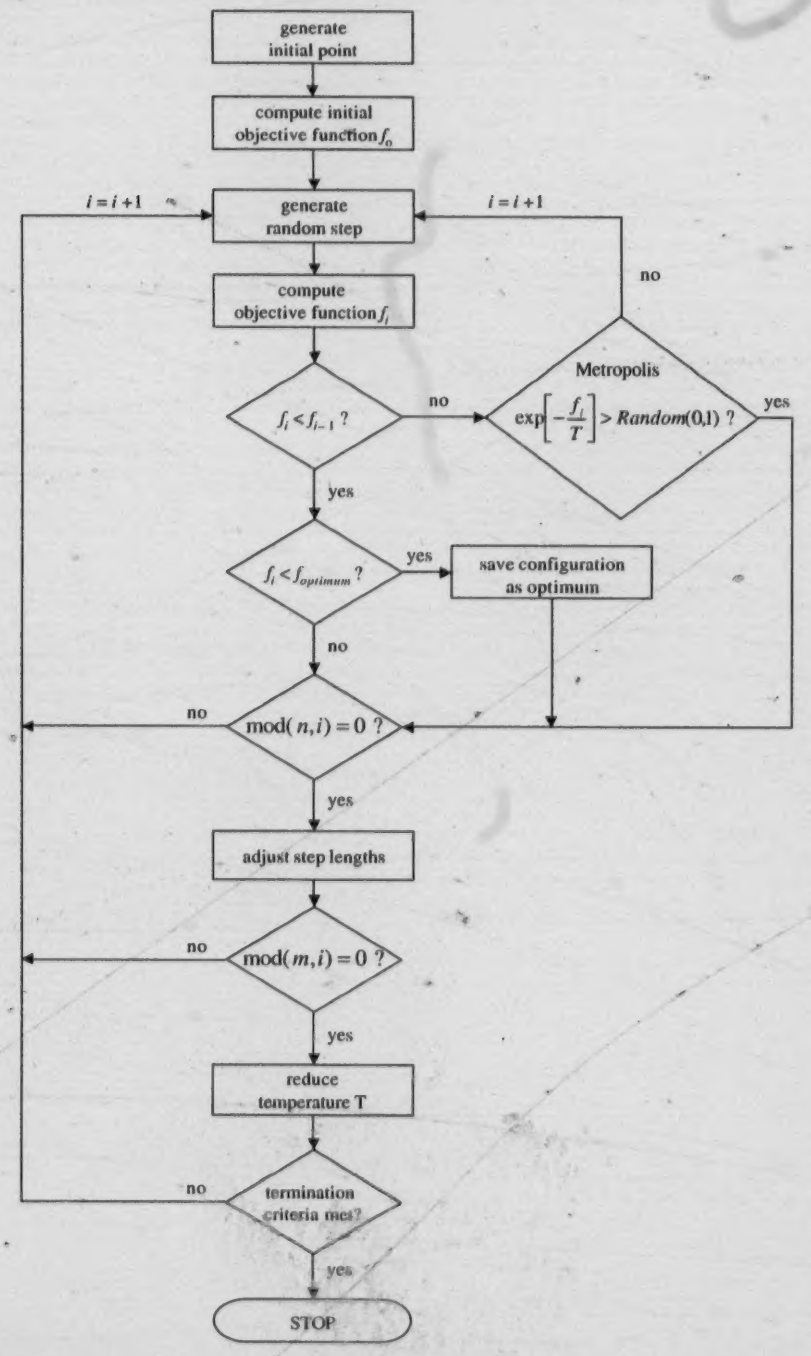

Figuré 3.1: The simulated annealing algorithm. The operator mod (x_1, x_2) returns the remainder of x_1 divided by x_2.

explore a wide area of parameter space without getting trapped in local minima. As the temperature is decreased, the algorithm is able to focus on the most promising areas.

In addition to manipulating the temperature, the magnitude of the step length in parameter space can be controlled. It has been found experimentally that the space is best explored when the acceptance rate of new steps is 50% [125]. A relatively high rejection rate means that the space is being ineffectively explored, while a relatively low rejection rate means the algorithm is being explored with too-small steps.

The SA algorithm has many advantages over other optimization methods. It is largely independent of the starting values, it can escape local minima through selective uphill moves, and the underlying function need not be continuous. The SA method has been found to be superior to the simplex method, the Adaptive Random Search, and the quasi-Newton algorithm in finding the optimum of continuous functions [42, 64]. Eftaxias et al. [53] compared the SA and Levenberg-Marquardt algorithms and found that the LM algorithm was only advantageous when few model parameters must be optimized and a good initial estimate was provided. They observed that the SA algorithm was more robust and found more accurate and meaningful fits as the number of model parameters was increased.

The SA algorithm has been applied to population pharmacokinetics [52], optimal design [85] and in the physiologically-based program PKQuest [100]. However, in the latter, the method is built into an application for Maple, a commercial mathematical problem-solving program, and not explicitly described. To our knowledge, this algorithm has not yet been applied to solve compartmental models in individual pharmacokinetics.

3.4 Methods

3.4.1 The PKPhit Program

A C++ program, PKPhit, was written to implement the SA algorithm. It includes the definition of three classes: Data, Model, and SimAnneal. The Data class holds the

experimental data. The Model class contains the equations of the model, the dosing information, and the chosen form of the objective function. The differential equations were solved numerically using a fourth-order Runge-Kutta routine with 500 steps [153]. The SimAnneal class holds a particular set of values for the parameters and the corresponding value of the objective function. It makes use of three functions to generate a trial set of parameter values, calculate the corresponding cost function, and determine whether or not to accept the new set of values.

3.4.2 Annealing Schedule

The program begins by generating a random starting position in parameter space and calculating the corresponding objective function, f_0. The form of the objective function, f, was chosen to be the weighted residual sum of squares (WRSS):

$$\text{WRSS} = \sum_{i=1}^{n} w_i \left(C_i - \hat{C}_i\right)^2, \tag{3.2}$$

where $\hat{C}_i$ denotes the predicted value of C_i based on the chosen model, and w_i is the weighting factor. The weight is commonly chosen to be the inverse of the variance of the observation, and here an iterative reweighting scheme was chosen where the variance was taken to be proportional to the square of the predicted concentration [56], $\hat{C}_i$, so that

$$w_i = \frac{1}{\hat{C}_i^2}. \tag{3.3}$$

The algorithm progresses as new steps are generated and either accepted or rejected as a function of the temperature, which is reduced every m iterations. The magnitude of a step is calculated by multiplying a random number between 0 and 1 by the step length. The acceptance rate (AR) of new trials is checked every n iterations. The step lengths are increased if $AR > 60\%$, decreased if $AR < 40\%$, and left unchanged otherwise. Following Corana et al. [42], the new step length, L_j', for the j^{th} parameter is calculated

from the previous step length L_j according to

$$L'_j = \begin{cases} L_j \left(1 + c_j \dfrac{AR - 0.6}{0.4}\right) & \text{if } AR > 0.6, \\ \dfrac{L_j}{1 + c_j \dfrac{0.4 - AR}{0.4}} & \text{if } AR > 0.4, \end{cases} \tag{3.4}$$

where c_j is the step length adjustor for parameter j.

The program terminates when the convergence criteria are reached. Several different criteria were investigated alone and in combination, including the total number of iterations, the absolute or relative change in WRSS, the acceptance rate, and the current temperature.

3.4.3 Test Models

The robustness of the SA algorithm in fitting pharmacokinetic parameters was tested using three two-compartment models. Figure 3.2 shows a mamilliary model with a central compartment. The case with constant kinetic rate coefficients, which we will refer to as the classical Model 1, is described by the equations

$$\dot{C}_1 = k_{21} C_2 - (k_{12} + k_{10}) C_1 + \frac{i(t)}{V_d}, \tag{3.5}$$

$$\dot{C}_2 = k_{12} C_1 - k_{12} C_2, \tag{3.6}$$

where C_1 is the concentration in compartment 1, C_2 is the concentration in compartment 2, k_{ij} is the kinetic rate coefficient for the transfer of drug molecules from compartment i to compartment j, and $i(t)$ is the infusion rate of the drug in mass or moles per hour. The term V_d is the apparent volume of distribution, defined as the volume of fluid into which the dose would have to be dispersed in order to produce the concentration observed in the plasma, and it is expressed in liters. Compartment 1 typically corresponds to the plasma, and compartment 2 could represent a tumor, the brain, a bound state, or simply a mathematical construct. For constant kinetic rate coefficients, Equations (3.5)

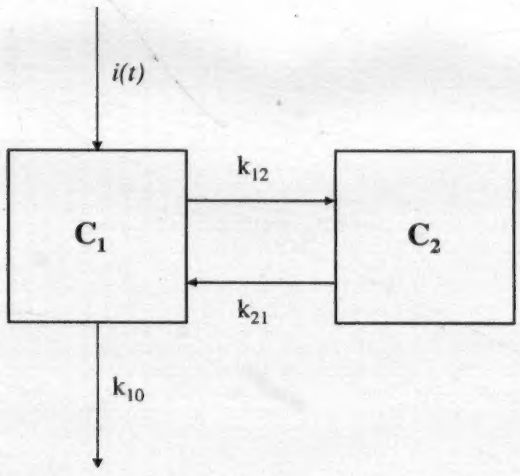

Figure 3.2: A two-compartment mamillary model.

and (3.6) have an exact algebraic solution that is a sum of terms that are exponential in time.

By replacing one or more of the constant kinetic rate coefficients by the fractal equivalent, a fractal compartmental model can be created. For example, by making the substitution $k_{21} = k_{21}t^{-h}$ in Eqs. (3.5) and (3.6), a fractal trapping model is obtained, with a power-law release of drug molecules from compartment 2 back into compartment 1. This Model 2 is expressed mathematically as

$$\dot{C}_1 = k_{21}t^{-h}C_2 - (k_{12} + k_{10})\,C_1 + \frac{i(t)}{V_d}, \tag{3.7}$$

$$\dot{C}_2 = k_{12}C_1 - k_{21}t^{-h}C_2. \tag{3.8}$$

Alternatively, a fractal elimination model can be created from the concatenary configuration shown in Fig. 3.3. Fuite et al. [55] designated compartment 1 as the plasma and compartment 2 as the liver. By making the substitution $k_{20} = k_{20}t^{-h}$, elimination from the liver now occurs at a fractal rate. This case comprises Model 3 and is described

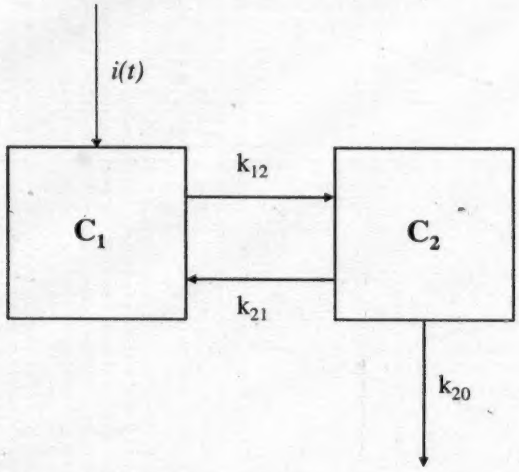

Figure 3.3: A two-compartment catenary model.

by the equations

$$\dot{C}_1 = k_{21}C_2 - k_{12}C_1 + \frac{i(t)}{V_d}, \tag{3.9}$$

$$\dot{C}_2 = k_{12}C_1 - \left(k_{21} + k_{20}t^{-h}\right)C_2. \tag{3.10}$$

The fractal compartmental models are linear, since the kinetics remain first-order. However, the value of the fractal kinetic rate coefficient, and thus the probability of drug release from the fractal compartment, changes with time. Unlike Model 1, the equations for Models 2 and 3 cannot be solved exactly using analytical methods [38].

3.4.4 Simulated Data Sets

Sets of error-free data were generated for each model using parameters (listed in Table 3.1) that were chosen to reproduce real clinical situations. For Models 1 and 2, the values correspond to parameters reported for the anticancer agent carboplatin in pediatric patients [150]. In addition, an arbitrary value of $h = 0.6$ was included for Model 2. The dose and infusion time were taken to be 500 mg and 1.5 h, respectively. Twelve concen-

Table 3.1: Theoretical coefficients for the simulated two-compartment models.

Model	k_{12} (h^{-1})	k_{21} (h^{-1})	k_{10} (h^{-1})	k_{20} (h^{-1})	V_d (L)	h
Classical	1.5	1.1	1.25	-	5.0	-
Fractal trapping	1.5	1.1	1.25	-	5.0	0.6
Fractal elimination	28.0	3.0	-	0.6	10.0	0.8

tration values, C_i, were calculated for times $t_i = 0, 0.5, 1, 1.5, 2, 3, 4, 6, 8, 10, 12,$ and 18 h. Here, C_i refers to the concentration at time t_i. Beyond 18 hours, the concentration falls below the quantification limit of 0.0025 mg $\cdot$ L^{-1} reported for free platinum using atomic absorption spectrometry [71]. Model 3 was fit to mibefradil data [173], and the estimated parameters were used to generate 12 points for times $t_i = 0, 0.8333, 0.1667, 0.25, 0.3333, 0.5, 1, 1.5, 2, 6, 1$ A dose of 25 mg and an infusion time of 0.1667 h was selected for a hypothetical 25-kg dog.

To create sets of realistic, noisy data, (t_i, C_i^*), an independent error value, ϵ_i, was added to each concentration value:

$$C_i^* = C_i + \epsilon_i. \tag{3.11}$$

A Gaussian distribution with zero mean (μ) was assumed for ϵ_i, such that

$$\epsilon_i \sim N\left(0, \sigma^2\right), \tag{3.12}$$

where $N\left(\mu, \sigma^2\right)$ is a normally-distributed random variate with mean μ and variance σ^2. The variance was chosen to induce a coefficient of variation (CV) of 10% [82] in C_i, where

$$CV = \frac{\sigma}{\mu} \times 100\% = \frac{\sigma}{C_i} \times 100\%. \tag{3.13}$$

In order to generate $N\left(0, \sigma_i^2\right)$, the polar form of the Box-Muller method was used

to transform two uniformly-distributed random numbers into two $N(0,1)$ variates [153]. Further modification provides

$$\epsilon_i = N\left(0, \sigma^2\right) = \sigma_i \times N(0,1)\,. \tag{3.14}$$

with $\sigma_i = \left(\frac{CV}{100\%} \times C_i\right)$ from Eq. (3.13). Finally, substituting into Eq. (3.11) yields

$$C_i^* = C_i \left(1 + \left[\frac{CV}{100\%}\right] N(0,1)\right). \tag{3.15}$$

Figure 3.4 shows the range in data points for the three models.

3.5 Results

3.5.1 Optimum Algorithm Parameters

Perhaps the most important step in evaluating the SA algorithm is the development of an appropriate annealing schedule. To ensure successful optimization, the temperature should be lowered slowly enough to find the global minimum but quickly enough to minimize computer run time. For the two-compartment models, it was found that a linear decrease in temperature by a factor R was the most efficient, as compared to exponential or power law functions of T, or a function of the number of iterations. Furthermore, the temperature drop was best achieved when the ratio of the number of iterations at each temperature, m, to the initial temperature, T_0, was 0.10 (with $m = 1$ and $T_0 = 10$) and $R = 0.999$. When $\frac{m}{T_0} = 1.0$, the algorithm failed to converge, and when $\frac{m}{T_0} = 0.01$, the algorithm was inefficient and required more than twice as many iterations. An increase in R to 0.9999 also proved inefficient, while a decrease to 0.99 led to a lower accuracy in the final results.

The choice of appropriate convergence criteria was also investigated. WinNonLin ® monitors the relative change in the objective function. In this work, a modified method based on results of Goffe et al. [64] was developed for PKPhit. Every N_δ iterations,

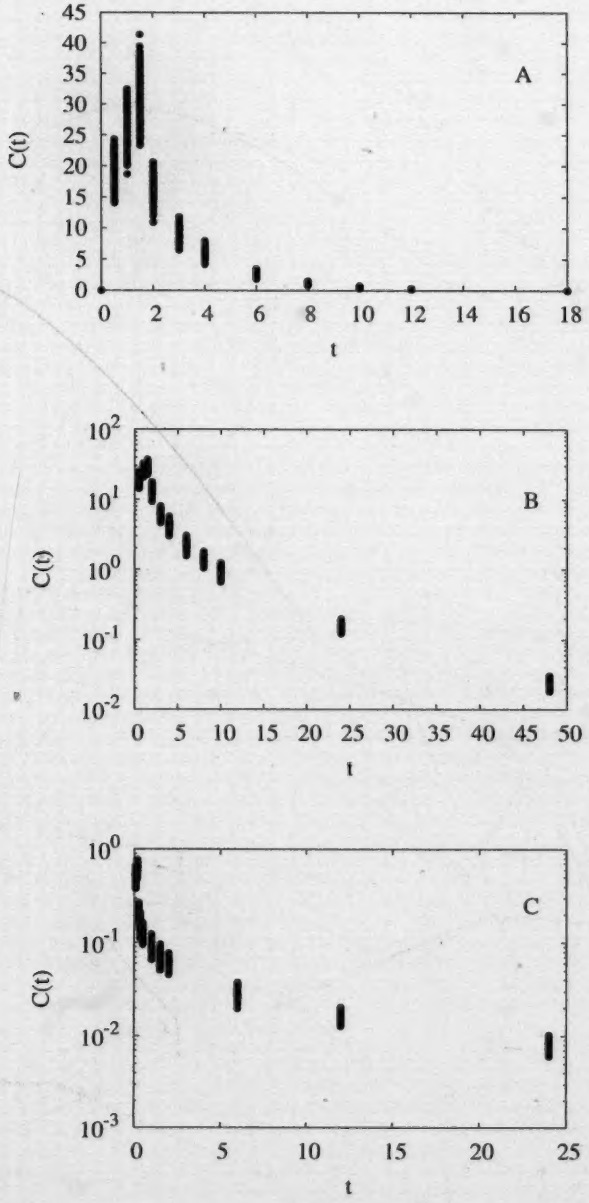

Figure 3.4: The simulated data sets for (a) Model 1, (b) Model 2, and (c) Model 3.

Table 3.2: Annealing schedule.

Parameter	Value
Cycles at step length	20
Iterations at temperature	10
Temperature reduction factor	0.999
Step length adjustor	0.995
Lower bound - kinetic parameters	0.001
Upper bound - kinetic parameters	1000.0
Lower bound - volume of distribution	0.001
Upper bound - volume of distribution	1000.0

Table 3.3: Initial parameter values.

Parameter	Value
Temperature	10
Step length - kinetic parameters	0.01
Step length - volume of distribution	0.1

the average of the previous N_δ accepted values of the objective function was calculated and compared to both the current function value, f_i, and the current optimum value, f_{optimum}. The relative changes were compared to a predetermined value δ, and the algorithm was said to converge if

$$\frac{|f_{\text{previous}} - f_i|}{f_{\text{previous}}} < \delta \tag{3.16}$$

and

$$\frac{|f_{\text{previous}} - f_{\text{optimum}}|}{f_{\text{previous}}} < \delta, \tag{3.17}$$

where

$$f_{\text{previous}} = \frac{\sum_{j=1}^{N_\delta} f_j}{N_\delta}. \tag{3.18}$$

For flexibility in fitting difficult data sets, an additional condition was imposed such

that the total number of iterations did not exceed $N_{\max} = 30,000$. Using the optimum parameters discussed above and values of $N_\delta = 10$ and $\delta = 0.0001$, convergence was found to occur after $15,000 \pm 5,000$ iterations (taking less than a minute on a Pentium 4 computer, 3.2 GHz with 1 G of RAM).

Because it was found that adjusting the step length actually led to longer run times and in many cases an inability to converge, constant step length values were used. A step length of 0.01 to 0.05 was optimal for the kinetic rate parameters and volume of distribution, while a value of 0.001 was ideal for the fractal exponent. When these values were increased, the algorithm quickly found the correct area in parameter space, but subsequently took over 30,000 iterations to narrow in on the optimum. Smaller step lengths resulted in inefficient exploration of the parameter space and the same excess of iterations. The bounds in parameter space were taken to be $0.01 - 10.0$ for the kinetic rate coefficients and volume of distribution, and $0 - 5$ for the fractal exponent; however, widening the ranges, even by a factor of 10^4, had no effect on the progression of the algorithm.

In order to investigate the sensitivity of the SA algorithm to the initial parameter values, Model 1 was fit to a data set 50 times, each time with different values of the random seed and initial model parameter values (randomly chosen over the range $(0, 10]$). The mean WRSS was 0.3389 ± 0.0004, and the coefficient of variation was less than 5% for each of the estimated model parameters. Although the algorithm is most efficient when the range of the initial values is limited, it never failed to reach the global optimum, even when the ranges were extended to $(0, 50]$ and the initial function value was as high as 10^{100}. Consequently, the performance of the SA algorithm is independent of the starting point.

Finally, performing occasional restarts of the program using the current optimum parameter values as the new initial values was not found to be beneficial; the algorithm explored the surrounding space but still converged on the minimum at the same temperature.

3.5.2 Comparison With Other Algorithms

To evaluate the performance of the SA algorithm, the WRSS and model parameter values found by PKPhit for Model 1 were compared to those determined by the Gauss-Newton (Levenberg and Hartley) and Nelder-Mead simplex algorithms as implemented by WinNonLin ® Version 4.1. Table 3.4 lists the results for 50 data sets, the number found to achieve meaningful results since two independent groups of 50 were statistically equivalent (with WRSS values of 0.27 ± 0.10 and 0.28 ± 0.10). The confidence intervals should include the theoretical values used to generate the noise-free data, and this is indeed the case for all of the parameters.

Because the same data and model is involved, the WRSS can be used to compare the goodness of fit of the three algorithms. The WRSS values were the same for all three algorithms, and thus PKPhit performs as well as the commercially-available implementations of the Gauss-Newton and simplex algorithms. However, in order to get the similar degree of accuracy and precision in the Gauss-Newton and simplex results, the initial parameter values had to be within 40% of the actual values, and the lower and upper bounds had to be within an order of magnitude for the Gauss-Newton algorithm and more than twice as narrow again for the simplex algorithm (see Table 3.5). Doubling the range of the parameter bounds for the simplex algorithm resulted in a decrease in the accuracy of the parameter estimates by an average of 30% and an increase in their standard deviation by an average of 140%. In the case of the Gauss-Newton algorithm, simply increasing the initial estimates of the kinetic rate coefficients from $1.0\,h^{-1}$ to $5.0\,h^{-1}$ resulted in an inability of the algorithm to converge to a solution for any of the 100 data sets.

In the extreme case where no initial estimates were provided to WinNonLin, the program was unable to find solutions for 26 of the data sets when using the Gauss-Newton algorithm and 24 of the sets when using the simplex algorithm. Furthermore, although the mean objective functions did not rise significantly, the standard deviations in the parameter estimates increased by $15 - 50\%$ in the Gauss-Newton case and by

Table 3.4: Estimated parameters for the classical two-compartment model. The input parameters necessary for the Gauss-Newton and simplex algorithms are listed in Table 3.5.

Parameter	Theoretical Value		Estimated Value PKPhit	Gauss-Newton	Simplex
k_{12} (h^{-1})	1.5	mean	2.26	2.23	2.48
		SD	0.86	1.06	0.68
		range	0.83 – 4.1	0.68 – 5.5	0.93 – 3.0
k_{21} (h^{-1})	1.1	mean	1.44	1.43	1.47
		SD	0.22	0.18	0.17
		range	0.95 – 2.1	1.1 – 1.9	1.0 – 1.9
k_{10} (h^{-1})	1.25	mean	1.44	1.42	1.51
		SD	0.30	0.35	0.27
		range	0.88 – 2.3	0.87 – 2.7	0.92 – 2.0
V_d (h^{-1})	5.0	mean	4.53	4.64	4.29
		SD	0.93	1.0	0.88
		range	2.7 – 7.3	2.3 – 7.6	3.1 – 7.0
WRSS	-	mean	0.28	0.28	0.28
		SD	0.10	0.11	0.[illegible]
		range	0.11 – 0.50	0.11 – 0.54	0.12 – 0.51

Table 3.5: Initial and bounding parameter values necessary for the Gauss-Newton and simplex algorithms to achieve the accuracy shown in Table 3.4.

Algorithm	Value	k_{ij} (h^{-1})	V_d (L)
Gauss-Newton	Initial	1.0	7.0
	Lower Bound	0.5	0.5
	Upper Bound	10.0	10.0
Simplex	Initial	1.0	7.0
	Lower Bound	0.5	2.0
	Upper Bound	3.0	7.0

Table 3.6: Estimated parameters for Model 2 with fractal trapping.

		Experimental Value		
Parameter	Theoretical Value	Mean	SD	Range
k_{12} (h^{-1})	1.50	1.75	0.75	0.58–4.01
k_{21} (h^{-1})	1.10	1.11	0.32	0.50–1.89
k_{10} (h^{-1})	1.25	1.40	0.28	0.96–2.54
V_d (L)	5.00	4.76	0.94	1.46–6.99
h	0.60	0.58	0.073	0.39–0.72
WRSS	-	0.067	0.043	0.0077–0.20

$50 - 350\%$ in the simplex case. Therefore, although the three algorithms are capable of achieving equivalent model fits, the Gauss-Newton and simplex algorithms require strict initial conditions, whereas the SA algorithm is able to explore the parameter space and focus on the most promising area without prior knowledge of its location.

3.5.3 Applicability to Fractal models

Fifty noisy data sets were generated for Model 2, the fractal trapping model, and Model 3, the fractal elimination model. Based on the performance of PKPhit demonstrated in the previous section, the parameters were estimated using PKPhit, and the results are listed in Tables 3.6 and 3.7, respectively. For both the fractal models, the parameter estimates agree with the predicted values, and the confidence intervals are reasonable. These values are similarly independent of the initial values and bounds of the parameters. In these cases, the WRSS values are strictly the metric for minimization and as such cannot be compared across Tables 3.4 – 3.7.

On a final note, while the WRSS is a good metric for function optimization, we recommend using the Akaike Information Criterion (AIC) and/or the Schwarz-Bayesian Criterion (SBC) to guide selection between different models [105]. These metrics adjust for the number of model parameters and the number of data points.

Table 3.7: Estimated parameters for Model 3 with fractal elimination.

		Experimental Value		
Parameter	Theoretical Value	Mean	SD	Range
k_{12} (h^{-1})	28.0	24.3	2.0	18.3–29.6
k_{21} (h^{-1})	3.00	2.68	0.58	1.42–4.43
k_{20} (h^{-1})	0.6	0.57	0.059	0.43–0.71
V_d (L)	10.0	10.9	1.19	7.8–15.1
h	0.80	0.77	0.056	0.63–0.88
WRSS	-	0.074	0.047	0.0068–0.23

3.6 Conclusion

This chapter introduced the first detailed application of the simulated annealing optimization routine to fit individual pharmacokinetic data. The robustness of the SA algorithm in fitting both classical and fractal compartmental models has been demonstrated. Although a technique was used to modify the step length, a constant step length was found to lead to a more stable solution. Convergence of the SA algorithm was most efficient with a linear decrease in the temperature by a factor $R = 0.999$ every $m = 0.10 \cdot T_0$ iterations and best estimated using the relative decrease in the objective function.

PKPhit always converged towards the global minimum, irrespective of the initial values and bounds of the model parameters, whereas similar fits by the Gauss-Newton and simplex algorithms required estimates of the parameters to within 40% of the actual values as well as narrow parameter ranges. This limitation is significant not only in the case of a new drug, but also for established drugs due to wide ranges in interindividual variability. For example, when Sonnichsen et al. [176] fit a two-compartment model to data for the anticancer agent paclitaxel in 30 pediatric patients, the ranges of values found for three of the parameters were $k_{12} = 2.9 - 47.4\,\mu\text{mol} \cdot \text{h}^{-1}$, $k_{21} = 6.0 - 142.7\,\mu\text{mol} \cdot \text{h}^{-1}$, and $k_{20} = 0.052 - 1.04\,\text{h}^{-1}$.

Due to its versatility and independence on prior knowledge of the parameter values,

the SA algorithm is particularly applicable to fitting fractal models that are not solvable using analytical techniques. Eftaxias et al. [53] found that an SA solution may be further improved by around 5% by subsequent application of the LM algorithm, and this possibility could be investigated in a future study.

Chapter 4

Emergence of Power Laws from Competing Saturable Processes

4.1 Purpose

The objectives of this chapter are (1) to perform power law analysis of pharmacokinetic data for the anticancer agent paclitaxel, and (2) to emphasize the role of the power exponent in the investigation and quantification of nonlinear pharmacokinetics and the elucidation of underlying physiological processes. In addition, it will be tested to see if a correlation exists between different types of power law behaviour.

4.2 Background

One of the biggest challenges in medical oncology is optimizing the dose and dosing schedules of an anticancer drug for a given patient. The concept of linearity in the body's handling of a drug is important, since it indicates that the drug's concentration as well as derived parameters scale simply with both dose and time. Nonlinearity, however, implies that the relationships are less straightforward. In this study, new ways to assess and quantify nonlinear pharmacokinetic behaviour are investigated using power laws,

with emphasis on their origins and applications to the drug paclitaxel.

Paclitaxel [160] is derived from the bark of the Pacific Yew tree and is active against many cancers, including ovarian, breast, head and neck, and non-small cell lung cancers [81]. Because it is poorly water-soluble, the current formulation incorporates the solvents Cremophor EL (CrEL) and dehydrated alcohol. Paclitaxel is typically administered by intravenous infusion over 1, 3, 6, or 24 hours (h). Because a patient may have an anaphylactic reaction to CrEL, alternative formulations of paclitaxel have been introduced, including Genexol-PM [90] and ABI-007 [47].

Paclitaxel is eliminated predominantly through metabolism in the liver by cytochrome P-450 enzymes [128]. Paclitaxel's mechanism of action is by binding to and stabilizing microtubules within cells, leading to the inhibition of cell replication and eventual cell death due to apoptosis [86]. Paclitaxel has a long residence time within the body and can stay trapped in cancer cells for over a week [131]. Paclitaxel is also highly bound to CrEL micelles, plasma proteins, platelets, and red blood cells [77].

Clinical trials indicate that the area under the plasma curve (AUC) and the maximum plasma concentration (C_{max}) for paclitaxel increase disproportionately with an increase in dose. Not surprisingly, compartmental models with linear rate constants have provided less than adequate fits to paclitaxel concentration-time curves. As a result, two- and three-compartment models with both saturable distribution and saturable elimination have been used to model clinical data [60, 88, 176]. Figure 4.1 shows the central plasma compartment, a saturable binding compartment, and an optional linear binding compartment. The saturable distribution has been attributed to either transport [176] or binding [87] processes. Paclitaxel's pharmacodynamic effects correlate best with the duration of time that the plasma concentration remains above a critical value, estimated as $0.05\,\mu$M [60].

4.3 Hypothesis

As discussed in Section 2.6, power law relationships have been found in many pharmacokinetic data sets. These include concentration-time curves with long-time power law tails of the form

$$C(t) \sim t^{-a} \quad \text{for } t > T \tag{2.35}$$

and pharmacokinetic parameters P that vary with dose D through

$$P = cD^{\beta}, \tag{2.36}$$

where c is a proportionality constant and β is the power exponent. In the previous chapter, it was demonstrated that power laws can be generated by a one-compartment model with fractal enzyme-mediated elimination kinetics. In this chapter, it is hypothesized that power law behaviour can also be generated by a multicompartment model with competing saturable processes. Pharmacokinetic data for the drug paclitaxel will be tested for the relationships in Eqs. (2.35) and (2.36).

4.4 Methods

A power law is best identified through a log-log plot, since taking the logarithm of both sides of Eq. (2.33) yields the linear relationship, with the slope of the line is equal to the power exponent. Thus, the existence of a power law can be tested for by performing regression analysis on log-transformed data, with the goodness of fit evaluated using the R^2 metric (a value of 1 corresponding to a perfect fit).

Forty-one sets of concentration-time data from 20 published clinical trial studies were digitized and inferred using Macromedia Fireworks Version 4. The data were tested for power law tails of the form expressed by Eq. (2.35), where T coincides with the end of the intravenous infusion of the drug. The mean number of data points in the tail was 9 ± 2 (minimum of 6 and maximum of 13). Eight sets of AUC and C_{max} data were taken

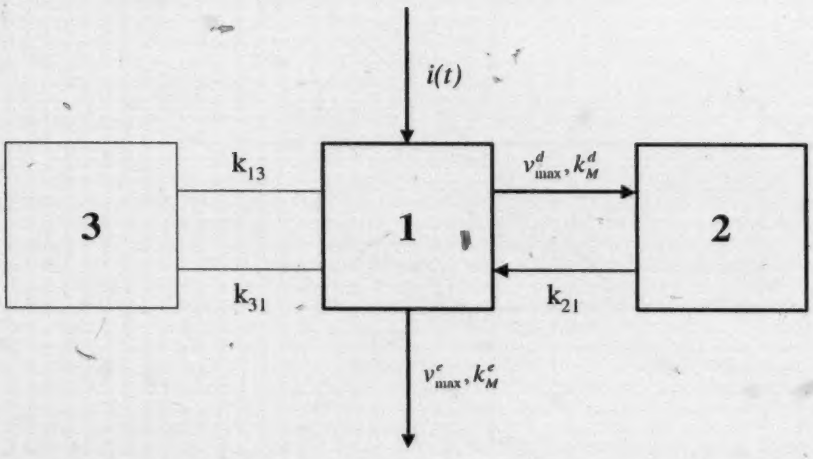

Figure 4.1: A compartment model with both saturable distribution to compartment 2 and saturable elimination from compartment 1, as well as an optional linear binding compartment 3.

directly from 10 published studies and were fit to Eq. (2.36). The mean number of dose levels per study was 4 ± 1 (minimum of 3 and maximum of 6).

Simulations of the two- and three-compartment model illustrated in Fig. 4.1 were performed using code written in C++ to numerically solve the set of ordinary differential equations using a fourth-order Runge-Kutta algorithm [153]. The relevant equations are:

$$\dot{C}_1 = -\frac{v^d_{\max} C_1}{K^d_M + C_1} + k_{12}C_2 - k_{13}C_1 + k_{31}C_3 - \frac{v^e_{\max} C_1}{K^e_M + C_1} + \frac{i(t)}{V_d}, \tag{4.1}$$

$$\dot{C}_2 = \frac{v^d_{\max} C_1}{K^d_M + C_1} - k_{21}C_2, \tag{4.2}$$

$$\dot{C}_3 = k_{13}C_1 - k_{31}C_3. \tag{4.3}$$

For the Michaelis-Menten reactions, the quantity $v_{\max}$ is the maximum reaction rate, and K_M is the concentration at which half the maximum velocity occurs. The superscript d indicates parameters that describe the distribution process, the e superscript indicates the elimination process, $i(t)$ is the input (infusion) function, and V_d is the volume of

Table 4.1: Mean population values reported by Kearns et al. [88] for the three-compartment model parameters.

Parameter		Value
$v^d_{\max}$	(μM $\cdot$ h^{-1})	10.20
K^d_M	(μM)	0.32
k_{12}	(h^{-1})	0.68
$v^e_{\max}$	(μM $\cdot$ h^{-1})	18.80
K^e_M	(μM)	5.50
k_{13}	(h^{-1})	2.20
k_{31}	(h^{-1})	0.65
V_d	(L)	4.00

distribution. The parameter values used were those reported by Kearns et al. [88] and are summarized in Table 4.1. Because the molecular weight of paclitaxel is 853.93 g/mol, the conversion factor between units is 1 mg/L = 1.171 μM. AUC was calculated using Simpson's method, and $C_{\max}$ was simply the largest C value of attained during the Runge-Kutta algorithm.

4.5 Results

4.5.1 Power Law Tails

Thirty-nine of the 41 concentration-time curves exhibited power law tails. Values calculated for the power exponent α are summarized in Table 4.2. Although the exponent was relatively independent of patient characteristics (such as weight, age, sex, and the type and stage of cancer) and the dose level, it varied with the length of the infusion. For short infusions (1-h duration), a single long-time tail was observed with a power exponent of $\alpha = -1.57 \pm 0.14$. The tails persisted up to 24 h and in one case up to 36 h. For long infusions (6-h or 24-h duration), a single long-time tail was also observed but with an exponent of over 3. The tails extended up to 24 h for the 6-h infusions and up to 48 h for the 24-h infusions.

Table 4.2: The power law exponent α quantifying the tail of paclitaxel concentration-time curves.

		Initial Slope		Terminal Slope	
Infusion Time (h)	Number of Data Sets	α	R^2	α	R^2
1	12[a]			-1.57 (0.14)	0.97 (0.02)
3	20[b]	-3.38 (0.27)	0.95 (0.04)	-1.70 (0.16)	0.99 (0.02)
6	3[c]			-3.07 (0.53)	0.96 (0.01)
24	4[d]			-3.23 (0.55)	0.94 (0.08)

[a]Over the dose range 1 50 – 250 mg/m^2, taken from [4, 112, 132].
[b]Over the dose range 1 50 – 250 mg/m^2, taken from [59, 58, 60, 77, 88, 135, 146, 175, 177, 187, 188].
[c]Over the dose range 6 – 30 mg/m^2, taken from [31].
[d]Over the dose range 1 80 – 290 mg/m^2, taken from [149, 176, 198].

In contrast, for the intermediate infusion time of 3 h, the concentration-time curves exhibited a crossover between two power law regimes. At the end of the infusion, there was an initial 1–2 h slope whose power exponent was equal, within error, to that exhibited by the 6-h and 24-h infusion curves. This initial slope was followed by a long-time tail with a power exponent equal, within error, to that exhibited by the 1-h infusion curves. The length of the long-time tail ranged from 9 to 68 h post-infusion. Figure 2 shows the distinct dual nature of the tails for 3-h infusions of paclitaxel. In addition, the rise of each curve also appears to follow a power law relationship. The shape of the curves is an example of a flip-flop situation because the initial slope is steeper than the terminal long-time tail. One would expect the opposite, since smaller plasma concentrations should be cleared more rapidly. Usually, a flip-flop is linked to orally-administered drugs whose absorption is the rate-limiting step [30]. In the case of paclitaxel, however, we believe that the flip-flop is associated with the distribution of drug from the plasma to other tissues.

The observed power law behaviour is likely not a consequence of binding to the CrEL formulation vehicle or blood components. Analysis of two CrEL-free formulations of paclitaxel produced results consistent with those observed for regular paclitaxel. Two

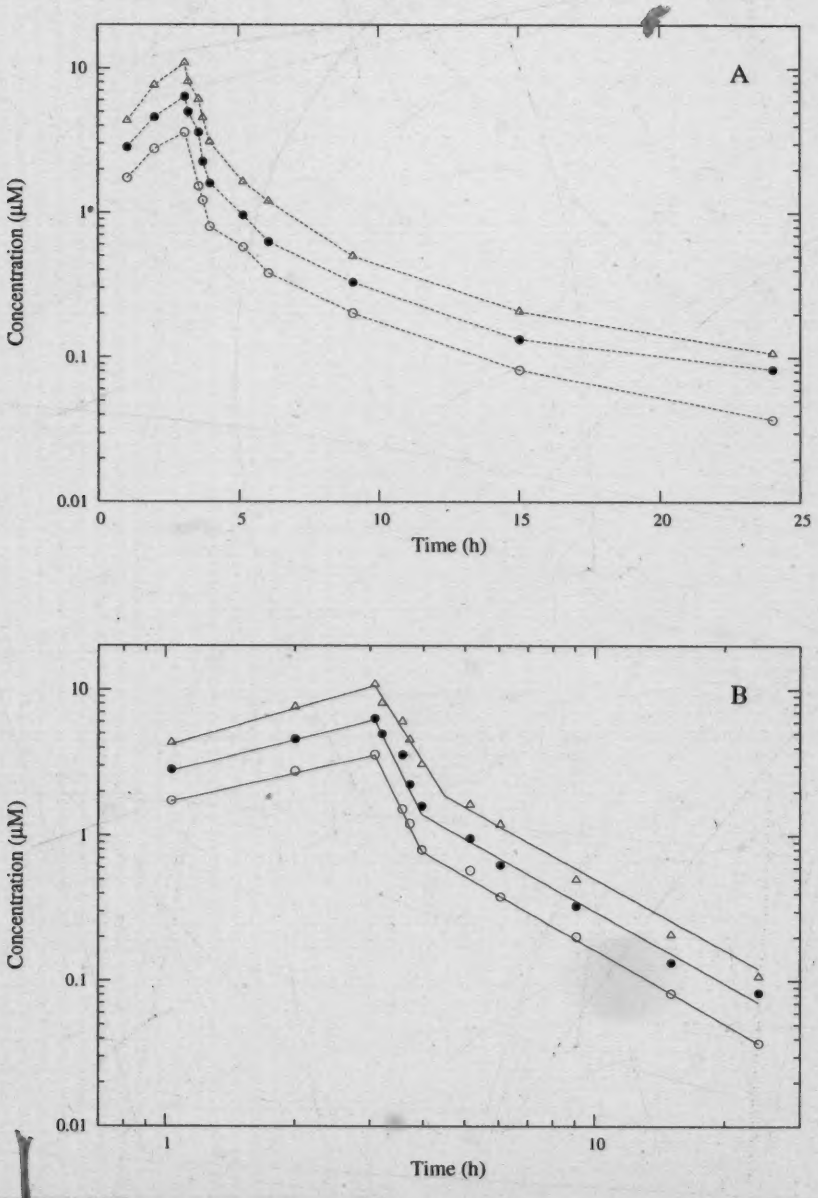

Figure 4.2: Pharmacokinetic data obtained for 3-h infusions of paclitaxel, replotted from Kearns et al. [88] for three dose levels (open circles, 135 mg/m^2; solid circles, 175 mg/m^2; open triangles, 225 mg/m^2). (A) Log-lin plot showing the non-exponential nature of the tails of the curves. (B) Log-log plot showing three distinct power law regions.

concentration-time curves for 30-min infusions of the drug ABI-007 taken from Damascelli et al. (2001) [47] demonstrated single power law tails with $\alpha = -1.61$. Four curves for 3-h infusions of $175 - 390\,\mathrm{mg/m^2}$ of the drug Genexol-PM taken from Kim et al. (2004) [90] exhibited dual power law tails with $\alpha = -4.99 \pm 0.57$ for the initial slope and $\alpha = -1.65 \pm 0.15$ for the terminal slope. The concentration-time curve reported by van Zuylen (2001) [188] for paclitaxel in whole blood following a 3-h infusion produced an initial power exponent of $\alpha = -3.86 \pm 0.59$ and a terminal exponent of $\alpha = -1.64 \pm 0.01$.

We conjecture that the steep curves correspond to the case where the distribution process is not saturated, allowing the maximum fraction of drug to be distributed outside of the plasma. The larger power exponent therefore reflects the maximum transfer of drug outside of the plasma. This situation occurs when the drug is infused relatively slowly. The shallow curves, however, result when the distribution process is saturated, and therefore the smaller power exponent predominantly reflects the elimination process. This situation occurs when the drug is infused relatively rapidly.

The fact that the power law tails persist even at low concentrations (below the reported K_M values) provides additional information about the system. This continued adherence to a power law indicates a failure of the drug to attain a steady state in the peripheral compartment(s). Therefore, drug distribution to and release from the tissues plays a dominant role in the pharmacokinetics of paclitaxel at all plasma concentrations.

4.5.2 Power Law Dose Dependence

The dose-dependence of AUC and C_{max} were found to be nonlinear, in agreement with the literature. The relationship in Eq. (2.36) provided a good fit to the data, and the results are listed in Table 4.3. The two values of β agree within error with each other and with the exponent characterizing the shallow long-time tails. Note that these results are only valid over the therapeutic dose ranges considered, and caution should be used in extrapolating beyond this range.

Table 4.3: The power law exponent β quantifying the dose dependence of pharmacokinetics parameters for 1-h paclitaxel infusions.

Parameter	Number of Data Sets	Dose Range (mg/m^2)	β	R^2
AUC	8 [a]	54–300	1.76 (0.17)	0.94 (0.08)
C_{max}	8 [b]	135–390	1.74 (0.09)	0.92 (0.09)

[a]From [60, 88, 112, 132, 146, 149, 187, 198].
[b]From [60, 88, 112, 132, 146, 159, 198, 199].

4.5.3 Simulations

After confirming the existence of power law tails in paclitaxel concentration-time curves, whether or not they could be generated by the competition between two saturable processes was tested. Simulations of the model shown in Fig. 4.1 did indeed replicate the behaviour. Figure 4.3 shows the shape of the concentration-time curve for different infusion times. For the 3-h infusion, a dual power law is evident. As the infusion time decreases, the initial slope becomes longer and less steep, and it is feasible that a single power law may be observable after short infusion times under certain conditions. Conversely, as the infusion time increases, the initial slope becomes shorter and essentially unobservable, resulting in a single steep power law for the 24-h infusion curve.

An advantage of simulations is that they allow us to study effects of different parameters on the shape of the concentration-time curve. By perturbing the parameter values, it was determined that the duration of the initial steep slope is determined by parameters describing the saturable distribution process, v^d_{max} and K^d_M, while the value of the exponent of the initial slope is determined predominantly by parameters describing the saturable elimination process, v^e_{max} and K^e_M. The slope of the shallow terminal curve is determined mainly by v^d_{max}, where an increase in its value produces an increase in α. This confirms the hypothesis proposed above that the steep curve reflects both the distribution and elimination processes while the shallow curve is dominated by the maximum rate of elimination.

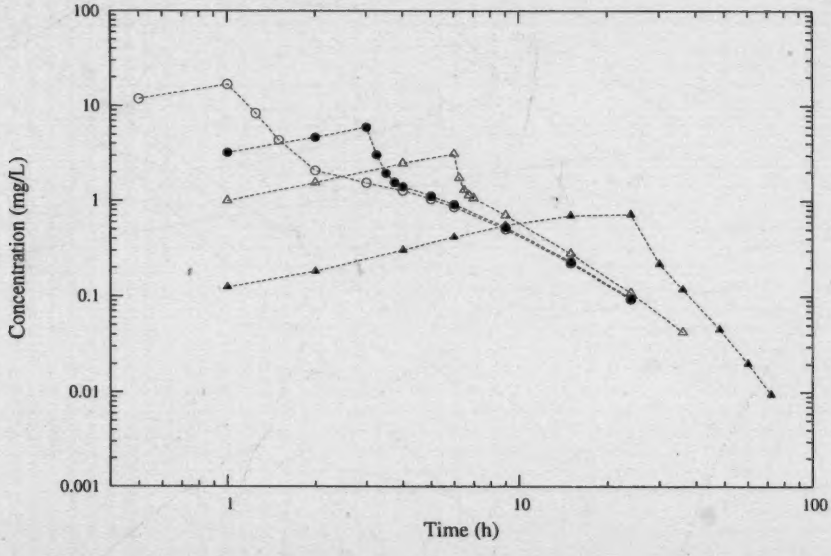

Figure 4.3: The effect of the infusion time (IT) on the shape of the concentration-time curve. (Open circles, IT = 1 h; solid circles, IT = 3 h; open triangles, IT = 6 h; solid triangles, IT = 24 h.)

The inclusion of the third, linear binding compartment was found to have an important effect. For low values of k_{13} (weak binding), the slopes of the two segments remain unchanged, but the duration of the initial slope increases (Fig. 4.4). As k_{13} becomes larger, however, the long-time tail eventually becomes exponential instead of power law. Therefore, an increase in the strength of the linear binding process decreases the plasma concentration and minimizes the effect of the saturable processes.

In the case of paclitaxel, $K_M^d << K_M^e$, and therefore the distribution process saturates before the elimination process. But what occurs when the reverse, $K_M^d >> K_M^e$, is the case? An example is shown in Figure 4.5 for the two-compartment model, and a much wider range of behaviour results. Simply changing the value of $v_{\max}^d$ can produce a single power law tail, a dual curve with an exponential tail, or a dual power law curve with either a steep or shallow terminal tail. A similar transition between different regimes also occurs when the dose increases, the volume of distribution decreases, or k_{21} increases. Therefore, this situation is much more sensitive to changes in the dosing

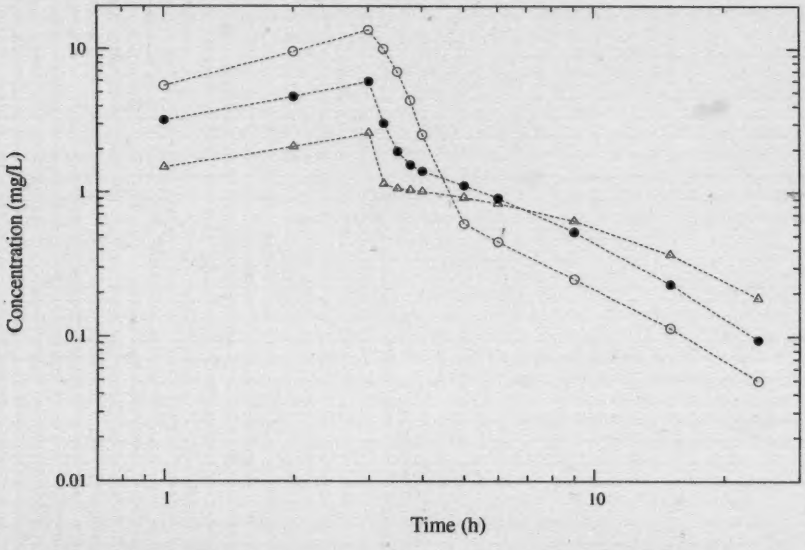

Figure 4.4: The effect of the strength of the linear binding compartment on the shape of the concentration-time curve. The tail becomes exponential for high k_{13} values. (Open circles, $k_{13} = 0\,\mathrm{h}^{-1}$; solid circles, $k_{13} = 2.2\,\mathrm{h}^{-1}$; open triangles, $k_{13} = 8.8\,\mathrm{h}^{-1}$.)

regimen or patient characteristics.

Simulations can also be used to investigate the dose-dependence of AUC and C_{max} beyond the current clinically-relevant range. Both parameters exhibit three distinct regions of dose-dependence on a log-log plot (Fig. 4.6). In both cases, the initial and terminal regions are characterized by approximately $\beta = 1$ (Table 4.4), indicating linear dependence of the concentration on the dose when the system is well below or well above the saturable concentration range. The intermediate regions, however, are characterized by a transition to a nonlinear regime with $\beta > 1$. The curves in Fig. 4.5 fall within this dose range. Because the onset dose of the intermediate slope is higher for AUC than for C_{max}, and the slope persists over a longer range, there appears to be a lag between the occurrence of disproportionately-higher maximum concentrations and an overall noticeable effect on the shape of the concentration-time curve. In summary, power law analysis is helpful in predicting nonlinear kinetics, and Figure 4.6 emphasizes

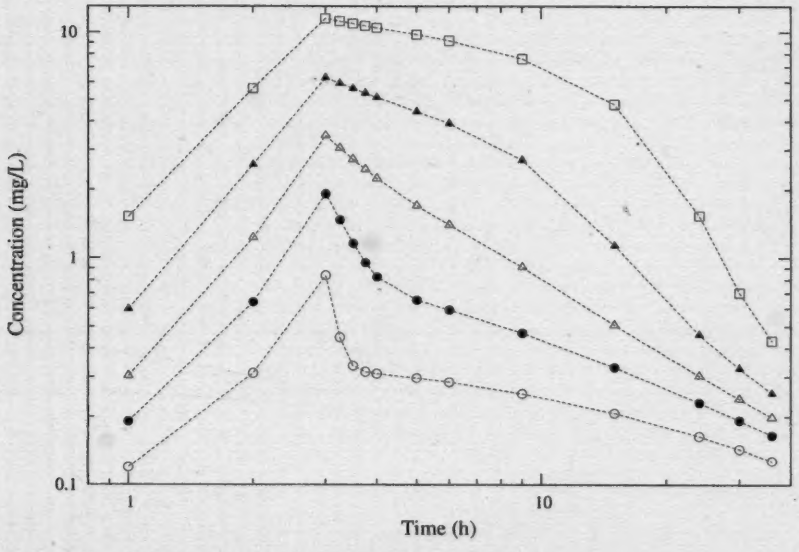

Figure 4.5: The effect of the dose on the shape of the concentration-time curve for a hypothetical two-compartment model with $K_M^d << K_M^e$. (Open circles, 40 mg; solid circles, 50 mg; open triangles, 60 mg; solid triangles, 75 mg; open squares, 100 mg.) The model parameters were $v_{\max}^d = 10.0\,\mathrm{mg \cdot L^{-1} h^{-1}}$, $K_M^d = 0.1\,\mathrm{mg \cdot L^{-1}}$, $k_{21} = 0.5\,\mathrm{h^{-1}}$, $v_{\max}^e = 1.0\,\mathrm{mg \cdot L^{-1} h^{-1}}$, $K_M^e = 5.0\,\mathrm{mg \cdot L^{-1}}$, and $V_d = 5.0\,\mathrm{L}$.

Table 4.4: The power law exponent β describing the graphs in Fig. 4.6.

Parameter	Dose Range mg	β	R^2
AUC	0–10	1.050 (0.006)	1.000
	55–300	3.163 (0.005)	1.000
	> 400	1.0683 (0.0004)	1.000
C_{max}	0–10	1.066 (0.009)	1.000
	20–60	3.67 (0.01)	1.000
	> 150	1.0202 (0.0001)	1.000

that the concept of linearity is valid only over a specified dose range.

Additional simulations were performed to investigate whether a relationship exists between β and α, such that the nonlinear dose-dependence of AUC and C_{max} is correlated with the non-exponential shape of the long-time tail. Figure 4.7 shows that β increases as α decreases; therefore the dose-dependence becomes increasingly disproportionate as the long-time tail becomes more shallow. In other words, the greater the contribution that the tail portion of the curve makes to the overall area under the curve, the greater the increase in AUC with an increase in dose.

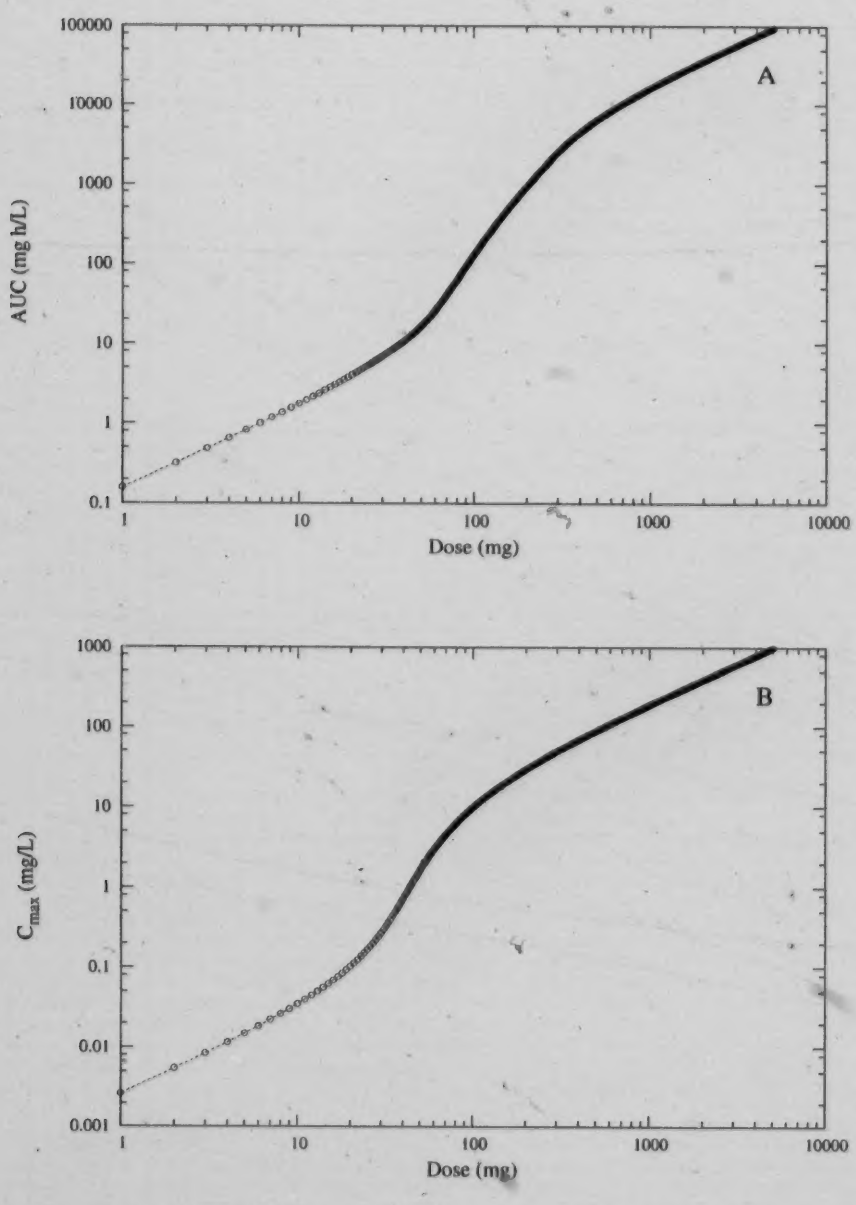

Figure 4.6: The dose-dependence of AUC and C_{max}. The model parameters are those described for Fig. 4.5.

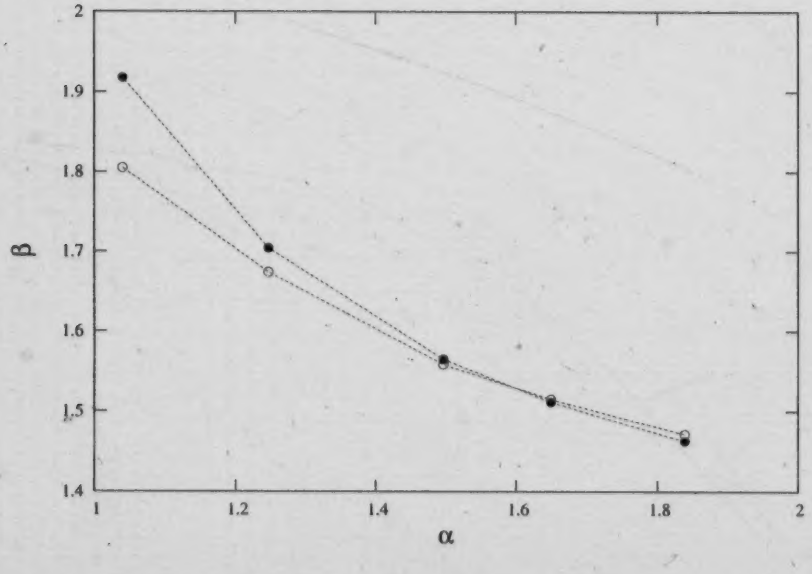

Figure 4.7: The relationship between β and α for a three-compartment model. The value for β was determined for 3-h infusions of 135, 175, 200, 250, and 300 mg/m^2 of paclitaxel (open circles, AUC; solid circles, C_{max}.) The model parameters were $K_M^d = 0.1\,\mathrm{mg \cdot L^{-1}}$, $k_{21} = 0.68\,\mathrm{h^{-1}}$, $v_{max}^e = 18.8\,\mathrm{mg \cdot L^{-1}h^{-1}}$, $K_M^e = 5.5\,\mathrm{mg \cdot L^{-1}}$, $k_{13} = 2.2\,\mathrm{h^{-1}}$, $k_{31} = 0.65\,\mathrm{h^{-1}}$, and $V_d = 4.0\,\mathrm{L}$. The parameter v_{max}^d varied between $5.1\,\mathrm{mg \cdot L^{-1} \cdot h^{-1}}$ and $20.4\,\mathrm{mg \cdot L^{-1} \cdot h^{-1}}$.

4.6 Discussion

The exponent of the power law tail can provide insight into the underlying drug processes. For paclitaxel, only two exponents were found to characterize the behaviour following short, intermediate, and long infusion times. Analysis of power law tails can provide valuable information for clinical applications. For example, longer infusions leading to a steeper tail would theoretically be best for paclitaxel, because they would indicate that a greater portion of the drug is being transferred to the tissues.

An advantage of this proposed mechanism is that it does not place a restriction on the value of α, in contrast to models suggested for the bone-seeking elements, where $-1 < \alpha < 0$ [24], and for fractal kinetics, in which $-1 \leq \alpha \leq 0$ and $d_s \leq 2$ [55].

Power laws can indicate self-similarity, as discussed above. Power law relationships in concentration-time curves may imply that pharmacological processes are linked over different time and/or size scales. To date, allometric scaling has been applied to pharmacokinetics to assess interspecies and intraspecies variation in pharmacokinetic parameters. However, the scaling of pharmacological processes within an individual has yet to be discussed and warrants further investigation.

Furthermore, the identification of power law tails has important consequences for the calculation of pharmacokinetic measures that are extrapolated back from the tail, and it implies that the concept of a terminal half-life does not apply.

4.7 Conclusion

We have shown that two competing saturable processes can generate concentration-time curves with power law tails. To the best of our knowledge, this is the first study to report power law tails in the concentration-time curves of an anticancer drug, as well as the first study to relate the existence of power law tails to saturable processes. Although a single saturable process cannot produce a power law, two competing saturable processes can produce a range of behaviour that includes single and dual power law tails. Furthermore,

although power law tails have been reported for clearance curves, this is the first study to investigate the tails of infusion curves and the dependence of the shape of the curve on the infusion rate.

Before embarking on a full pharmacokinetic analysis, the tails of concentration-time curves can be checked for a power law fit. The existence of a power law tail, especially a shallow one, can signal dose-dependent behaviour. In the case of paclitaxel, a steeper decline is more desirable, since it implies a greater distribution to the tissues as well as a decrease in the extent of nonlinearity. This model is also consistent with observations that the pharmacodynamic effect does not correlate with AUC or C_{max}, since plasma concentrations do not necessarily indicative of the amount of drug still present in the body.

Chapter 5

Fractal Michaelis-Menten Kinetics Under Steady State Conditions

5.1 Purpose

The objective of this chapter is to extend the theory of fractal kinetics to include saturable reactions occurring within heterogeneous media. The theory will be tested using experimental data for the cardiac drug mibefradil.

5.2 Background

In Section 2.5, the theory of fractal kinetics in the transient regime was summarized. Several researchers applied the time-dependent kinetic rate coefficient to the Michaelis-Menten equation; however, as seen in Section 2.4.1, the Michaelis-Menten formalism assumes a steady state regime. In this chapter, an alternative theory for fractal Michaelis-Menten kinetics is presented.

5.2.1 Steady State Fractal Kinetics

As discussed in Section 2.5, the effect of complex geometry on the rate of transient reactions produces an anomalous kinetic rate coefficient. Under steady state conditions, however, Anacker and Kopelman [8] demonstrated that the effect of the geometry is manifested instead as an anomalous reaction order. They showed that the classical equation

$$v = kC \tag{5.1}$$

should be replaced by the effective rate equation

$$v = kC^X, \tag{5.2}$$

where X is a fractal reaction order related to the spectral dimension of the random walk. For example [9],

$$X = \begin{cases} 1 + \frac{2}{d_s} & \text{for } A + A \text{ reactions,} \\ 1 + \frac{4}{d_s} & \text{for } A + B \text{ reactions.} \end{cases} \tag{5.3}$$

These equations have been confirmed using Monte Carlo simulations. Anacker et al. [10] found that $X = 2.44$ for the 2D Sierpinski gasket and $X = 2.01$ as expected for the homogenous cubic lattice. Klymko and Kopleman [92] found that for bimolecular reactions in solids, ranged from the homogeneous value of 2 up to a value of 30. Newhouse and Kopelman [138] found values of $X \approx 5$ for ensembles of 10×10 islands and $X \approx 15$ for ensembles of 5×5 islands. Therefore, as a space becomes more finely divided, as in the example a fractal dust like the Cantor set [113], $d_s \to 0$ and therefore $X \to \infty$.

A form of concentration-dependent fractal kinetics was developed by López-Quintela and Casado [97], who proposed the following scaling relationship:

$$k^{eff} = AC^{1-d_f} \qquad 0 \leq d_f \leq 1, \tag{5.4}$$

where d_f is the fractal dimension of the space. The effective kinetic rate coefficient k^{eff} is therefore assumed to be dependent on the observation scale, here taken to be the concentration. By applying this equation to $v_{\max}$, they obtained the formula

$$v = \frac{v_{\max}^{eff} C^{2-d_f}}{K_M^{eff} + C}, \tag{5.5}$$

where $v_{\max}^{eff}$ and K_M^{eff} are new constants. For $d_f = 1$, the classical Michaelis-Menten equation is recovered, and as $d_f \to 0$, the complexity of the reaction becomes more and more important. Heidel and Maloney [76] performed an analytical exploration of this equation, and initially Macheras [106] and later Ogihara [145] applied it to model carrier-mediated transport under heterogeneous conditions.

A seemingly different approach to concentration-dependent fractal kinetics is the "power-law formalism" developed by Savageau [166], expressed through the generalized mass-action representation:

$$\frac{dC_i}{dt} = \sum_{k=1}^{r} \alpha_{ik} \prod_{j=1}^{n} C_j^{g_{ijk}} - \sum_{k=1}^{r} \beta_{ik} \prod_{j=1}^{n} C_j^{h_{ijk}}, \tag{5.6}$$

where α and β are the kinetic rate coefficients and g and h are the kinetic rate orders associated with each reactant. The equations for the power-law formalism are complicated and Savageau admits that this model works best for large series of reactions rather than of one or more reactions catalyzed by only one enzyme [166]. Savageau justifies his formalism by showing that for homodimeric reactions, its equations are equivalent to the fractal kinetics equations. However, this equivalence has yet to be proven for any other reactions due to the complexity of the equations [170]. In principle, it is possible that Eq. (5.6) can be obtained by summing over several Michaelis-Menten reactions.

To summarize, any reaction for which $h > 0$ or $X > n$ is referred to as following fractal-like kinetics [95]. In this chapter, an alternative formulation of dose-dependent fractal kinetics is proposed based on fractal reaction orders under steady state conditions.

5.3 Model

In a strict sense, a steady state regime means that the concentration of the reactant is constant in time, i.e. $dC/dt = 0$. One way in which this can be achieved is if the concentration of drug molecules is much greater than the concentration of enzymes, even if the local concentration values vary considerably. Even in the presence of drug elimination, a steady state can be maintained due to the recycling of drug molecules by the circulatory system. It is important to distinguish this steady state achieved through recycling from the steady state defined for chronic drug administration. In the latter, drug is administered through multiple doses or a constant infusion, and the elimination rate eventually becomes equal to the infusion rate. The steady state in the current theory can be considered as a local approximation to the same condition.

If the environment is heterogeneous, the system is described by the equations:

$$\frac{dx}{dt} = k_1 \left(e_0 - x\right) C^X - \left(k_{-1} + k_2\right) x, \tag{5.7}$$

$$\frac{dp}{dt} = k_2 x. \tag{5.8}$$

where C is the concentration of the substrate, x is the concentration of the enzyme-substrate complex, and e_0 is the total concentration of enzymes, as introduced in Section 2.4.1. Applying the quasi-steady-state assumption, $dx/dt = 0$, the following equation is derived:

$$v = \frac{v_{\max} C^X}{K_M + C^X}. \tag{5.9}$$

It can be noted that Eq. (5.9) has the same form as the Hill equation that describes the response of a patient or tissue as a function of the drug concentration [133]. Incorporating this formula into a one-compartment model with an IV infusion yields

$$\frac{dC}{dt} = -\frac{v_{\max} C^X}{K_M + C^X} + \frac{i(t)}{V_d}. \tag{5.10}$$

where $i(t)$ is the infusion rate in units of mass/time and V_d is the volume of distribution in units of volume.

5.3.1 Asymptotic Behaviour

To investigate the asymptotics of Eq. (5.10), we consider the model post-infusion. For high concentrations (those occurring well above K_M):

$$\frac{dC}{dt} = -v_{\max}. \tag{5.11}$$

For low concentrations (those occurring far below K_M):

$$\frac{dC}{dt} = -\frac{v_{\max}}{K_M} C^X. \tag{5.12}$$

Integrating Eq. (5.12) leads to the asymptotic power law behaviour

$$C(t) \sim t^{\frac{1}{1-X}}. \tag{5.13}$$

Comparing to Eq. (2.35) yields the relationship

$$\gamma = \frac{1}{1-X} \tag{5.14}$$

or

$$X = 1 - \frac{1}{\gamma}. \tag{5.15}$$

Note that Eqs. (5.13) – (5.15) are undefined for $X = 1$, since this value corresponds to the classical model with an exponential tail, which is inconsistent with a power law.

The fact that the proposed steady state model predicts long-time power law behaviour provides a point of comparison with other models. The solution to a compartmental model with constant coefficients takes the form of a linear superposition of exponential terms, and the resulting concentration-time curve exhibits an exponentially-decaying

tail:

$$C(t) \sim \exp\left[-kt\right]. \tag{5.16}$$

The Michaelis-Menten model predicts an exponential tail:

$$C(t) \sim \exp\left[-\frac{v_{\max}}{K_M}t\right]. \tag{5.17}$$

The transient fractal equation predicts a stretched exponential tail:

$$C(t) \sim exp\left[-kt^{1-h}\right]. \tag{5.18}$$

Finally, the fractal Michaelis-Menten equation (Eq. (2.32)) derived by Kosmidis et al. [96] also predicts a stretched exponential tails of the form

$$C(t) \sim \exp\left[-\frac{v_{\max}}{K_M}t^{1-h}\right]. \tag{5.19}$$

5.4 Methods

Concentration-time data were obtained for the cardiac drug mibefradil [174] in four dogs. The dogs received a dose of 1 mg/kg of mibefradil infused over 10 minutes. The analysis of the data consists of the following steps: (1) quantification of the shape of the tail, (2) comparison of the fit of the proposed model with that of existing models, and (3) testing of the relationship expressed in Eq. (5.15).

The value and standard deviation of the power law tail exponent γ were calculated from the concentration-time curves using linear regression analysis of the log-transformed data.

The models were fit to the data using the simulated annealing algorithm described in Chapter 3. Five one-compartment models were fit to the data sets, and they are summarized in Tale 5.1.

Table 5.1: Summary of models for the enzyme-mediated kinetics of drug elimination.

Model	Abbreviation	Reaction Rate
Fractal [55]	F	$k_0 t^{-h} C$
Michaelis-Menten [126]	MM	$\frac{v_{\max} C}{K_M + C}$
Transient fractal Michaelis-Menten [96]	FMM	$\frac{v_{\max} C}{K_M t^h + C}$
López-Quintela fractal Michaelis-Menten [97]	LQC	$\frac{v_{\max}^{eff} C^{2-d_f}}{K_M^{eff} + C}$
Steady state fractal Michaelis-Menten	SSFMM	$\frac{v_{\max} C^X}{K_M + C^X}$

Table 5.2: The slope γ of the log(concentration) versus log(time) curve between $t = 30$ min and $t = 1440$ min. Values are given as mean (standard deviation).

Dog	γ	R^2
1	-0.702 (0.028)	0.991
2	-0.464 (0.049)	0.927
3	-0.597 (0.024)	0.989
4	-0.705 (0.066)	0.943

5.5 Results

The shape of the tail was determined for the four data sets and was found to be a straight line on a log-log plot, indicating a power law relationship. The values for the power law exponent are listed in Table 5.2. The power law tail extends over three orders of magnitude in time, and the goodness-of-fit represented by the R^2 value is greater than 0.9 for every dog. This result indicates that the SSFMM model is an appropriate model for the data.

The results from the model fits are listed in Table 5.3. The MM model performs

the worst. Furthermore, the values that it predicts for the volume of distribution are unrealistically low for three of the four dogs. In contrast, the V_d values for the other models are reasonable for a dog and are consistent with each other. Furthermore, the K_M values for the MM model are almost two orders of magnitude higher than the values for the LQC, FMM, and SSFMM models. The values for the intrinsic clearance, v_{max}/K_M, are also at least one order of magnitude smaller than those predicted by the other models. These results indicate that classical Michaelis-Menten kinetics does not adequately describe the elimination of mibefradil from the dog.

The LQC, F, and FMM models provide some improvement. However, in the case of the LQC model, the reaction orders of $2 - d_f$ yield values of zero for the fractal dimension, d_f, essentially eliminating the fractal nature of the model. In the case of the F and FMM models, the exponent h takes the maximum value of 1.

The SSFMM model provides the best fit to all data sets. The values for X determined from the model fit were compared to those calculated from the power law tail exponent γ using Eqs. (5.13) and (5.15), and the results are listed in Table 5.4. The values agree within error for all but Dog 1. Figure 5.1 a shows the power law tail for Dog 3, and Figure 5.1 b shows the same data fit by the SSFMM model. The proposed model accurately describes the concentration-curve at all concentration levels.

According to Eq. (5.12), the existence and onset of the power law tail correlate with the value of K_M, and the power law behaviour should only exist for $C << K_M$. The values estimated for K_M range from 800 ng/mL to 7000 ng/mL and are between 30 and 90% higher than the maximum plasma concentrations (556.1 to 1400 ng/mL). Therefore, the power law tails are observable because the dose of mibefradil given to the dogs in this study leads to plasma concentrations well below saturation levels. Furthermore, Eq. (5.12) can be interpreted alternatively in terms of a concentration-dependent $v_{\max}$ of the form $v_{\max}^{eff} = v_{\max} C^{X-1}$. When the approximate Eq. (5.12) was used instead of Eq. (5.9), it resulted in similar parameter values as the SSFMM model but with a poorer fit to the rise of the curve.

Table 5.3: One-compartment parameters for the drug concentration in the jugular vein of dogs following a 10-min infusion of 1 mg/kg of mibefradil.

		Value				
Model	Parameter	Dog 1	Dog 2	Dog 3	Dog 4	Mean
MM	$v_{\max}$ ($\text{ng} \cdot \text{mL}^{-1}\text{min}^{-1}$)	327	4,699	4,737	4,375	
	K_M ($\text{ng} \cdot \text{mL}^{-1}$)	96,593	101,139	100,131	101,046	
	V_d (L)	10.5	0.00369	0.00361	0.00405	
	WRSS	7.27	11.0	11.0	11.0	
	AIC	**31.8**	**37.2**	**37.2**	**37.2**	**35.9**
LQC	$v_{\max}^{eff}$ ($\text{ng} \cdot \text{mL}^{-1}\text{min}^{-1}$)	587	847	363	623	
	K_M^{eff} ($\text{ng} \cdot \text{mL}^{-1}$)	5,323	6,961	4,702	5,693	
	V_d (L)	7.21	8.45	4.64	5.67	
	$2 - D$	2.00	2.00	2.00	2.00	
	WRSS	2.68	4.06	4.15	3.05	
	AIC	**20.8**	**26.2**	**26.5**	**22.5**	**24.0**
F	k_e (min^{-1})	1.01	1.16	1.03	1.21	
	V_d (L)	4.80	4.31	4.95	3.55	
	h	0.999	0.999	0.998	0.998	
	WRSS	2.56	5.33	3.74	4.14	
	AIC	**18.2**	**27.8**	**23.2**	**24.5**	**23.4**
FMM	$v_{\max}$ ($\text{ng} \cdot \text{mL}^{-1}\text{min}^{-1}$)	4,358	3,306	2,486	4,170	
	K_M ($\text{ng} \cdot \text{mL}^{-1}$)	4,623	3,638	2,709	4,401	
	V_d (L)	6.04	11.0	10.1	12.0	
	h	1.00	1.00	1.00	1.00	
	WRSS	2.01	1.82	2.01	2.01	
	AIC	**17.1**	**15.8**	**17.1**	**17.1**	**16.8**
SSFMM	$v_{\max}$ ($\text{ng} \cdot \text{mL}^{-1}\text{min}^{-1}$)	3,575	8,201	3,548	3,817	
	K_M ($\text{ng} \cdot \text{mL}^{-1}$)	5,217	799	6,778	7,098	
	V_d (L)	1.30	2.39	16.5	9.54	
	X	2.56	3.35	2.74	2.61	
	WRSS	0.845	0.263	0.219	0.544	
	AIC	**5.99**	**-9.38**	**-11.7**	**0.0797**	**-3.75**

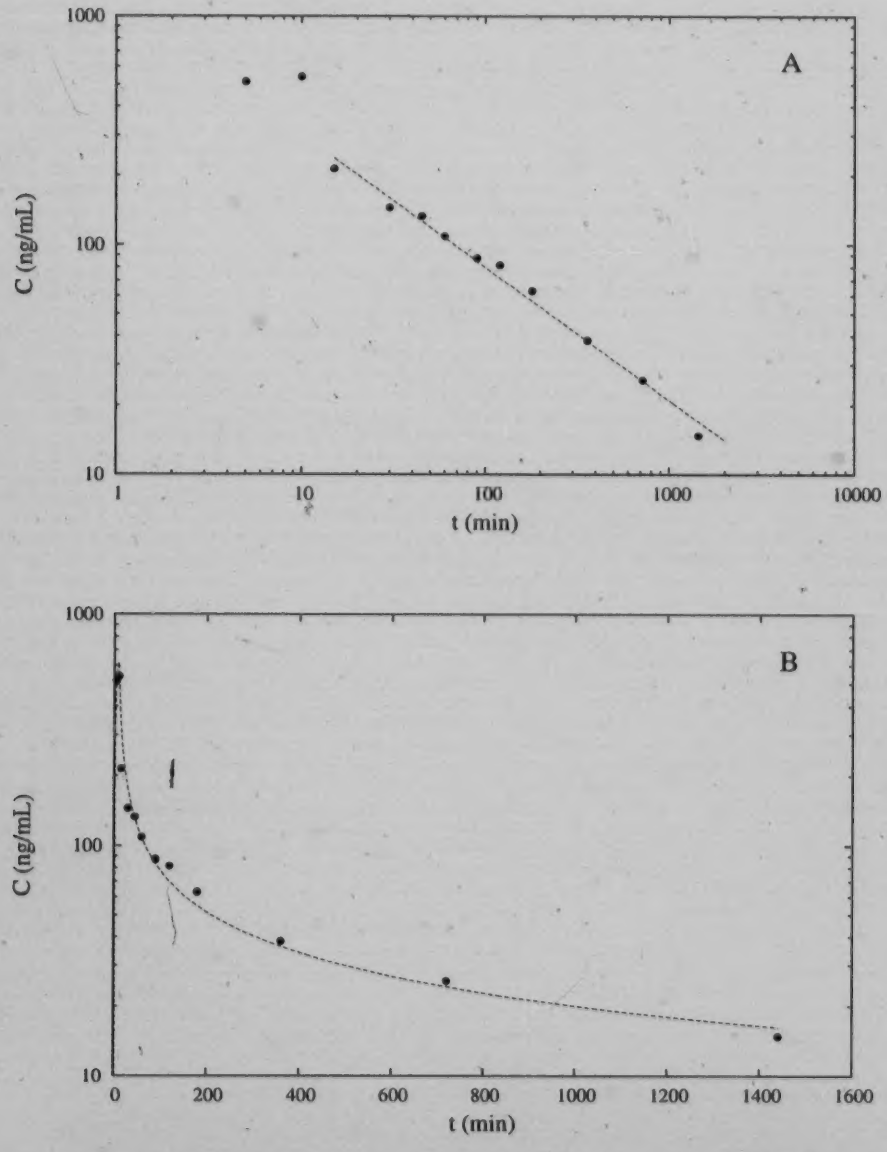

Figure 5.1: Concentration-time curve for mibefradil data for Dog 3. (A) Log-log plot showing the long-time power law tail from 30 min to 1440 min. The dashed line is the regression line with $\gamma = -0.597 \pm 0.024$. (B) The same data but the dashed line now represents the best-fit curve found using the SSFMM model with $X = 2.74$.

Table 5.4: Comparison between the values for the fractal reaction order X predicted from the slope γ and obtained from the model fit.

	X	
Dog	Predicted From γ	Model Value
1	2.42 (0.10)	2.56
2	3.16 (0.33)	3.35
3	2.68 (0.11)	2.74
4	2.41 (0.22)	2.61

5.6 Discussion

One-compartment models are simplifications; however, they can provide an accurate and adequate fit if the distribution of the drug is rapid and equilibrium is achieved quickly in all tissues. In this study, we used a one-compartment model to show that anomalous reaction orders can be a reflection of the heterogeneous nature of the medium under which drug metabolism occurs. Two concepts need to be elaborated upon: the meaning of a steady state and the meaning of noninteger reaction orders.

It is well-known that the liver has a complex geometry. The blood vessels supplying it are arranged as a fractal tree [84], its cellular network has fractal properties [57], and the perfusion of blood at the terminal branches is heterogeneous [195]. Both transient and steady state reactions occurring within such spaces can exhibit anomalous behaviour. For transient reactions, it is assumed that there is a random distribution of reactants [95]. Therefore, anomalous kinetics in the transient case strictly results from the decreased efficiency of random walkers in exploring their irregular space (quantified by d_s). In the steady state regime, however, there is a constant influx of molecules. In regular geometries, this influx can cause a net stirring effect [95]; however, in fractal and confined geometries, self-stirring is inefficient. The spaces are instead characterized by large fluctuations in the local concentration and an increasing segregation of molecules [9]. This effect has been reported for reaction-diffusion phenomena in physical systems [43].

As a result, under steady state conditions, the distribution of molecules is partially ordered due to the influx of molecules, and the nonrandomness reduces the reaction probabilities and consequently the reaction rate. To summarize, transient fractal kinetics occur in well-stirred heterogeneous media while steady state kinetics occur in poorly-stirred heterogeneous media. Here, the term heterogeneity refers to the geometry of the environment.

In the case of steady state fractal kinetics, Klymko and Kopelman [92] interpreted noninteger values of X as characteristic of a microscopically heterogeneous medium that is best described as a collection of kinetically-independent clusters. The kinetic rate coefficients are then kinetic averages taken over domains of different sizes and local concentration. This interpretation is consistent with the studies that reported high X values for reactions occurring on clusters and islands [138, 139]. A similar model can be developed for the liver, the organ predominantly responsible for the elimination of mibefradil from the body. The metabolic enzymes are located in the liver cells, called hepatocytes, which are organized around the terminal supply vessels. Each set of vessels and their surrounding cells are called a sinusoid. Not only does each sinusoid have a different number and distribution of hepatocytes, it receives a different portion of the blood flow. Therefore, the vascular system of the liver can be considered as a network of clusters of sinusoids. Because X increases as the size of the clusters decreases [138], $X = 1$ means that the liver acts as a homogeneous, well-mixed compartment and $X > 1$ indicates segmentation and a lack of mixing.

This interpretation is consistent with a model proposed by Weiss [195], who described the transit times in the liver as being determined by both the micromixing and macromixing processes. He suggested two models at different ends of the spectrum: i) a distributed model in which the sinusoids are parallel and there is complete segregation of the pathways, and ii) a dispersion model in which the sinusoids are interconnected and there is perfect micromixing. Considering our results in this framework, X provides a quantitative measure of the degree of micromixing between sections of the liver and

locates the model somewhere between Weiss's two extreme models.

5.7 Conclusion

This study provides the first application of fractal kinetics under steady state conditions to pharmacokinetics. We have demonstrated that a steady state fractal Michaelis-Menten equation best describes the elimination of the drug mibefradil from dogs. Furthermore, it accounts for the long-time power law behaviour of the concentration through the inclusion of a fractal reaction order, X. This anomalous reaction order suggests that the liver, the organ of elimination for mibefradil, is best treated as a collection of clusters of sinusoids. The higher the value of X, the less mixing that occurs between adjacent sinusoid clusters.

We conclude that transient fractal kinetics is appropriate for describing reactions that occur within well-mixed heterogeneous environments, while steady state fractal kinetics better describes reactions that occur in understirred heterogeneous spaces. The latter can occur due to the continuous influx of drug molecules through recycling in the circulatory system. Finally, although the proposed one-compartment model is sufficient for fitting curves with a single power law tail, curves described by consecutive power laws may require more than one compartment.

Chapter 6

Interacting Random Walk Model

6.1 Purpose

The application of fractal kinetics through compartmental models is deterministic and a measure of the aggregate, macroscopic behaviour of the ensemble of drug molecules. This chapter investigates the relationship between the mean, macroscopic behaviour and the underlying behaviour of individual drug molecules through a stochastic framework. A random walk formalism is developed to relate the macroscopic chemical kinetic behaviour of the ensemble of drug molecules to the microscopic interactions between individual molecules. The model is used to investigate the consequences of nonlinearity and interactions between individual drug molecules.

6.2 Model

From a physical point of view, a group of drug molecules can be treated as a many-body system of identical molecules. The molecules are introduced into a confined, dissipative medium, and they undergo transport and kinetic processes until all of the molecules have been removed from the system. For drugs administered directly into the vascular system, the molecule residence time is determined predominantly by (1) the resistive effect of the temporary trapping of drug molecules in cells and tissues, and (2) the conductive effect

of permanent trapping due to metabolism and excretion.

In the current model, the walk occurs through time on a one-dimensional finite lattice with periodic boundary conditions. For the purpose of this chapter, we consider only two different kinds of lattice sites: plasma (P) transport sites and permanent elimination (E) traps. This is equivalent to assuming that the drug concentration in other tissues is instantaneously in equilibrium with that in the plasma. Drug molecules are introduced onto P sites and undergo a sequence of sojourn times in P sites until they are removed from an E site. The residence time of a molecule is denoted θ and can be expressed simply as

$$\theta = \sum_{i=1}^{q} \hat{\tau}_i, \tag{6.1}$$

where $\hat{\tau}_i$ is an individual sojourn time in a P site and q is the total number of sojourns. Because θ is a macroscopic quantity and $\hat{\tau}$ is a microscopic quantity, Eq. (6.1) represents a simple statistical mechanical view of the drug residence time. For the current study, in order to isolate the dynamics of the elimination process, the plasma sojourn time was taken to be constant and equal to 3 time steps. In addition, molecules remained in E sites for 3 time steps before being removed from the lattice.

If each walker is independent, the total number of walkers will decrease exponentially in time. However, if the walkers are allowed to interact, anomalous behavior can result. To test whether interactions can reproduce fractal kinetics, both short-term and long-term correlations were introduced into the model using a saturable process and walk constraints. Although heterogeneity is typically incorporated into random walk models explicitly through a waiting time distribution $\psi(t)$ at each site, we instead indirectly generate $\psi(t)$ using these interactions to affect the accessibility and availability of E sites. The waiting time distribution is therefore a "waiting time to exit the body", and the model is hopping-controlled instead of trap-controlled.

This model can be mapped onto a stochastic compartmental model, with all the sites of a given type being interpreted as forming a "compartment" and the transfer between

P and E sites being governed by a PDF. However, the random walk model has a greater degree of flexibility in handling interactions between molecules.

A C++ program was written using Microsoft Visual C++.net (Redmond, WA) with a DrugMolecule class and a DrugSite class. An instance of the DrugMolecule class was created for each molecule to keep track of its plasma sojourn time, θ, number of plasma hits, N_P, and current location and site type. An instance of the DrugSite class was created for each lattice site to hold information about its location, type, and occupation status.

The Monte Carlo algorithm proceeds as follows:

1. An L-length array $\{s_0, s_1, \ldots, s_L\}$ is created to represent the lattice, with s_i representing the type of site at the i-th position. The site types are distributed randomly along the lattice according to the fractions f_i of the total number of sites of type i (equal to P or E).

2. An N-length array $\{d_0, d_1, \ldots, d_N\}$ of drug molecules is created to track the position of each molecule.

3. To institute the CTRW formalism, an M-length sorted list $\{t_0, t_1, \ldots, t_M\}$ is created to hold the update times of the molecules. The update time is equal to the current time plus the sojourn time associated with the type of site a molecule currently occupies. The list is sorted in increasing order in time, so that t_0 is the next time at which the system will advance.

4. The clock, which runs in Monte Carlo time steps, is set to zero. The molecules are initially assigned to random P sites, and the sorted list is populated with update times equal to 3 time steps. Multiple occupancy of any site is not allowed.

5. The clock is moved forward to equal t_0, and the molecule associated with that update time is selected.

6. If the molecule is at an E site, it is removed from the system. Otherwise, a new

site is chosen according to the sampling rules (c.f. Section 6.3.2). If the new site is unoccupied, the molecule moves to that site. If the site is occupied, the molecule remains at its current site. A new update time is generated for the molecule and added to the sorted list.

7. Steps 5 and 6 are repeated until all of the molecules have been removed from the lattice.

At intervals of n_{update} moves, the elapsed time and occupation number, X_i, for each site type are recorded. The occupation number plays the role of drug concentration. Unless otherwise indicated, the model parameters for the current study were chosen to be $L = 200,000$, $N = 10,000$, $f_E = 0.05$, and $f_P = 0.95$.

6.3 Reproducing Elimination Kinetics

6.3.1 Michaelis-Menten kinetics

In order to simulate Michaelis-Menten kinetics, molecules were allowed to jump anywhere on the lattice. However, although a molecule always moved to an empty P site, it was only moved to an empty E site if a random number drawn on $[0, 1]$ was less than the probability $p(N_e)$. The quantity N_e is the number of currently occupied E sites. To satisfy the condition that p is 1 for low values of N_e and 0 for $N_e = N_e^{\max}$, the probability distribution was chosen to have the form

$$p(N_e) = 1 - \left(\frac{N_e}{N_e^{\max}}\right)^2 \qquad 0 \le N_e \le N_e^{\max}. \tag{6.2}$$

Figure 6.1 shows $p(N_e)$ for different values of $N_e^{\max}$. The effect of increasing $N_e^{\max}$ is to increase both $v_{\max}$ and K_M. Figure 6.2 confirms that this distribution produces the correct behavior; the plot of $\dot{X}_P$ as a function of X_P is hyperbolic and the Lineweaver-Burk plot (Eq. (2.28)) is linear.

Figure 6.3 shows a plot of X_P following a bolus dose. The transition to linear kinetics

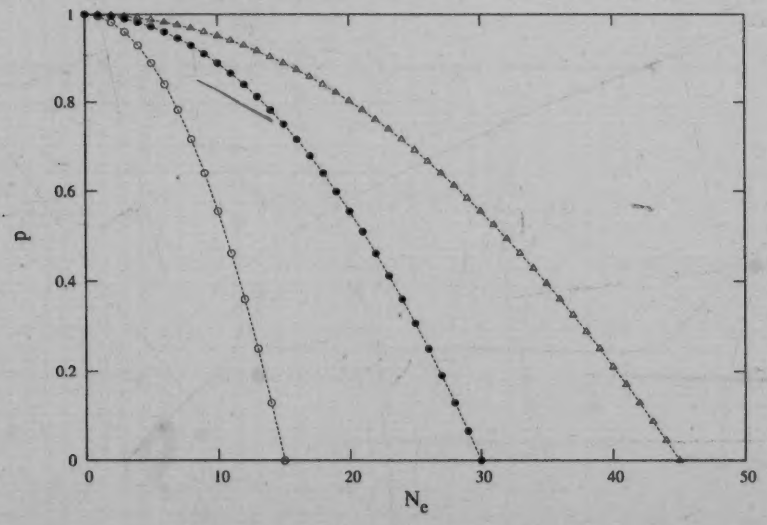

Figure 6.1: The probability p that a molecule will move to an empty elimination (E) site, given the number N_e of currently populated E sites, with $N_e^{\max} = 15$ (open circles), $N_e^{\max} = 30$ (solid circles), and $N_e^{\max} = 45$ (open triangles).

occurs at approximately $X_P = 2,000$ molecules. Because this interaction only persists for the duration of the E site sojourn time (3 time steps), this saturation effect is an example of a short-term correlation between the molecules.

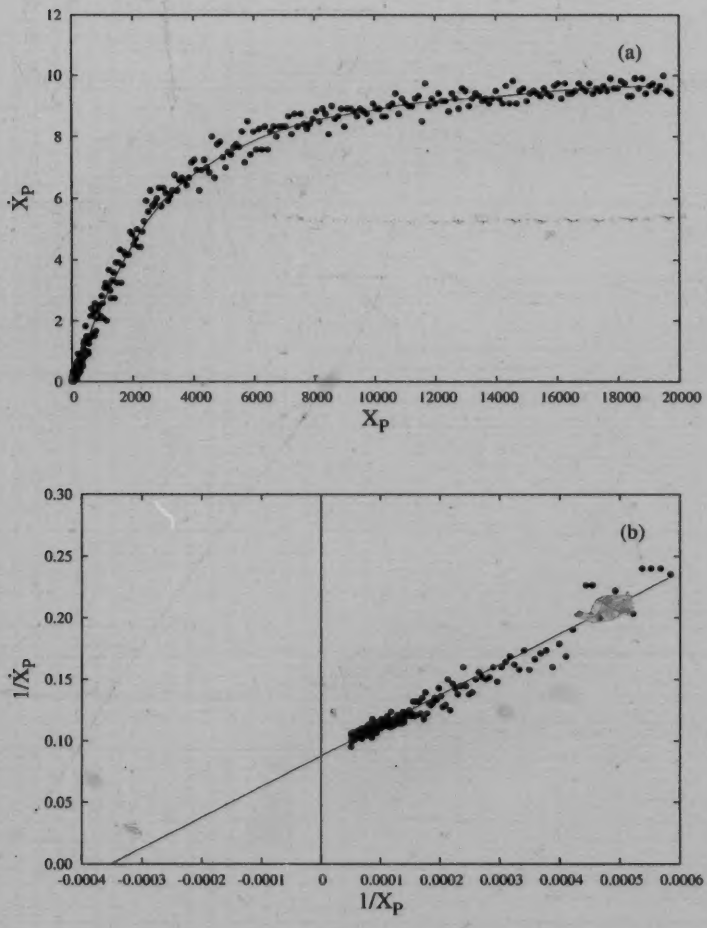

Figure 6.2: (a) Reaction rate as a function of plasma occupation with $N_e^{\max} = 30$. The solid line represents a moving-average trendline. (b) Reciprocal Lineweaver-Burk plot of the same data. The solid line represents the best-fit obtained by regression analysis, with corresponding values of $v_{\max} = 1.14 \pm 0.01$ and $K_M = 317 \pm 8$ ($R^2 = 0.958$).

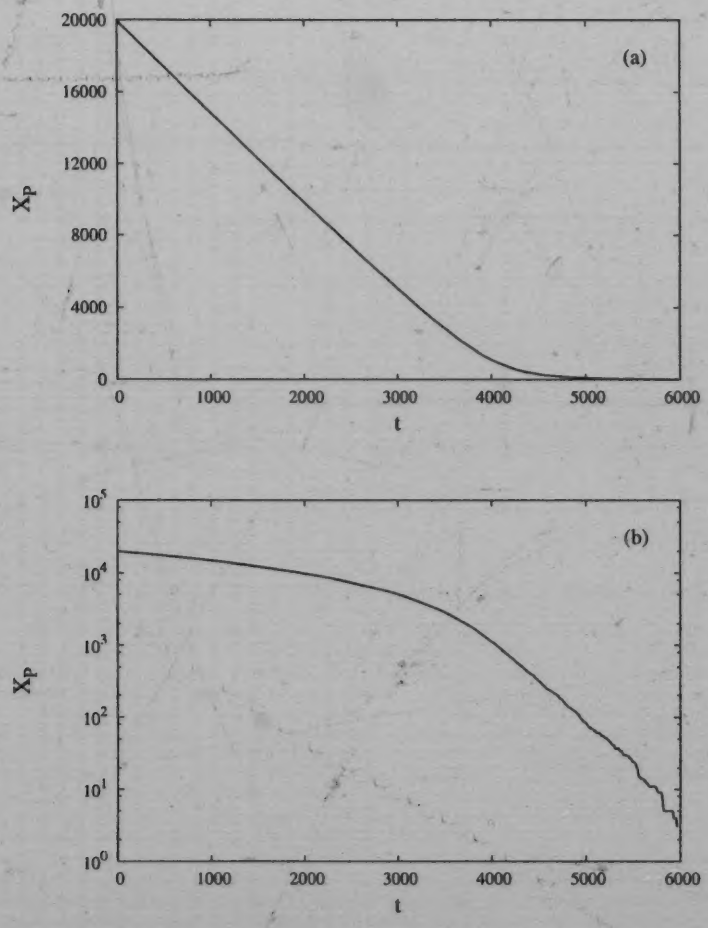

Figure 6.3: (a) The plasma occupation following a bolus dose of 10,000 drug molecules undergoing short-term interactions. (b) The decline is first linear and then transitions to exponential.

6.3.2 Fractal-like kinetics

Transient fractal-like kinetics can be introduced into the random walk model by limiting the movement of molecules along the lattice. For a simple random walk in which the molecules can jump to any site on the lattice, there is a constant probability (equal to f_E) that a molecule is eliminated at a given time. The probability is independent of the time that a molecule has spent in P sites, or its "age". In addition, the compartments are homogeneous and well-mixed, and the system lacks memory.

However, if the molecules are restricted to nearest-neighbor moves, the probability of elimination is no longer constant. Clusters of molecules will begin to form along the lattice, and the interior molecules will have limited mobility. The more interior a molecule is within a cluster, the more time must elapse before it will be able to move and access an E site. Therefore, clustering creates an age-dependent effect. To implement this modification in the interacting random walk model, molecules were only allowed to move a maximum of Ω sites in either direction along the lattice. For large Ω (> 50), the simple random walk and classical kinetics were recovered.

This type of heterogeneity leading to age-discrimination in the elimination process mimics understirred compartments [122]. The lower the value of Ω, the less efficient the mixing process. A physiological analogy can be made to a drug that is transported through the bloodstream and eliminated from the liver. Access to an enzyme site in the liver will depend not only on the blood flow to the liver, but also on the degree of mixing within the sinusoids and the transport into the hepatocytes. The rate of reactions occurring within poorly-mixed environments has been shown to be slowed down in both regular and disordered environments [9, 14, 139].

To the best of our knowledge, this type of stochastic pharmacokinetics model is unique in its use of both saturable and clustering processes. Although Matis and Wehrly [121] studied a stochastic model with clustering effects, the purpose was to mimic situations in which drug molecules can adhere to each other or to a foreign object, so the elimination probability was the same for all molecules within a cluster.

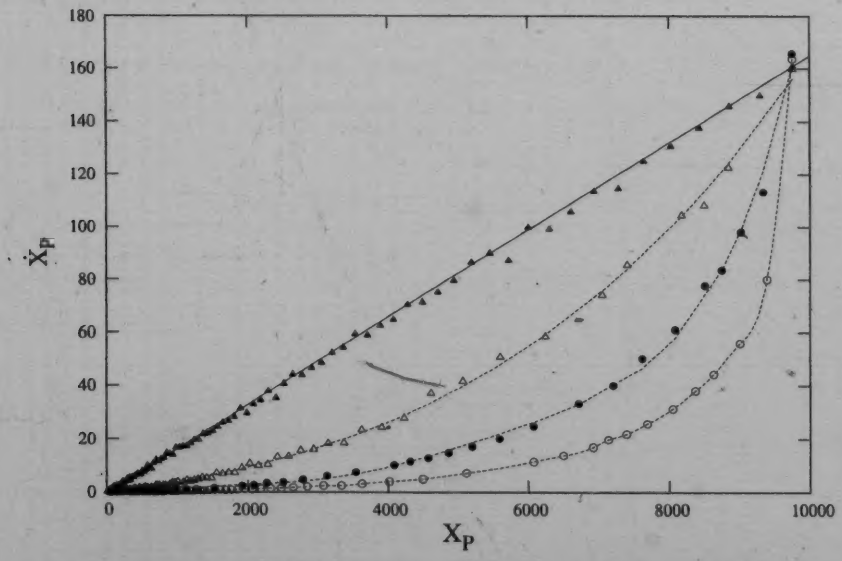

Figure 6.4: Reaction rate as a function of plasma occupation following a bolus dose of 10,000 molecules undergoing short-term interactions with $N_e^{\max} = 15$ and $\Omega = 100$ (closed triangles), $\Omega = 5$ (open triangles), $\Omega = 2$ (closed circles), and $\Omega = 1$ (open circles). The $\dot{X}_P$ and X_P values were averaged over 5 runs.

Figure 6.4 shows the effect of Ω on the reaction rate. At the maximum plasma occupation, the rates are the same. However, as the concentration drops, the rate corresponding to $\Omega = 100$ drops linearly, while the rates corresponding to low Ω values decrease more drastically as clusters form and then eventually taper off as the clusters disperse. Because the rate never regains the value of the simple random walk, this suggest a long-time persistence of correlations between the molecules due to the formation and dispersion of clusters.

Figure 6.5 shows the plasma occupation curve following a bolus dose with $\Omega = 1$. The curve exhibits a long-time tail that is best described by a stretched exponential in time. To confirm that this behaviour is consistent with transient fractal-like kinetics, k (calculated as $[dX_P/dt]/X_P$), was plotted as a function of time (Fig. 6.6). A power law dependence was found, as predicted by Eq. 2.29, with $h \cong -0.569 \pm 0.014$ ($R^2 = 0.965$).

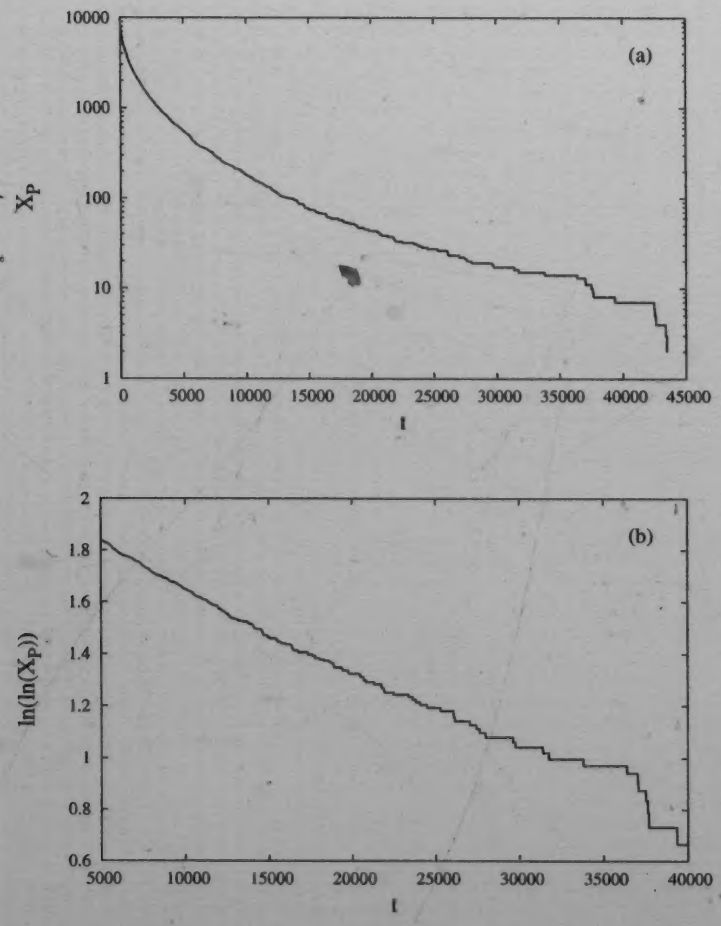

Figure 6.5: (a) The plasma occupation following a bolus dose of 10,000 drug molecules undergoing long-term interactions ($\Omega = 1$). (b) The decline follows a stretched exponential.

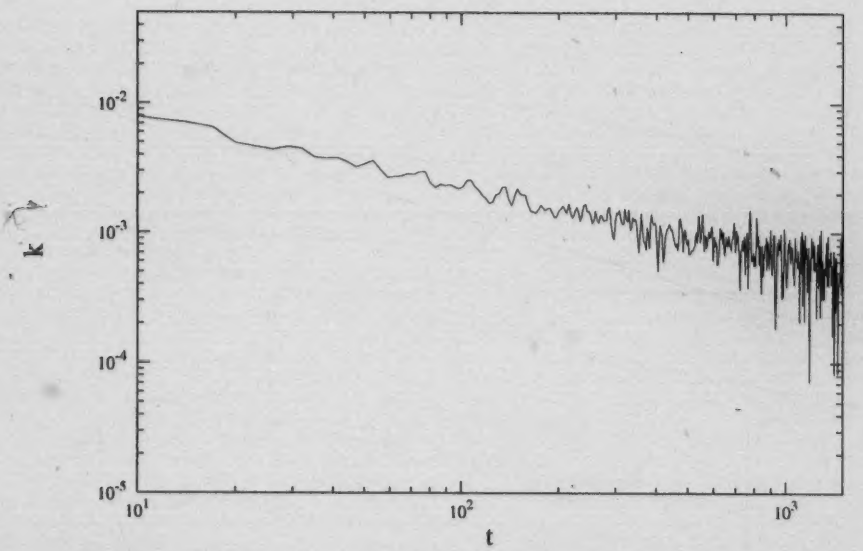

Figure 6.6: The power law dependence of k on t for a lattice with long-term correlations ($\Omega = 1$).

6.3.3 Fractal-like Michaelis-Menten kinetics

When simulations were performed in the presence of both short-term and long-term interactions, the plasma occupation decreased in a biphasic manner (Fig. 6.7). There was an initial linear decline followed by a long-time power law tail. This result is consistent with both Eq. (5.9) and experimental results found for the drug mibefradil [117]. The mean value of the power law tail exponent calculated between $t = 1,000$ and $t = 100,000$ and averaged over 10 runs was $\gamma = -1.414 \pm 0.005$ ($R^2 = 0.995 \pm 0.005$). Therefore, steady state fractal Michaelis-Menten kinetics are consistent with a combination of short-term and long-term interactions between drug molecules.

The PDF for θ was calculated for the process illustrated in Fig. 6.7 using 10,000 drug molecules. The function has a long-time power law tail (Fig. 6.8) with an exponent of -2.46 ± 0.04 ($R^2 = 0.993$), which is equal to $\gamma + 1$. The number of sojourn times will follow the same distribution, just scaled by the sojourn time.

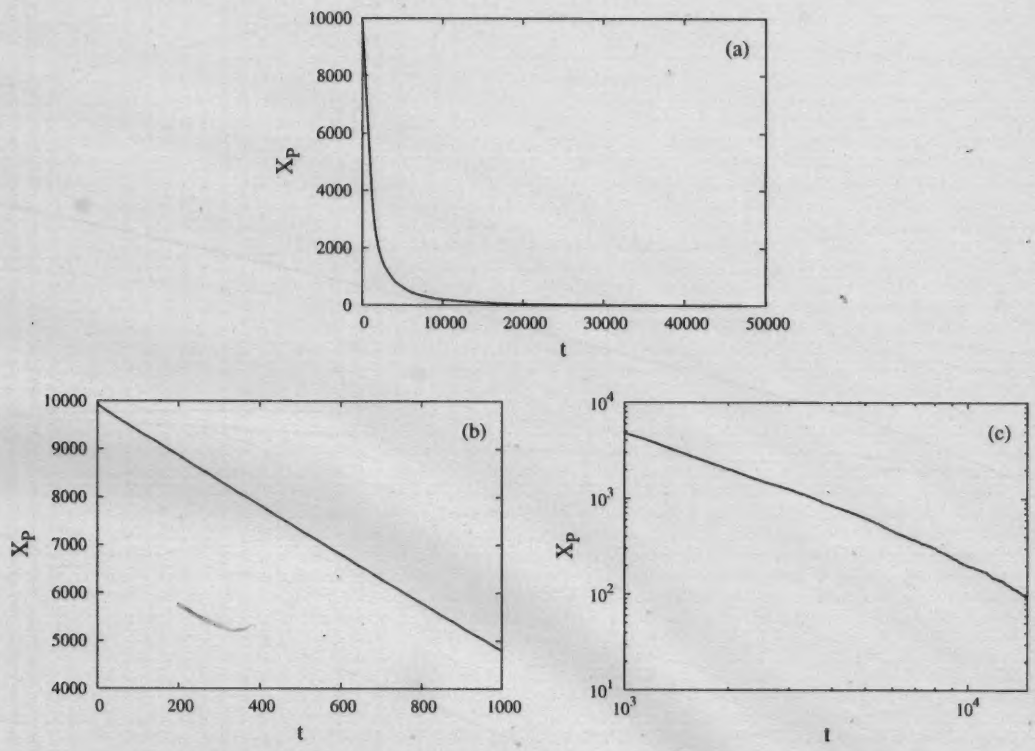

Figure 6.7: (a) The plasma occupation following a bolus dose of 10,000 molecules undergoing both short-term and long-term correlations ($N_e^{\max=15}$ and $\Omega = 1$). The decline is (b) first linear and then transitions to (c) a power law.

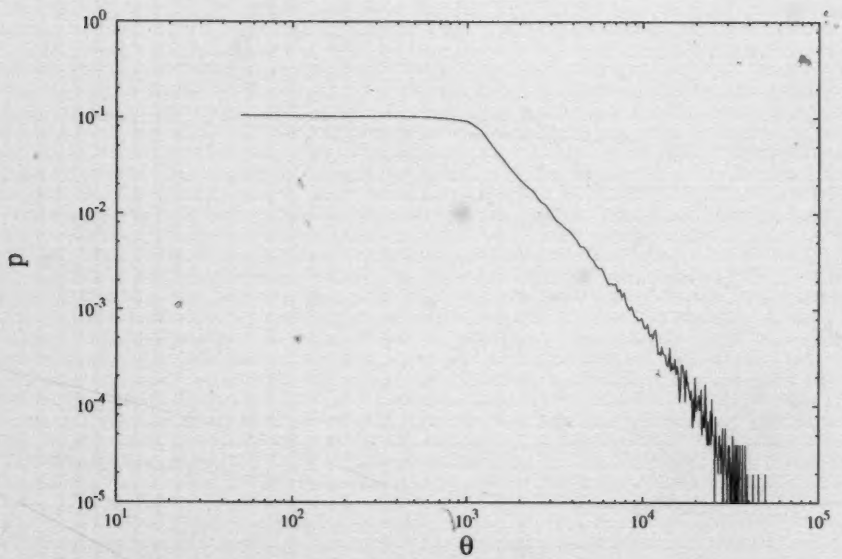

Figure 6.8: The probability distribution of drug residence times θ for a system undergoing combined short- and long-term interactions ($N_e^{\max} = 15$ and $\Omega = 1$).

6.3.4 Infusion curves

A drug can be infused over time instead of administered as a bolus dose. The infusion rate is given as molecules per time step. This is especially important in the case of saturable kinetics, since lower infusion rates can lead to a greater systemic exposure to the drug and potentially a greater dose to the target. It was found that linear and fractal kinetics produced dose-independent AUC values (Fig. 6.9 (a), while Michaelis-Menten elimination kinetics produced nonlinear dose-dependent AUC values. For the case of fractal-like Michaelis-Menten kinetics, the AUC values were similar to those for fractal kinetics at low infusion rates but rose to mirror those of the Michaelis-Menten regime at high infusion rates. By far the highest systemic exposure corresponded to the fractal-like Michaelis-Menten elimination regime.

The maximum plasma concentration, $X_P^{\max}$, was linearly dependent for the case of linear elimination, but was nonlinearly dependent on the infusion rate for the other three types of elimination kinetics. Again, the fractal-like Michaelis-Menten case followed the fractal-like behaviour at low infusion rates but followed the Michaelis-Menten behaviour at high infusion rates.

In addition, the inclusion of the long-term correlations between the molecules precluded the reaching of a steady state. Figure 6.10 (a) shows a steady state for Michaelis-Menten elimination kinetics while Figure 6.10 (b) shows that no steady state is achieved when the kinetics are fractal-like Michaelis-Menten.

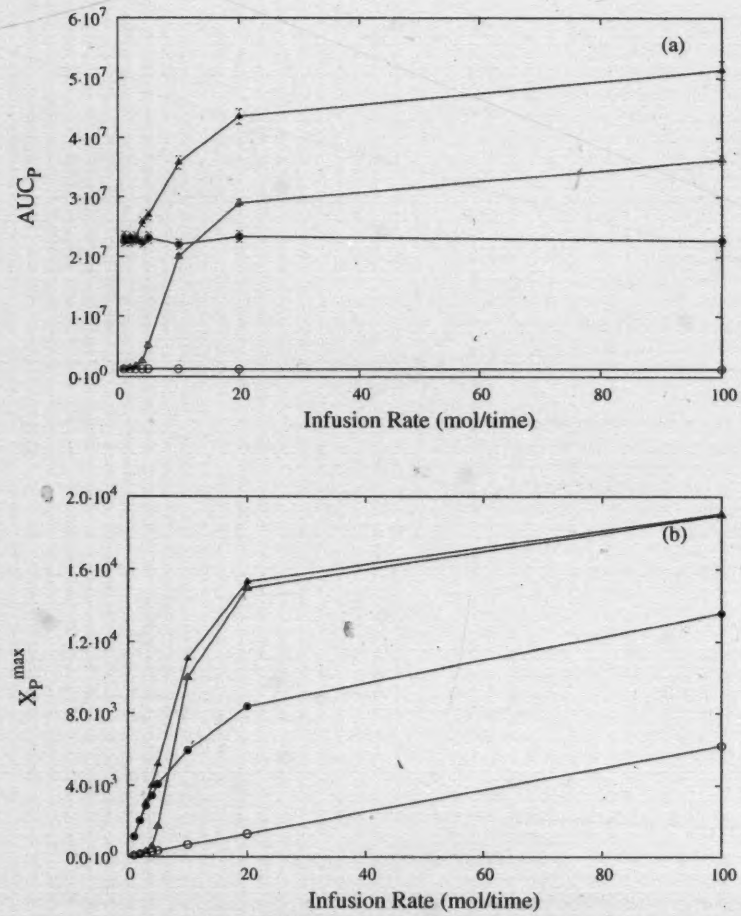

Figure 6.9: (a) Area under the plasma curve and (b) the maximum plasma concentration as a function of the infusion rate for a system with no temporary traps and elimination following linear (open circles), fractal (solid circles), Michaelis-Menten (open triangles), or fractal Michaelis-Menten (solid triangles) elimination kinetics.

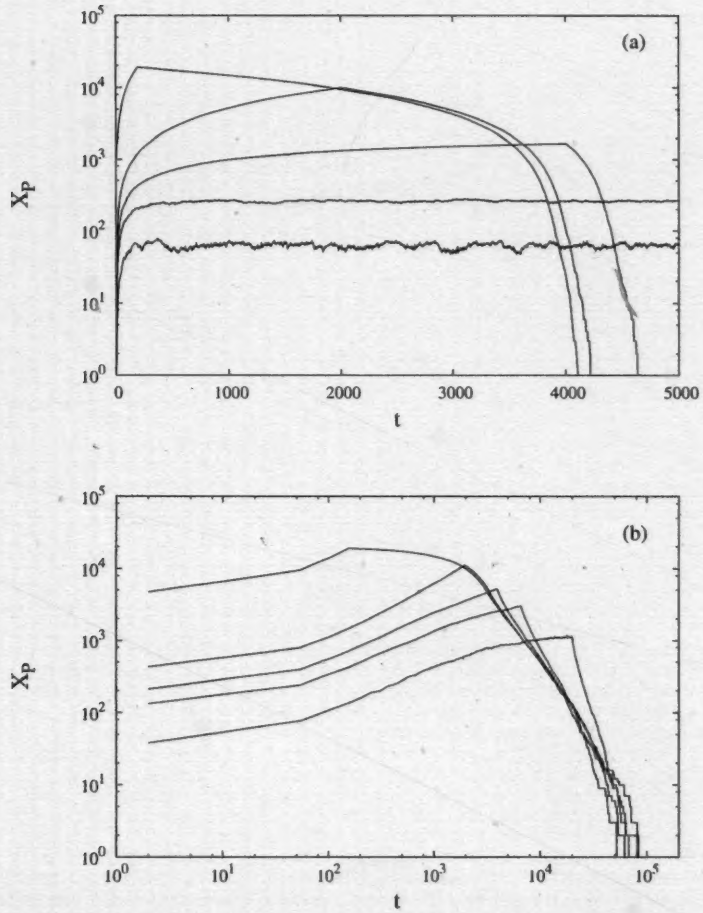

Figure 6.10: Plasma occupation curves for a system with (a) Michaelis-Menten elimination kinetics and (b) fractal Michaelis-Menten kinetics. The infusion rate is, from top to bottom: 100, 10, 5, 3, and 1 molecule per time step

6.4 Conclusion

A continuous time random walk model was used to describe the residence time of drug molecules undergoing a series of sojourn times in the body before being permanently eliminated under either homogeneous or heterogeneous conditions. It was shown that short-term correlations between drug molecules lead to Michaelis-Menten kinetics while long-term correlations lead to transient fractal-like kinetics. By combining both types of correlation, fractal-like Michaelis-Menten kinetics were achieved, and the simulations confirm the analytical results derived in Section 5.2.1.

Chapter 7

Continuous Time Random Walk Model With Lévy Flights

7.1 Purpose

In previous chapters, fractal kinetics were used to model the effects of spatial heterogeneity on the progress of a reaction. In this chapter, the case of temporal heterogeneity is considered, in the form of Non-Gaussian trapping times. The interacting random walk model from Chapter 6 is expanded into a continuous time random walk (CTRW) model that can accommodate Lévy-distributed trapping times. The results provide an alternative model for concentration-time curves with power law tails as well as a way to investigate the interplay between temporary and permanent trapping mechanisms.

7.2 Background

Lévy statistics involve random variables with such broad distributions that the usual Central Limit Theorem does not hold. In this chapter, the argument is made that such a broad distribution can also be found in the behaviour of some drugs, especially when there is a small but finite probability that a drug molecule remains trapped in the body

for a long period of time.

7.2.1 Temporary Binding of Drug Molecules

Drug molecules are involved in three major binding processes: binding to their target, binding to components of the blood, and binding to tissues. In the first case, most drugs act by the inhibition of an enzyme or interaction with a receptor. Out of 480 drugs studied by Saltzman [163], 28% were found to inhibit an enzyme, 45% interacted with general receptors, and 21% interacted with nuclear receptors. The majority of receptors are proteins on or within cells, and the molecules that bind to them are called ligands. The drug-receptor interaction can block or alter the function of the receptor, thereby initiating biochemical and physiological changes. The structure of a drug determines its binding affinity for the receptor.

In addition to the specific binding of drugs to initiate a therapeutic effect, drug molecules can bind in non-specific ways to blood components. Many drugs bind to plasma proteins in a nonlinear, saturable way, although the unbound fraction may be relatively constant around the therapeutic range [32]. The main plasma proteins are albumin, globulins, clotting proteins, hormones, enzymes, and antibodies. Drug molecules can also bind to red blood cells.

Furthermore, drug molecules can bind to the cellular components of tissues. Examples include the binding of quinacrine in the liver and spleen [204] and the binding of gentamicin in the kidney [134]. In addition, fat can serve as a reservoir for lipid-soluble drugs. Due to low blood flow to these sites, drug molecules can remain bound to fat for long periods of time. Bone is another potential reservoir. Drug molecules can adsorb onto the surface of the bone crystal and eventually be incorporated into the lattice [32]. Examples are toxins like lead and the tetracyline antibiotics, and their prolonged release from bone is governed mostly by the rate of bone remodeling [181].

A high binding affinity can be an advantage if it refers to the target of the drug; however, if the target is elsewhere, those tissues act instead as drug reservoirs that prolong

the body's exposure to the drug and can initiate local toxicities and complicate dosage estimates. Because a drug's target is frequently outside of the blood, pharmacokinetic data tend to be an indirect signal from which the crucial information must be deduced.

7.2.2 Lévy Distributions

Lévy distributions are the typical framework for analyzing and modeling power law behaviour in fields as diverse as geology [147][148], economics [171][28], and physics [72][165]. Applications in biology and medicine include the nature of DNA sequences [168], motor-controlled movements in humans [35], the spreading of epidemics [118], animal flights [20], and neural networks [172].

Lévy distributions (also called stable, α-stable, or Lévy stable distributions) allow skewness and heavy tails. They follow the Generalized Central Limit Theorem that states that the only non-trivial limit of a normalized sum of independent, identically-distributed variables follows a Lévy distribution. The standard Central Limit Theorem is a special case in which the limit of normalized sums of independent, identically-distributed terms with finite variance tends to a Gaussian. Let a Lévy random variable be denoted by $S(\alpha, \beta, \sigma, \mu)$, where $\alpha \in (0, 2]$, $\beta \in [-1, 1]$, $\sigma \in \Re_+$, and $\mu \in \Re$ are the indices of stability, skewness, scale, and shift, respectively. When $\beta = 0$, the subfamily $S(\alpha, 0, \sigma, \mu)$ is symmetric about μ. Two special cases exist: the Cauchy distribution when $\alpha = 0$ and $\beta = 0$, and the Gaussian distribution when $\alpha = 2$ and $\beta = 0$, with mean μ and variance $2\sigma^2$.

Consider the set $\{z\}$ of N statistically independent, identically-distributed random variables and their normalized sum

$$Z \equiv \sum_{i=1}^{N} z_i. \tag{7.1}$$

If the distribution of z has a finite variance, the Central Limit Theorem (CLT) states

that

$$\frac{Z - A_N}{B_N} \stackrel{d}{=} S(2, \beta, \sigma, \mu), \tag{7.2}$$

where the equality sign applies to the probability density functions (PDFs) and A_N and B_N are normalization constants. Thus the distribution of $\{Z\}$ tends towards as Gaussian as N goes to infinity. If the assumption of a finite variance is relaxed, the Generalized Central Limit Theorem (GCLT) holds that [186]

$$\frac{Z - A_N}{B_N} \stackrel{d}{=} S(\alpha, \beta, \sigma, \mu). \tag{7.3}$$

The Gaussian and Cauchy distributions are the only two distributions for which a closed form exists for the probability density function (PDF). Consequently, Lévy distributions are represented by the characteristic function $\phi(t)$ (the Fourier transform of the PDF) through

$$E\left[e^{it\phi}\right] = \begin{cases} \exp\left\{-\sigma|t|^{\alpha}\left[1 - i\beta \mathrm{sgn}(t) \tan\frac{\alpha\pi}{2}\right] + i\mu t\right\} & \text{if } \alpha \neq 1 \\ \exp\left\{-\sigma|t|\left[1 + \frac{2i\beta}{\pi}\mathrm{sgn}(t) \ln|t|\right] + i\mu t\right\} & \text{if } \alpha = 1 \end{cases}, \tag{7.4}$$

where $E[x] = \int_{-\infty}^{\infty} xp(x)\,dx$ denotes the expectation value of x.

Sometimes it is useful to use Zolotarev's (M) parametrization [206]

$$E\left[e^{it\phi}\right] = \begin{cases} \exp\left\{-|t|^{\alpha}\left[1 + i\beta \mathrm{sgn}(t)\left(\tan\frac{\alpha\pi}{2}\right)\left(|t|^{1-\alpha} - 1\right)\right]\right\} & \text{if } \alpha \neq 1 \\ \exp\left\{-|t|\left[1 + i\beta \mathrm{sgn}(t)\frac{2}{\pi}\ln|t|\right]\right\} & \text{if } \alpha = 1 \end{cases}. \tag{7.5}$$

Nolan [140] developed a useful modification $S^*(\alpha, \beta, \sigma^*, \mu^*)$ such that

$$X^* \stackrel{d}{=} \alpha^{-1/\alpha}\sigma^*\left(Z - m(\alpha, \beta)\right) + \mu^*, \tag{7.6}$$

where Z has the characteristic function shown in Eq. 7.5. In this parametrization, the distribution is shifted so that μ and σ coincide with the mode and standard deviation

in the Gaussian case. This parametrization is useful for visual comparisons and computations.

The tails of the Gaussian distribution are exponential. The tail of Lévy distributions with $\alpha < 2$, however, are asymptotically equivalent to a power law [141]:

$$P(X > x) \sim \gamma^{\alpha} c_{\alpha} (1 + \beta) x^{-\alpha} \tag{7.7}$$

$$p(x) \sim \alpha \gamma^{\alpha} c_{\alpha} (1 + \beta) x^{-(\alpha+1)}, \tag{7.8}$$

where $c_{\alpha} = \sin\left(\frac{\pi\alpha}{2}\right) \Gamma(\alpha) / \pi$. These distributions are called heavy-tailed because they fall off more slowly than an exponential, and there is a small but finite probability that x takes an extremely large value.

Figure 7.1 show the PDF generated using the S^* parametrization for $\beta = 1$ as implemented in the STABLE program (available at http://academic2.american.edu/ jpnolan/stable/stable.html). The distributions with higher α are more concentrated near the mode at the origin while those with lower α have heavier tails. When $\beta > 1$, the curves are skewed to the left and the right-hand tail becomes heavier. When $\beta < 1$, the opposite is true, and the curve is identical to that for $\beta = b$ but reflected across the y-axis. Figure 7.2 compares the $\alpha = 0.8$ case for different values of β.

As α decreases, more of the probability resides in the tail. For example, given a sample of data from a symmetric distribution, there would be more than 30 times as many values above 3 in the $\alpha = 1.4$ case than in the Gaussian case and over 100 times as many in the $\alpha = 0.8$ case than in the Gaussian case. Moreover, if the same distributions are fully skewed to the left ($\beta = 1$), these factors more than double.

One consequence of heavy tails is that not all moments might exist, where the n^{th} moment is given by $\langle x^n \rangle = \int_{-\infty}^{\infty} x^n f(x) dx$. The value of α can be thought of as the largest moment that exists. Because the first moment is equal to the mean and the second moment is equal to the variance, distributions with $\alpha < 2$ have an infinite variance, and distributions with $\alpha < 1$ also have an infinite mean.

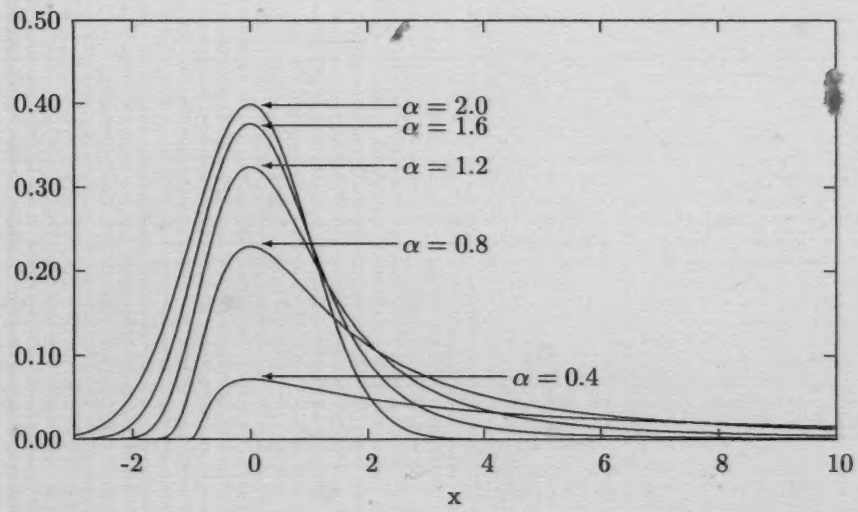

Figure 7.1: Lévy probability density functions for $\beta = 1$, $\sigma = 1$, and $\mu = 0$.

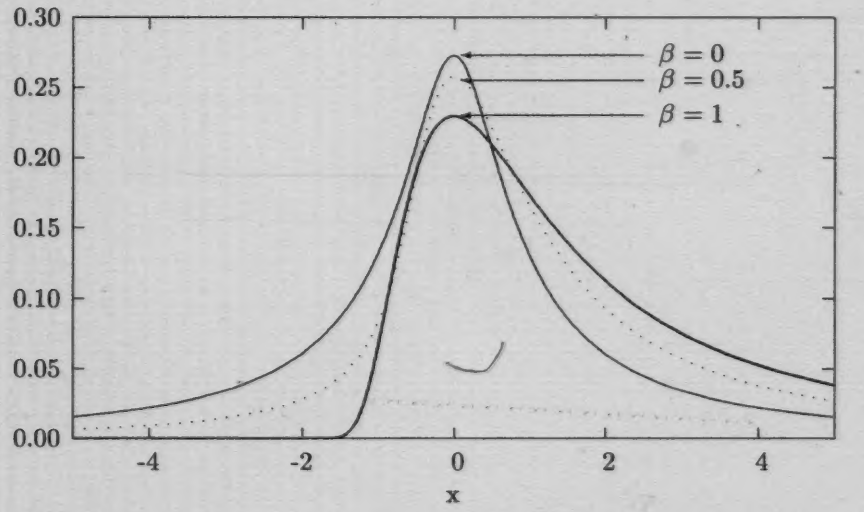

Figure 7.2: Lévy probability density functions for $\alpha = 0.8$, $\sigma = 1$, and $\mu = 0$.

7.2.3 Lévy Flights

A Lévy flight is defined as a stochastic process whose jumps are Lévy-distributed stochastic variables. Lévy flights have been used as a model for trapping times and flight lengths in a variety of physical systems. In their study of subrecoil laser cooling, Bardou et al. [19] describe the transit of an atom as a sequence of trapping periods alternating with diffusive periods. The distribution of trapping times is taken to be Lévy-distributed with index α. The authors found that the evolution of the system depends on competition between the trapping and diffusive processes.

Lévy-distributed trapping times have also been used to characterize incoherent radiation [151]. The radiation undergoes a number of absorption events (due to elastic scattering) and reemission events before ultimately escaping (through inelastic scattering). Single radiation trajectories are described by Lévy flights, and the total trajectory forms a fractal in space.

Lévy flights have also been tied to self-organized criticality (SOC), the spontaneous emergence of scale-invariant behaviour in systems out of equilibrium [18]. Sand or rice piles are the usual paradigm for SOC. Grains are added to the top of a pile, and the transit of the grains to the bottom of the pile is monitored in terms of flight lengths and times. Experiments have shown that the time for grains to escape from the bottom of the pile follows a negative power law distribution [39]. Boguñá and Corral [29] modelled the dynamics by describing the movement of the grains using Lévy flights, which they incorporated into a continuous time random walk model.

Although it might seem illogical to use an infinite-variance distribution to describe a bounded, physical variable, approximations can be made so that the tail distribution exhibits power law behaviour over a large but finite range. Mantegna and Stanley [114] introduced the truncated Lévy flight (TLF), whose PDF for symmetric distributions is

given as

$$p(x) = \begin{cases} 0 & x < -l \\ c_1 L(x) & -l \leq x \leq l \\ 0 & x > l \end{cases}, \tag{7.9}$$

where $L(x)$ is a Lévy distribution with $\alpha \leq 2$, c_1 is a normalization constant, and l is the cutoff length. Mantegna and Stanley found that the sum Z given by Eq. 7.1 with z drawn from Eq. 7.9 converges at a value n_x to a Gaussian for relatively large N or relatively small l. However, if the width of the distribution is small compared to the truncation value, this convergence can be extremely slow. Thus, the sum of a large number of random variables from a distribution with finite variance can follow a non-Gaussian distribution except for at the very ends of its tails. The behaviour of a TLF will be essentially indistinguishable from a Lévy flight, except for in the most rare events. Consequently, although the truncation of the flight renders the moments of the distribution finite, the system can exhibit anomalous behaviour and scaling properties before the eventual convergence.

7.3 Relevance of Lévy Distributions to Pharmacokinetics

Weron [197] has discussed three of the conditions in which Lévy distributions are believed to be applicable in the description of a system: (i) there is a specific theoretical reason for expecting non-Gaussian behaviour (e.g. diffusion in a disordered system); (ii) an observable is the sum of many small terms (e.g. stock market prices); or (iii) a data set exhibits power-law tails. More than one situation might apply to a given system, and indeed in the case of pharmacokinetic systems, each can be found under certain conditions.

In the first case, many drug processes in the body occur in confined or heterogeneous spaces, in which both diffusion and kinetics have been found to exhibit anomalous behaviour [24]. For example, as seen in previous chapters, it has been found that the

pharmacokinetics of a drug eliminated from the liver, an organ with a fractal structure, can lead to fractal kinetics. In the second case, the residence time of a drug molecule can be seen as the sum of many small sojourn times in the cells, tissues, and organs of the body. If the elimination of a drug is slow and/or the drug's binding affinity within the body is high, the number of sojourn times will increase. In the third case, power-law tails have been found empirically in many plasma concentration-time curves. Therefore, as suggested in the literature for radioisotopes, the cycling between trapped and circulating states can describe drug molecules in the body analogous to subrecoil laser cooling, incoherent radiation, and a sandpile. This concept is implemented in the next section using a continuous time random walk model.

7.3.1 Continuous time random walks

In physical systems, random walks in the presence of traps are typically modeled using the continuous-time random walk (CTRW) formalism. Montroll and Weiss [130] introduced the concept to render time continuous without going to the diffusion limit. In a standard random walk, the waiting time between steps is a constant, discrete value. In a CTRW, the time between steps, typically called the waiting time, is drawn from a continuous distribution, $\psi(t)$. The CTRW method has been applied to model systems as diverse as asset prices in the financial market [119], charge transport in amorphous solids [142], and solute transport in geological formations [51].

The relevant master equation is [24]

$$\frac{\partial P(\mathbf{r},t)}{\partial t} = \sum_{\mathbf{r}'} w_{\mathbf{r},\mathbf{r}'} P(\mathbf{r}',t) - \sum_{\mathbf{r}'} w_{\mathbf{r}',\mathbf{r}} P(\mathbf{r},t), \tag{7.10}$$

where $P(\mathbf{r},t)$ is the probability distribution for the walker being at position $\mathbf{r}$ in d - dimensional space at time t, and $w_{\mathbf{r},\mathbf{r}'}$ is the rate of transition from position $\mathbf{r}'$ to position

r. For nearest-neighbour walks on a one-dimensional lattice, the master equation is

$$\frac{\partial P(x,t)}{\partial t} = w_{x,x-1}P(x-1,t) + w_{x,x+1}P(x+1,t) - (w_{x-1,x} + w_{x+1,x})\,P(x,t). \tag{7.11}$$

When all the $w_{x,y}$ values are constant, the walk is classical. If they are also all equal, the simple random walk with no bias is recovered. However, when the transition rates are drawn from a distribution $\psi(w)$, the walk becomes anomalous. These results are useful because many physical problems can be mapped onto the one-dimensional lattice [6]. Disorder or heterogeneity is typically incorporated into CTRW models through a non-Gaussian waiting time distribution $\psi(t)$.

The next section introduces a new application of the CTRW to the modeling of drug residence times. The model builds on the interacting random walk model described in the previous chapter; however, the sojourn time at a lattice site is no longer a constant but rather a random variable drawn from a probability distribution.

7.4 Model

Expanding upon the interacting random walk model developed previously, there are now three different types of lattice sites: plasma (P) sojourn sites, temporary target traps (T), and permanent elimination traps (E). Drug molecules are introduced onto P sites and undergo a sequence of sojourn times in both P and T sites until they are removed from an E site. The total residence time θ of a molecule can now be expressed as

$$\theta = \hat{T} + T\ , \tag{7.12}$$

where T is the total time spent in the plasma and $\hat{T}$ is the total time spent in temporary traps. Because each of these quantities is the sum of N individual plasma sojourn times

Table 7.1: Lévy distribution parameters

Parameter	Description
α	heaviness of the tail
β	skewness
σ	scale
μ	position

τ_j or M individual trapping times $\hat{\tau}_i$,

$$\theta = \sum_{i=1}^{N} \tau_j + \sum_{j=1}^{M} \hat{\tau}_i. \tag{7.13}$$

Note that θ is a macroscopic quantity while τ and $\hat{\tau}$ are microscopic quantities.

In order to focus on the roles of the temporary and permanent trapping sites, the sojourn time in the plasma, $P(\tau)$, is still approximated as a delta function at the value PT. However, it is proposed that the temporary trapping events are Lévy flights, and $P(\hat{\tau})$ is Lévy-distributed . The additional model parameters are listed in Table 7.1. If $\alpha < 2$, there is a dispersion in the trapping times due to the relaxation of deep traps. In this simplified version of the model, the temporary traps are also assumed to be the therapeutic target of the drug (for example, tumor cells in the case of anticancer agents).

Weiss [196] incorporated a similar idea into his recirculatory model for the drug amiodarone. He used a gamma distribution for plasma cycling times in the plasma and trapping times following:

$$f(t) \sim \tau^{\alpha} t^{(-1-\alpha)} \qquad (0 < \alpha < 1). \tag{7.14}$$

His model, however, assumed a constant elimination rate, no interactions between molecules, and no saturable processes.

In the current model, the different methods for eliminating a molecule from an E site are those described in the previous chapter: simple elimination, Michaelis-Menten sat-

Table 7.2: Power law tail exponent between $x = 0$ and $x = 3000$ for the distribution of values drawn randomly from the quantiles for $\alpha = 1.4$.

Number of Values	Power Law Exponent	R^2
10 000	-2.42 (0.15)	0.943
100 000	-2.40 (0.06)	0.983
1 000 000	-2.44 (0.04)	0.992
10 000 000	-2.45 (0.04)	0.992

urable elimination, and fractal elimination under both transient and saturable regimes. To the best of our knowledge, this model is the only one that combines saturable processes, long-term interactions between molecules, and the probability of long-time trapping in the body.

7.5 Method

In order to generate random variables from a Lévy distribution, the characteristic function given by Eq.(7.4) was integrated using techniques outlined by Nolan [140]. In addition, in order to efficiently sample the distribution, look-up tables were generated that consisted of 10,000 quantiles (values separated by equal probability). The quantiles were calculated using

$$\int_{x_i}^{x_{i+1}} f(x)dx = p, \tag{7.15}$$

with $p = 1 \times 10^{-7}$. Therefore, two integrations were performed. To get a power-law relationship, the quantiles were drawn from the end portion of the Lévy distribution, with $\beta = 0$, $\mu = 0$, and $\sigma = 1$. All the values were shifted such that $x_1 \equiv 0$. The power law exponent of each PDF was equal to $-(1+\alpha)$ to within 1×10^{-6}. The quantiles were tested by uniformly sampling the quantiles randomly and checking the distribution of the new values. The results for the quantiles for $\alpha = 1.4$ are shown in Table 7.2.

Unless otherwise indicated, the model parameters were chosen to be $L = 200,000$ lattice sites, $N = 10,000$ drug molecules, $PT = 3$ time steps spent at a P site, $ET = 3$

Table 7.3: Power exponent γ for drug molecules undergoing simple elimination and Lévy trapping with different values of α.

α	Time Range	γ	R^2
1.2	$50 - 5000$	-1.187 (0.003)	0.992
1.4	$50 - 2000$	-1.241 (0.005)	0.990
1.6	$50 - 1000$	-1.255 (0.006)	0.983
1.8	$50 - 400$	-1.316 (0.008)	0.994

time steps spent at an E site, and $\sigma = 10$ for the Lévy distributions. Because the goal is to investigate the interplay between the temporary and permanent trapping processes, the values for $f_T = 0.05$ and $f_E = 0.05$ were chosen since they were much smaller than f_P but equal to each other.

7.6 Results

7.6.1 Effect of Lévy-distributed Traps

Figure 7.3 shows the plasma occupation curve following a bolus dose of drug molecules undergoing simple elimination and Lévy-distributed trapping times with $\alpha = 1.6$. After an initial period, the tail of the curve transitioned to a power law at $t = 30$ and persisted until $t = 1000$. There was a short terminal exponential decay that occurred when less than 1% of the molecules remained in the system. The power exponent of the tail was $\gamma = -1.255 \pm 0.006$ ($R^2 = 0.993$). Therefore, temporary traps with power-law-tailed trapping times can produce a concentration-time curve with power law behaviour that persists over three orders of magnitude, even when the elimination process is linear and the probability of trapping is only 5%.

The effect of decreasing α was to decrease γ but increase the range over which the power law persisted (Table 7.3). In each case, $\gamma < \alpha$, but the percent difference decreased with decreasing α. The shape of the power law segment was relatively independent of the scale factor σ (Table 7.4).

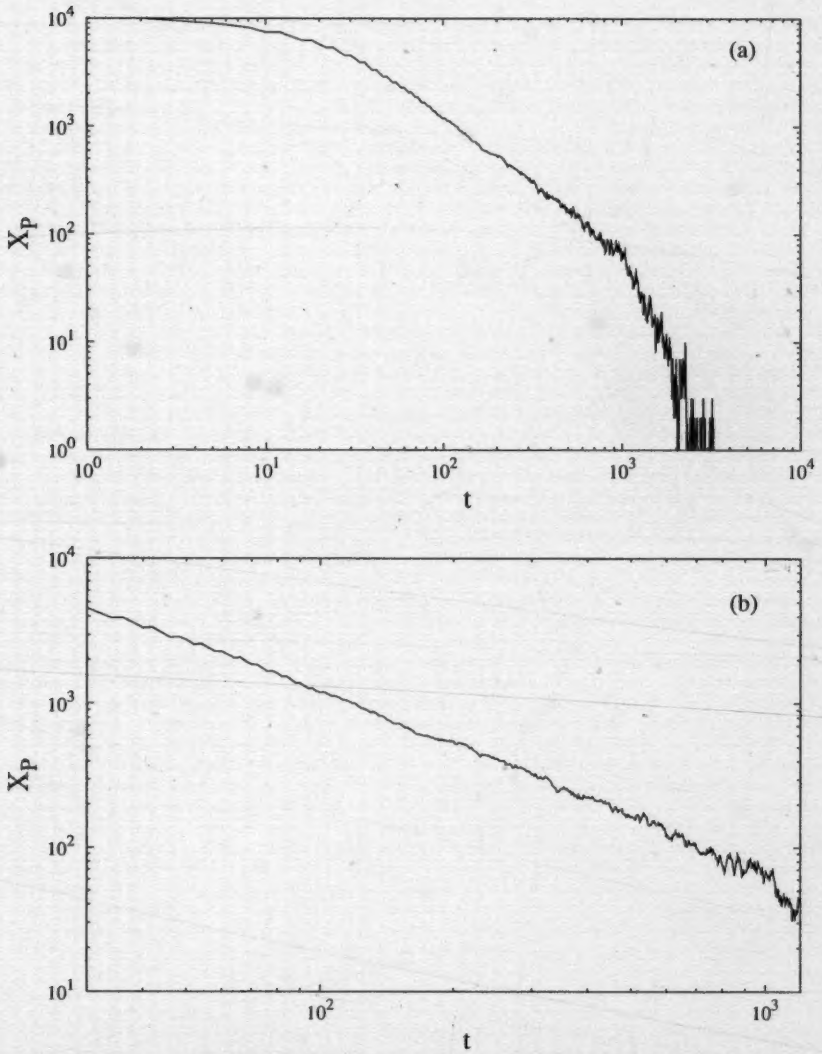

Figure 7.3: (a) The plasma occupation as a function of time for $N = 10,000$ molecules undergoing simple elimination and Lévy-distributed trapping with $\alpha = 1.6$. (b) Closeup of the the power law segment between $t = 30$ and $t = 1000$.

Table 7.4: The power exponent for $\alpha = 1.6$ as a function of the Lévy scale, σ.

σ	γ
1	1.271 (0.008)
5	1.253 (0.008)
10	1.255 (0.006)
15	1.210 (0.004)
20	1.294 (0.007)

Table 7.5: The mean power exponent γ and standard deviation as a function of the number of values.

No. Values	γ
5	1.259 (0.011)
10	1.255 (0.006)
20	1.259 (0.005)
30	1.255 (0.004)
40	1.256 (0.004)

7.6.2 Sensitivity of the Power Exponent

Sensitivity analysis was performed for γ. In order to determine the minimum number of runs required to achieve an acceptable error value, the simulation illustrated in Fig. 7.3 was executed for 10 different values of the random seed. Since the improvement in the error was not significant beyond 10 runs (Table 7.5), this value was chosen for all subsequent simulations in order to minimize run times. The same simulation was also repeated for three different lattice sizes L. The mean values of γ agree within error, but the standard deviation decreases with increasing lattice size (Table 7.6). Therefore, the maximum sized lattice ($L = 200,000$) that can be accommodated by the computer was chosen for all subsequent runs.

Table 7.6: The mean power exponent γ and standard deviation as a function of the lattice size, L.

L	γ
50,000	1.212 (0.012)
100,000	1.231 (0.087)
200,000	1.255 (0.006)

Table 7.7: Power law exponent for Lévy trapping with $\alpha = 1.6$ with simple elimination, for different relative strengths of the temporary and permanent trapping.

f_E/f_T	Time Range	γ	R^2
0.1	100 – 1000	-0.399 (0.006)	0.983
0.4	100 – 1000	-0.629 (0.006)	0.993
0.6	100 – 1000	-1.13 (0.01)	0.989
1.0	30 – 1000	-1.255 (0.006)	0.993
1.4	30 – 900	-1.334 (0.006)	0.992
1.6	30 – 900	-1.379 (0.009)	0.983
2.0	30 – 900	-1.41 (0.01)	0.987

7.6.3 Temporary Versus Permanent Trapping

As the number of E sites was decreased, the power exponent decreased (Fig. 7.4) but the length of the power law portion remained almost the same (Table 7.7). Therefore, the effect of a decreased elimination probability was to decrease γ.

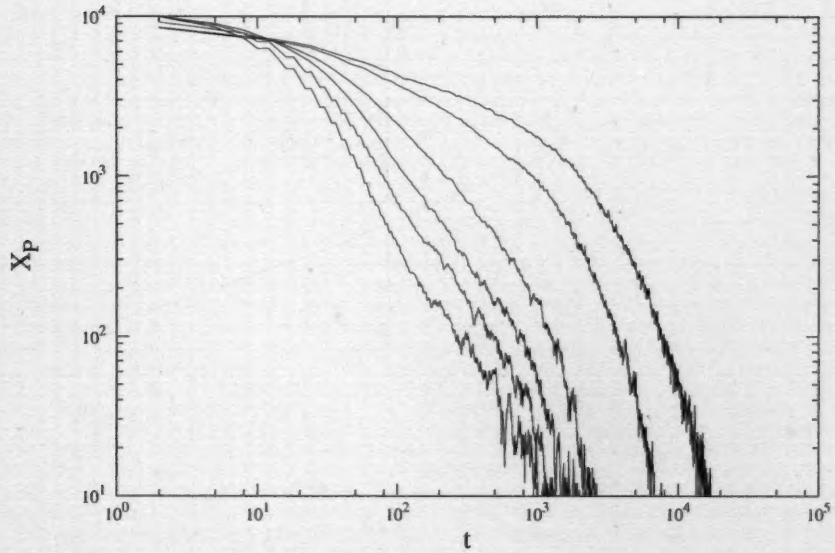

Figure 7.4: The plasma occupation for $N = 10,000$ molecules undergoing simple elimination and Lévy-distributed trapping. From top to bottom, $f_E/f_T = 0.1, 0.2, 0.6, 1.0, 1.4, 2.0$.

7.6.4 Effect of the Elimination Kinetics

In the above sections, it was demonstrated that a small probability of a Lévy-distributed trapping event could produce plasma occupation curves with a significant power law segment. This section investigates how this behaviour is affected when the elimination process is not linear. Figures 7.5 – 7.7 show the results when the elimination is saturable, fractal, and saturable fractal, respectively.

In the saturable case, the power law segment became longer and steeper as the maximum number $N_E^{\max}$ of molecules allowed in E sites increased.

When the elimination occurred via transient fractal kinetics through the use of clustering effects, decreasing Ω decreased the value of γ. The stronger the clustering effects, the less prominent the power law, and at $\Omega = 1$, the power law disappeared. Therefore, the clustering reduces the effect of the long-time trapping mechanism, since less molecules will attempt to move at a given time. As Ω decreased, the clustering effects became more dominant and the elimination depended more on the release of the molecules from the clusters than on the release from the temporary traps. The transition occurs when the time to be released from a cluster is longer than the time to be released from a trap.

In the case of elimination with both saturation and clustering effects, the power law segment becomes less steep and it persists for longer.

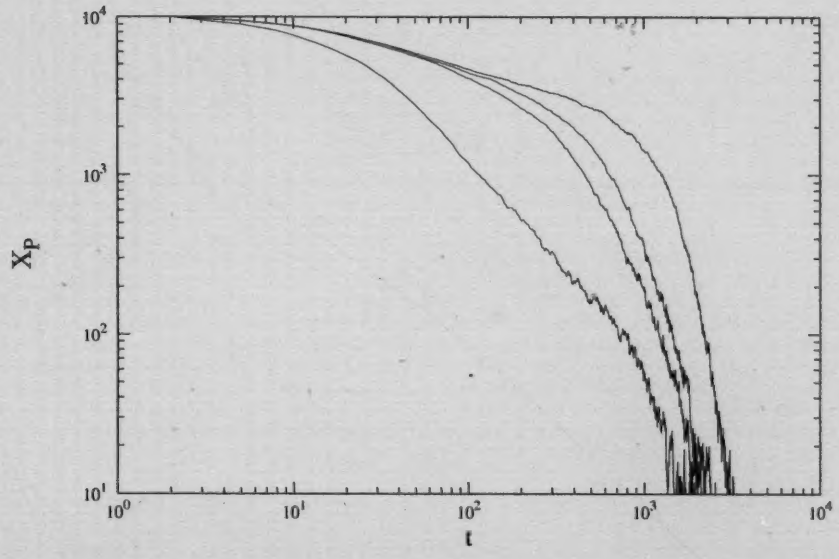

Figure 7.5: The plasma occupation for $N = 10,000$ molecules undergoing saturable elimination and Lévy-distributed trapping. From top to bottom, $N_E^{\max} = 15, 30, 45, 10,000$.

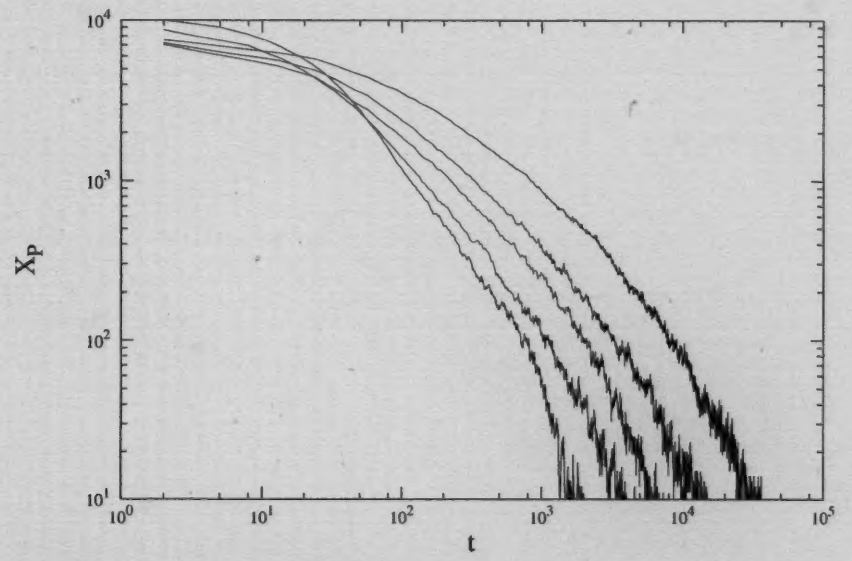

Figure 7.6: The plasma occupation for $N = 10,000$ molecules undergoing fractal elimination and Lévy-distributed trapping. From left to right, $\Omega = 100, 5, 3, 2, 1$.

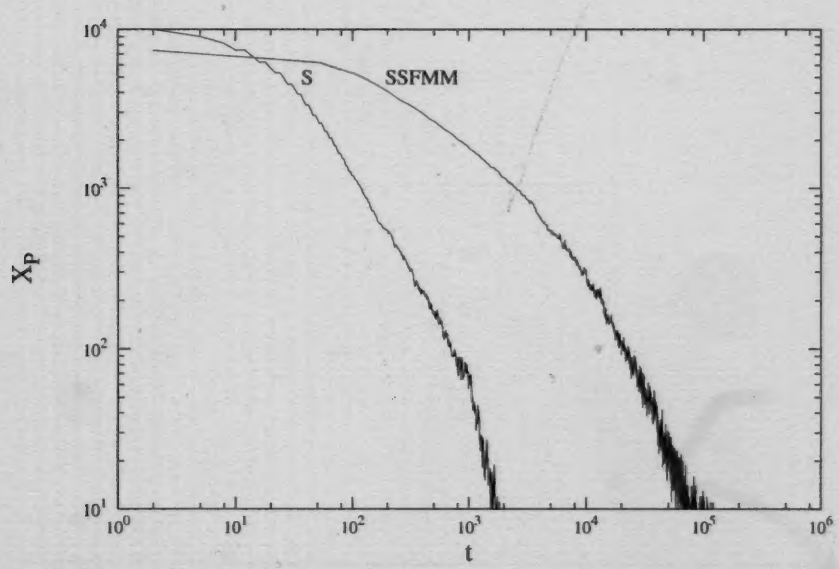

Figure 7.7: The plasma occupation for $N = 10,000$ molecules undergoing Lévy-distributed trapping and simple (S) elimination or steady steady fractal (SSFMM) elimination ($N_E^{\max} = 15$).

7.6.5 Predicting the Dose to the Target

If the temporary traps are the drug's intended target, one important use of this type of modeling is the extrapolation of the T site occupation level from the observable signal, the P site occupation level. Table 7.8 shows that the highest occupation level at the target site is achieved when the elimination kinetics are fractal, while the greatest dose to the target occurs for fractal Michaelis-Menten elimination kinetics. A saturable elimination process allows more drug molecules to enter long-time traps. Figure 7.8 illustrates the three processes. Although the highest occupation level is reached with fractal kinetics, the occupation drops off quickly. However, with the saturable elimination, the target occupation level remains higher over a much longer period.

Figure 7.9 shows an example of a quantitative relationship between the observed plasma signal and the occupation number of the target. Note that the shape of the curve is strongly dependent on the type of elimination kinetics. If one can deduce the type of elimination kinetics that might be present in a system based on the shape of the plasma concentration-time curve, this type of graph can then be used to estimate the relationship between the plasma occupation and the amount of drug at the target site. In addition, the curve indicates at what plasma occupation the maximum target dose can be expected. This occupation number is much lower in the case of simple elimination and much higher for the other elimination regimes. Interestingly, the maximum target occupation under fractal Michaelis-Menten elimination is sustained over a range of plasma occupation of almost 2000.

Table 7.8: Pharmacokinetic parameters.

Elimination Kinetics	AUC_P $(\times 10^6)$	AUC_T $(\times 10^6)$	X_T^{max} $(\times 10^3)$
Linear	0.597 (0.006)	1.41 (0.03)	3.03 (0.02)
Fractal	3.92 (0.02)	7.24 (0.03)	5.12 (0.04)
Michaelis-Menten	13.6 (0.6)	28.5 (0.04)	2.67 (0.02)
Fractal Michaelis-Menten	15.7 (0.1)	31.7 (0.03)	3.44 (0.04)

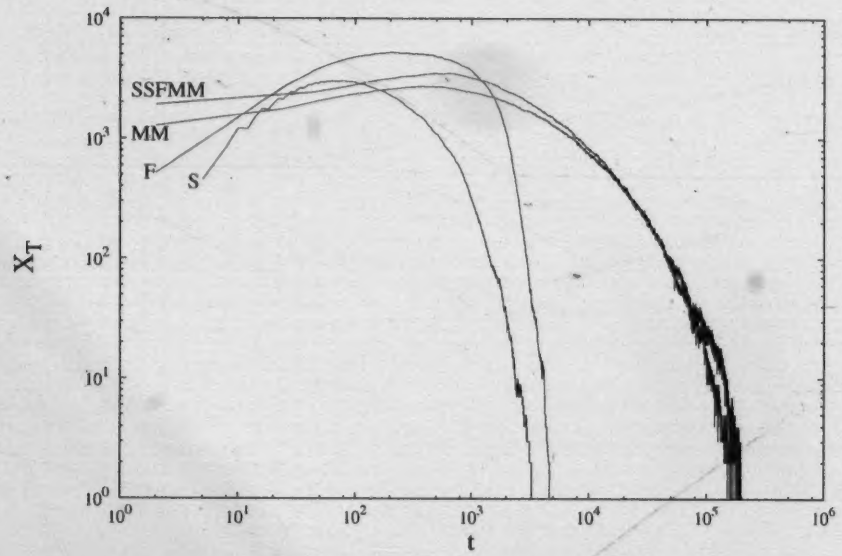

Figure 7.8: The target occupation as a function of time for $N = 10,000$ molecules undergoing Lévy-distributed trapping with $\alpha = 1.6$ and fractal Michaelis-Menten (SSFMM), Michaelis-Menten (MM), fractal (F), or simple (S) elimination.

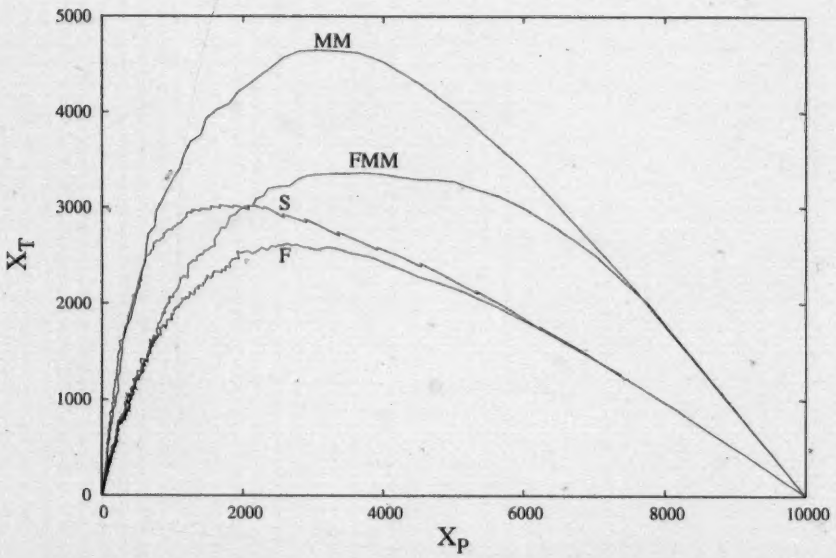

Figure 7.9: The target occupation as a function of the plasma occupation for $N = 10,000$ molecules undergoing Lévy-distributed trapping with $\alpha = 1.6$ and Michaelis-Menten (MM), fractal Michaelis-Menten (SSFMM), simple (S), or fractal (F) elimination.

7.6.6 Infusion curves

When the molecules were administered via an extended infusion instead of a bolus dose, AUC_P and AUC_T were only independent of the infusion rate for the case of linear elimination (Fig. 7.10). For very small infusion rates, or very long infusion times, the fractal and linear cases gave the same dose to the plasma and the target. In addition, the behaviour in these two cases was the same. However, in the case of Michaelis-Menten and fractal Michaelis-Menten elimination kinetics, there was a rise in both AUC_P and AUC_T at small infusion rates. This is because the elimination sites do not saturate.

Figure 7.11 shows the behaviour of $X^{\max}$ as the infusion rate increases. In the case of linear elimination, $X_P^{\max}$ increases linearly with the infusion rate, but $X_T^{\max}$ increases at a much faster rate. For the cases of fractal, Michaelis-Menten, and fractal Michaelis-Menten elimination kinetics, it appears that $X_T^{\max}$ reaches a maximum more quickly than $X_P^{\max}$.

Finally, the relationship between the target occupation and the plasma occupation was investigated for different infusion rates. The curves are more skewed towards the X_T axis in the case of fractal Michaelis-Menten elimination, and they also decrease in size much more slowly.

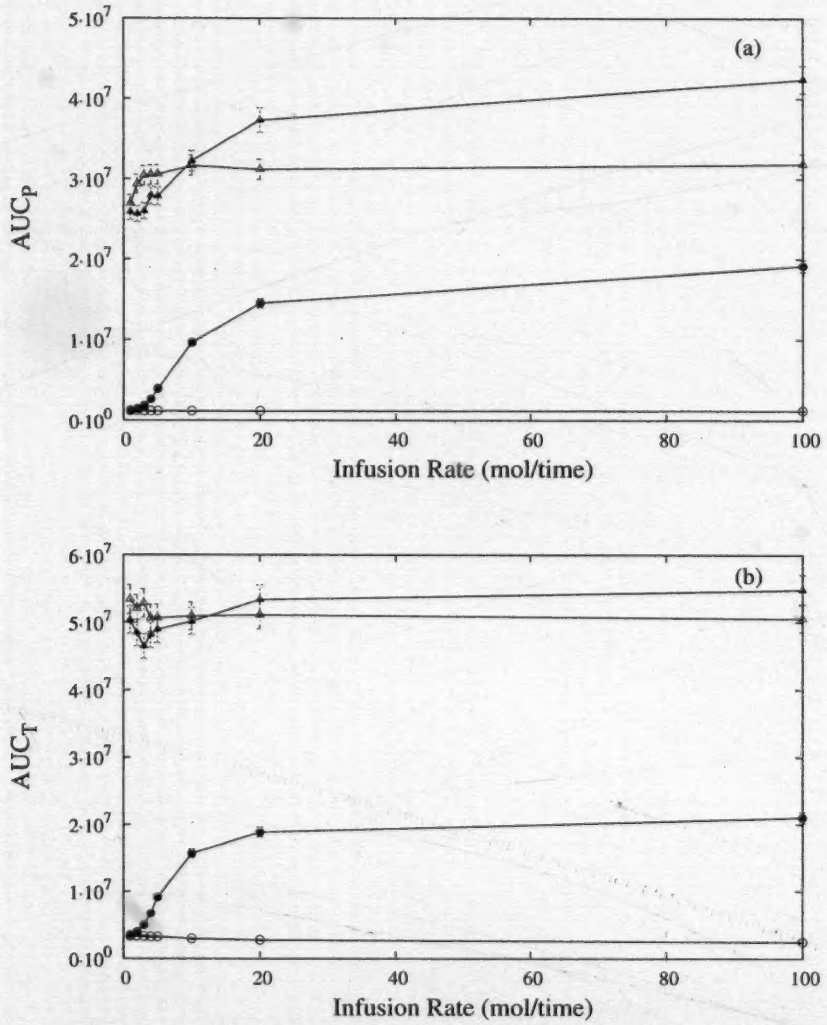

Figure 7.10: Area under (a) the plasma occupation curve and (b) the target occupation curve for Lévy-distributed traps with elimination following linear (open circles), fractal (solid circles), Michaelis-Menten (open triangles), and fractal Michaelis-Menten (solid triangles) kinetics.

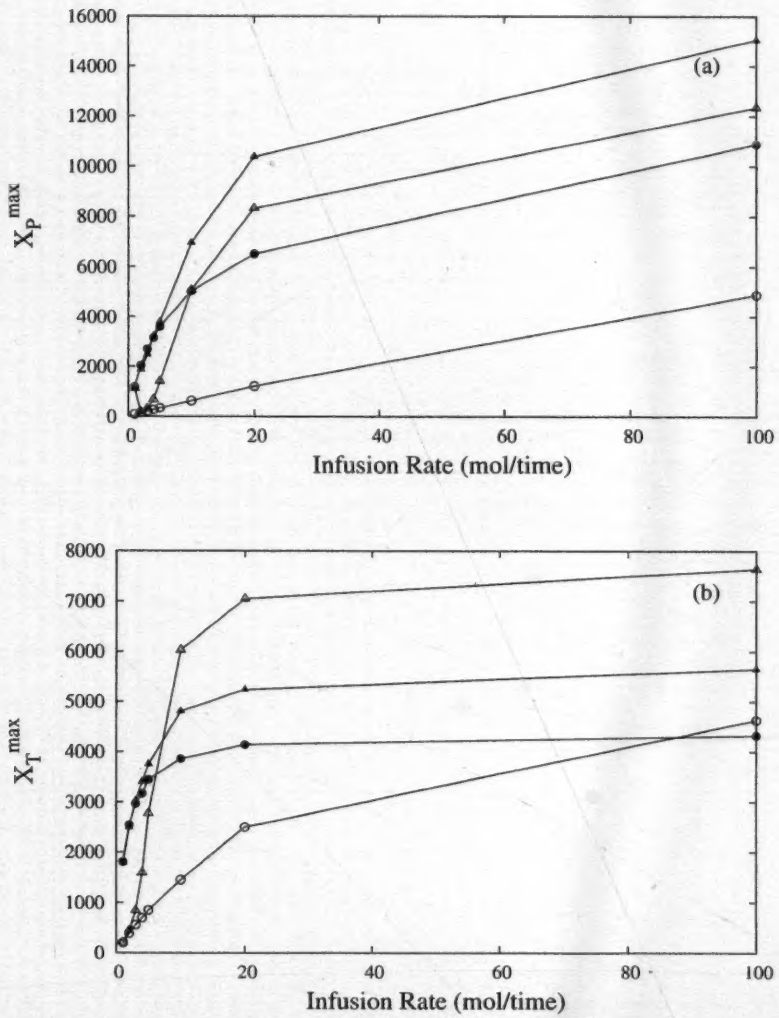

Figure 7.11: Maximum (a) plasma and (b) target occupation number for Lévy-distributed traps with elimination following linear (open circles), fractal (solid circles), Michaelis-Menten (open triangles), and fractal Michaelis-Menten (solid triangles) kinetics.

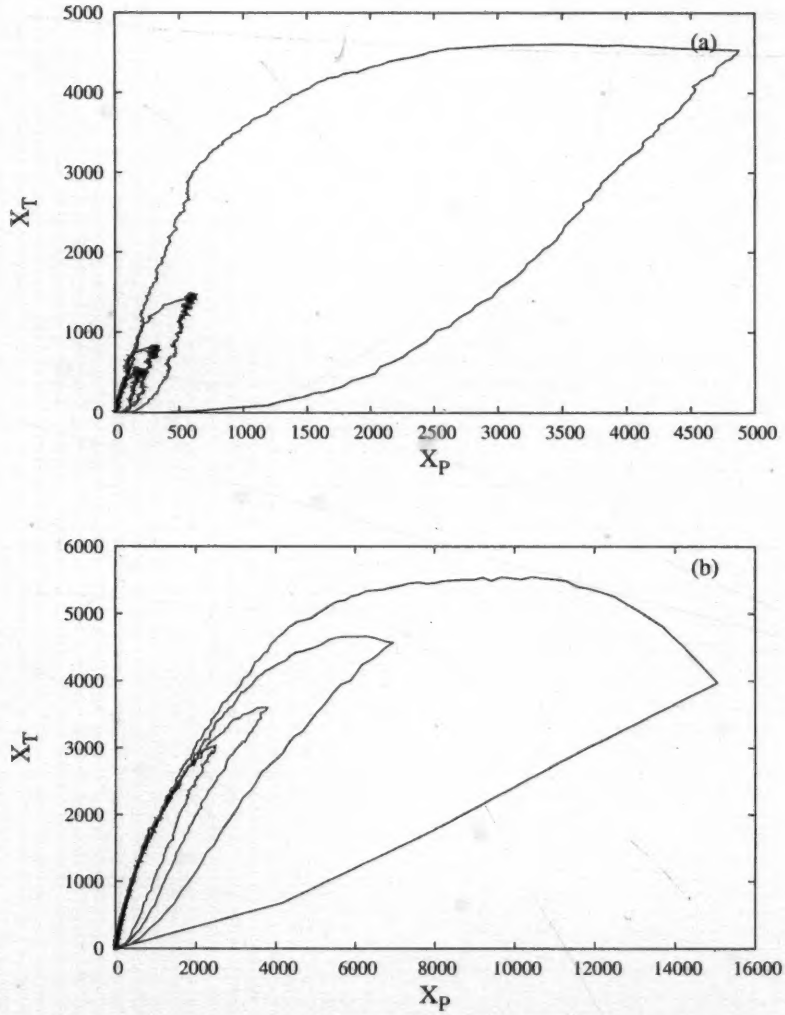

Figure 7.12: The target occupation number as a function of the plasma occupation number for Lévy traps and (a) linear or (b) fractal Michaelis-Menten elimination. The curves represent an infusion rate of, from inside to outside, 100, 10, 5, and 1 molecules per time step.

7.7 Discussion

The pharmacokinetic time series can be seen as a fractal time process in which the events that make up the process are distributed in a self-similar way. This means that the events occur as a hierarchy of bursts separated by a hierarchy of gaps. This is an example of statistical self-similarity, where the PDF of the residence time measured on a large scale is similar to the PDF of the residence time measured on a small scale. One consequence of the self-similarity is that there may be no single mean residence time. The analysis can be taken one step further to relate the parameter γ to the self-similarity of the drug residence times. Differentiating the equation $C(t) \propto t^{\gamma}$ gives

$$\frac{dC}{dt} \sim \gamma t^{\gamma-1} \tag{7.16}$$

and therefore

$$\frac{dC/C}{dt/t} \sim \gamma. \tag{7.17}$$

This, the relative variation of C divided by the relative variation of t is constant [108]. Therefore, γ relates how many molecules are being eliminated by a fractal Michaelis-Menten mechanism that is similar to the overall process governing the residence time distribution.

While allometric scaling has been applied to pharmacokinetics, the scaling of pharmacokinetic processes occurring within an individual has yet to be investigated. One advantage of scaling properties is that knowledge of the appearance or behaviour of a system at one scale (such as the whole body) provides information about the system at other scales (such as the organ or cellular level). Therefore, scaling laws can help extrapolate knowledge about elements of a system that are difficult to directly measure (such as the drug concentration in a tumour or in individual tumour cells).

7.8 Conclusion

The concept of Lévy flights has many potential applications in pharmacokinetic modeling. Expanding the random walk model from the previous chapter into a CTRW with Lévy trapping times enabled the construction of the first stochastic pharmacokinetic model that combines the effects of saturable and fractal permanent elimination with long-time temporary trapping. The model can be used to extrapolate the target dose from the plasma signal and to predict changes in the system's response to different dosing regimes.

An advantage of this model is that it does not make any assumptions about what causes the dispersion in the molecular residence times; these causes could include fractal kinetics, mechanisms of cell death, heterogeneity in cell populations, or release from long-time traps in cells such as tumour or fat cells. Furthermore, this dispersion can also help explain some clinical observations, for example delayed reactions in certain patients.

Chapter 8

Physiologically-Based Flow Network Model for Drug Elimination

8.1 Purpose

The objective of this chapter is to investigate whether the aggregate, organ-level kinetics modeled by a fractal compartment can be reproduced at the level of a single functional unit of the organ. A discrete network model is developed using anatomical and physiological parameters of the liver, and the effects of different types of heterogeneity are explored.

8.2 Background

8.2.1 Liver Architecture

At the macroscopic level, the liver consists of three vascular trees, two supply trees that originate from the portal artery and hepatic vein, and one collecting tree that drains into the portal vein [15] (Fig. 8.1 (a)). The vessels bifurcate down to the terminal arterioles

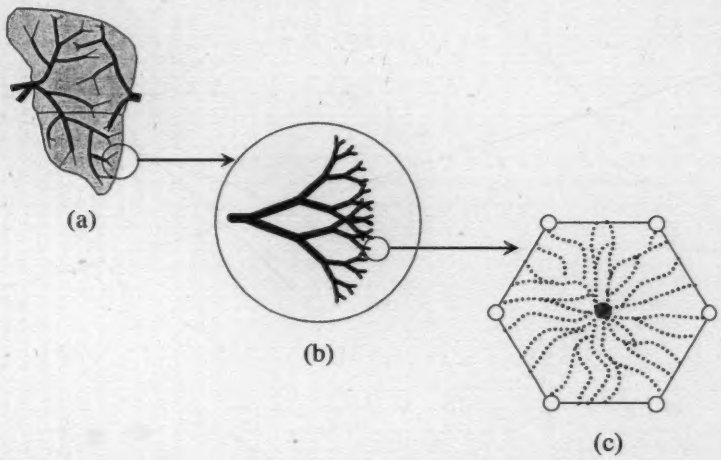

Figure 8.1: The liver. (a) The macrostructure. The hepatic artery and portal vein bring blood rich in oxygen, nutrients, and drug molecules in from the left. (b) The vessels branch to form a tree of arterioles and venules. (c) Pairs (represented by open circles) of terminal hepatic arterioles and portal venules empty into a hexagonal lobule. The blood flows towards a central hepatic venule (solid circle) The dotted lines represent sheets of hepatocyte, and the white space between them represents the sinusoids.

and venules (Fig. 8.1 (b)), which are organized into portal tracts along with a terminal bile duct. Liver cells, called hepatocytes, radiate outward from the terminal vessels. These plates of hepatocytes are interspersed by sinusoids, which play the role of the capillary in the liver, and the spaces of Disse, which are the extravascular space of the liver [67]. Finally, the blood is collected and removed by the hepatic venules.

8.2.2 Functional Unit

The functional unit of an organ is the smallest structural unit that can independently serve all of the organ's functions [167]. Because of its complexity, there is continued debate about what the functional unit of the liver should be. The classic lobule (Fig. 8.1 (c)) is a hexagonal cylinder, centered around a hepatic venule and with portal tracts situated at the corners. The portal lobule has a similar shape but is centered about a portal tract with the hepatic venules at the periphery [27]. The acinus is another proposed unit and is based on the pattern formed by the cords of hepatocytes between two central venules.

Table 8.1: Anatomical values for the liver.

Parameter	Value	Ref.
Hepatocyte diameter	12–24 μm	[70]
Diameter of liver cell sheets	25 μm	[67]
Lobule diameter	1–2.5 mm	[70]
Mean sinusoid diameter	7.3 μm	[67]
	$9.0 \pm 0.2\mu$m	[3]
Vascular tissue component	28–30%	[73]
Specific gravity of liver	1.05	[70]
Liver volume	1071 ± 228 cm^3	[205]

Matsumoto and Kawakami [123] suggested that the classic lobule can be divided into primary lobules, which are cone-shaped and each fed by one portal tract and drained by one hepatic venule. Teutsch and colleagues [183, 182] performed a morphological study of rat and human liver lobules, and their results support the idea of a secondary unit made up of primary units in what they term as a modular architecture. They conclude, however, that the primary unit is more polyhedral in shape than conical. Other experiments done by Ruijter et al. [162] suggest that the primary unit is needle-shaped and that there are equal amounts of portal and central vein associated with one unit. For this study, the primary unit is taken to be one-fourth of the classical lobule. The relevant anatomical values are listed in Table 8.1.

8.2.3 Diseased states

The health of the liver can be compromised by viruses, hereditary diseases, and toxins such as alcohol [184]. Damage or death of the hepatocytes leads to inflammation of the liver, called hepatitis. Although zones of necrosis can form when adjacent cells die, this damage is to some extent reversible, since the liver has the ability to regenerate. Thus hepatitis is typically characterized by waves of cell death and regeneration, leading to a mixture of necrotic areas and nodules of new hepatocytes. Because the architecture of the liver is often compromised, some cells may not receive normal levels of blood

supply. Furthermore, as inflammation progresses, fibrous tissue may replace the normal hepatocytes, resulting in the irreversible condition of cirrhosis. The damage can be compounded because the formation of necrotic zones increases the resistance to blood flow, and intrahepatic shunts can occur in which blood vessels begin to bypass the liver altogether. Therefore, although the liver has the capacity to withstand and even correct a lot of damage, its ability to transport, absorb, and metabolize important nutrients and drug molecules can be compromised.

8.2.4 Network Models of the Liver

Several lattice models have been used to simulate enzyme kinetics in disordered media. Berry [25] performed Monte Carlo simulations of a Michaelis-Menten reaction on a two-dimensional lattice with a varying density of obstacles to simulate the barriers to diffusion caused by biological membranes. He found that fractal kinetics resulted at high obstacle concentrations. Kosmidis et al. [96] performed Monte Carlo simulations of a Michaelis-Menten enzymatic reaction on a two-dimensional percolation lattice at criticality. They found that fractal kinetics emerged at large times.

Previously, Chelminiuk et al. [37] developed a network model of the liver consisting of a square lattice of vascular bonds connecting two types of sites that represent either sinusoids or hepatocytes. Random walkers explored the lattice at a constant velocity and were removed with a given probability from hepatocyte sites. To simulate different pathological states of the liver, random sinusoid or hepatocyte sites were removed. For a lattice with regular geometry, it was found that the number of walkers decayed according to an exponential relationship. For a percolation lattice with a fraction p of the bonds removed, the decay was found to be exponential for high trap concentrations but transitioned to a stretched exponential at low trap concentrations.

The models described above are all basic random walk models, and the lattices are abstract representations of the geometry of the space. The objective of this chapter is to develop a lattice model that incorporates realistic anatomical and physiological

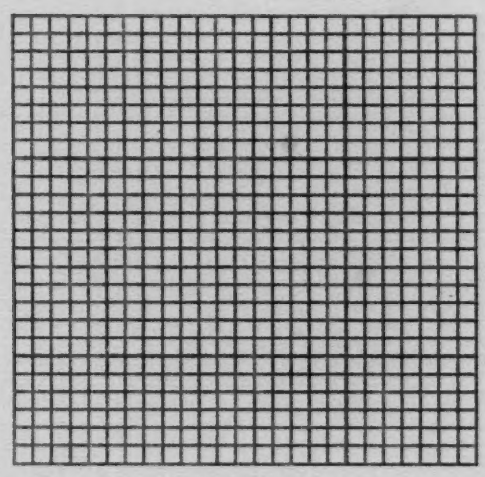

Figure 8.2: Homogeneous lattice. The grey bands represent sinusoids and the white spaces represent hepatocytes.

properties of the liver as well as the transport of reacting tracers by a blood-like fluid.

8.3 Model and Methods

The primary unit of the liver was approximated by a 51×51 square lattice such that four units correspond to one lobule. The architecture of the lattice consists of hepatocyte grid cells interlaced by a network of narrower sinusoidal grid cells (Fig. 8.2). The diameter of the sinusoid grid cells was taken to be 0.0006 cm, and the diameter of the hepatocyte grid cells was taken to be 0.0024 cm. The length of the lattice was thus 0.0744 cm per side. Doubling this value gives a lobule diameter of 0.149 cm, which is consistent with values listed in Table 8.1. The depth of the lattice was taken to be the diameter of a sinusoid, 0.0006 cm.

Each sinusoid grid cell represents a tubular vessel of diameter a. Taking the ratio of the volume of the vessel to the volume of the grid cell yields a porosity of $\phi_S = 0.7854$. Each parenchymal grid cell represents a cellular (hepatocyte) component and an extracellular (space of Disse) component. A ratio of 0.75 to 0.25 was chosen for their

$$\text{PAC} + \text{CYP} \longrightarrow \text{PAC-OH} + \text{CYP}$$

Figure 8.3: Simplified scheme of the Phase I metabolism of paclitaxel (PAC) by the enzyme cytochrome (CYP) P450 3A4 to form the metabolite hydroxy-paclitaxel (PAC-OH).

respective contributions to the volume, and the porosity of the parenchymal sites was therefore $\phi_H = 0.25$.

There is an input site corresponding to a terminal portal venule at one corner of the lattice and an output site corresponding to a terminal hepatic venule at the opposite corner. For simplicity, the arterial blood supply, which is lower in volume and pulsatile in nature, is omitted for the current simulations. The blood viscosity was taken to be 3.5. The molecular weight of the hepatocytes was taken to be 131, based on the formula $C_5H_9O_3N$, which is a standard representation of cell systems [124]. The drug paclitaxel was used as a reactive tracer, and its Phase I metabolism was modeled using the general formula of one paclitaxel (PAC) molecule being transformed into the metabolite 6α - hydroxypaclitaxel (PAC-OH) by the cytochrome P450 (CYP) isozyme CYP2C8 [129] (Fig. 8.3). Each hepatocyte grid cell contains a molar fraction of enzyme. The reaction can proceed in a linear manner at a rate characterized by k (in units of min^{-1}) or via Michaelis-Menten kinetics, defined by K_M (in units of molar fraction) and $v_{\max}$ (in units of min^{-1}). The molecular weight of paclitaxel is 0.853906.

In order to investigate the effects of the heterogeneity of the liver architecture on the rate of the reaction, three different variations of the lattice were studied: a regular lattice, a lattice with random permeability of the sinusoids, and a percolation lattice with a random number of the sinusoid sites removed.

The simulations were performed using the STARS advanced process simulator designed by the Computer Modelling Group (CMG) Ltd. in Calgary, Alberta, to model the flow and reactions of multi-phase, multi-component fluids through porous media. The medium is discretized into grid cells, and the displacement of fluid between cells is

calculated based on mass and energy conservation and the difference in pressure [104]. This difference can be induced by chemical, mechanical, or thermal processes. In the current simulations, the fluid flow was driven by a higher pressure at the inlet than at the outlet. STARS uses an adaptive-implicit numerical scheme such that the properties of each grid cell can be solved in either an implicit or an explicit mode [161]. This technique combines the stability of the implicit method while retaining the computational efficiency of the explicit method. Matrix inversion is achieved using CMG's package AIMSOL, based on incomplete Gaussian Elimination [104], and its extension, PARASOL, to parallel computing architectures [48]. Although the program can model both convective and dispersive effects, only convective transport was studied here.

Ignoring the dispersive contribution and making the assumption of incompressible and laminar flow, the system progressing according to Darcy's Law:

$$Q = -\frac{\kappa}{\mu}\frac{\partial P}{\partial x}, \tag{8.1}$$

where Q is the fluid velocity, κ is the permeability, μ is the viscosity of the fluid, and $\frac{\partial P}{\partial x}$ is the pressure gradient. The permeability κ is a measure of the transmissibility of a grid cell to the flow of a fluid, expressed in units of area (e.g. cm^2). For a cylindrical tube such as a blood vessel,

$$\kappa = \frac{r^2}{8}, \tag{8.2}$$

where r is the radius of the tube. For multi-component flow, STARS tracks the composition (molar or mass fraction) of any components in the fluid. The molar fraction χ was used here.

The pressure value at the inlet was taken to be $P_{in} = 103\,\mathrm{kPa}$, and the pressure at the outlet was taken to be $P_{out} = 101.8\,\mathrm{kPa}$. After subtracting the atmospheric pressure, these values are consistent with experimental values quoted by Rappaport [155], who found that the terminal portal venule pressure was $0.59 - 2.45$ kPa and that the terminal hepatic venule pressure was 0.49 kPa. Because flow through the lobule is due to the

pressure drop across the lattice, the generated flow rate will be a measure of the flow permeability of the lobule and hence a reflection of the health and functioning of the liver.

8.4 Results

8.4.1 Regular Lattice

When blood with a relative composition of 0.01 paclitaxel was infused into the regular lattice shown in Fig. 8.2 with nonreactive hepatocytes, the evolution of the paclitaxel concentration on the lattice followed a spatially homogeneous progression (Fig. 8.4). The flow rate at the input was 6.8×10^{-5} cm^3/min.

When a linear reaction (with $k = 10,000$ min^{-1}) was allowed to occur within the hepatocytes, a plot of the molar outflow of the metabolite followed a linear increase in the transient regime before transitioning to a steady state (Fig. 8.5). When the reaction proceeded instead by Michaelis-Menten kinetics (with $K_M = 2 \times 10^{-8}$ molar fraction and $v_{\max} = 10,000$ min^{-1}), the Lineweaver-Burke plot was linear in the transient regime (Fig. 8.6).

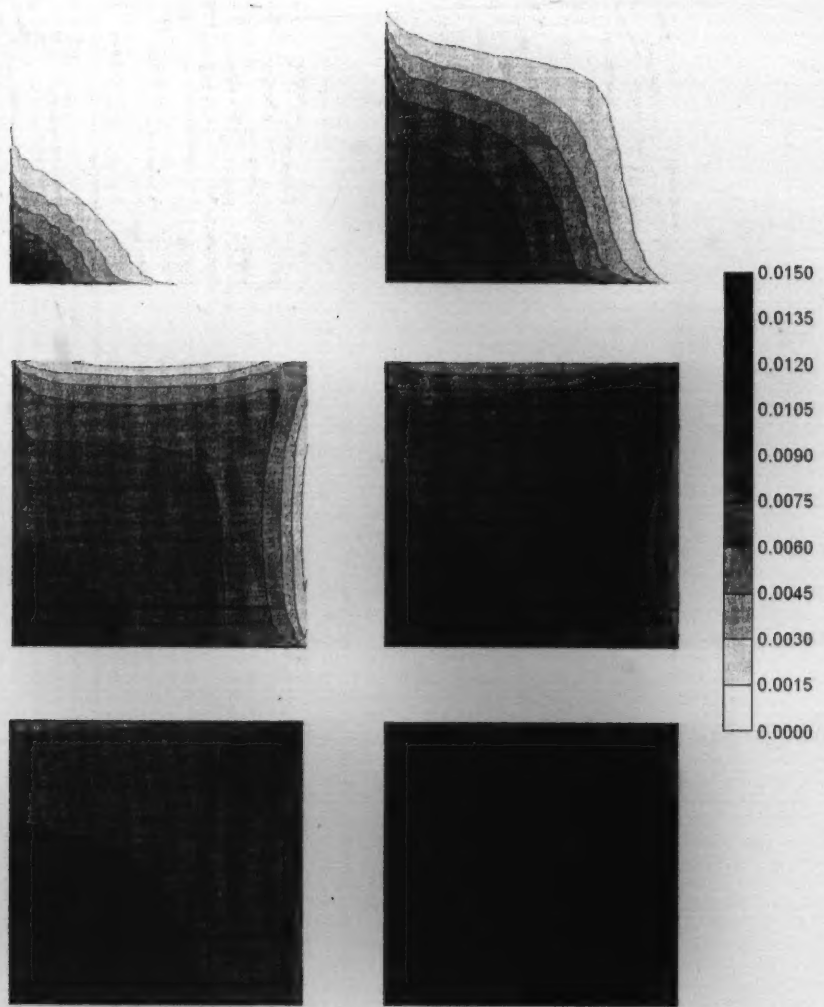

Figure 8.4: Contour plot of the molar fraction of paclitaxel on a regular lattice with a constant infusion of 0.01 molar fraction of the drug. The snapshots were taken at 0.00002, 0.00012, 0.00024, 0.00036, 0.00050, and 0.0012 minutes.

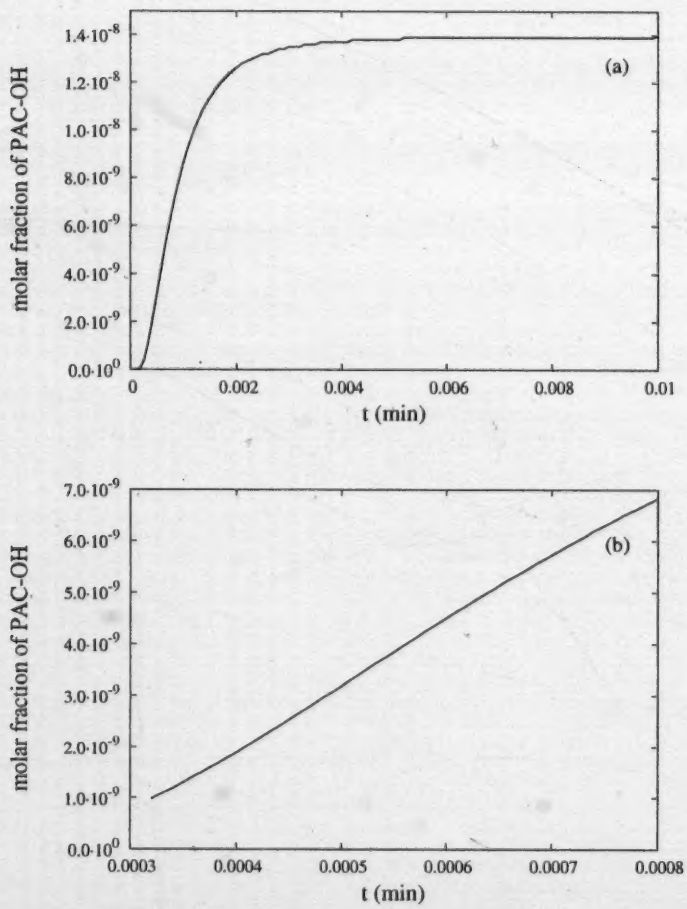

Figure 8.5: (a) The molar fraction of the metabolite PAC-OH as a function of time following a linear reaction on a regular lattice. (b) In the transient regime, the curve exhibits linear behaviour.

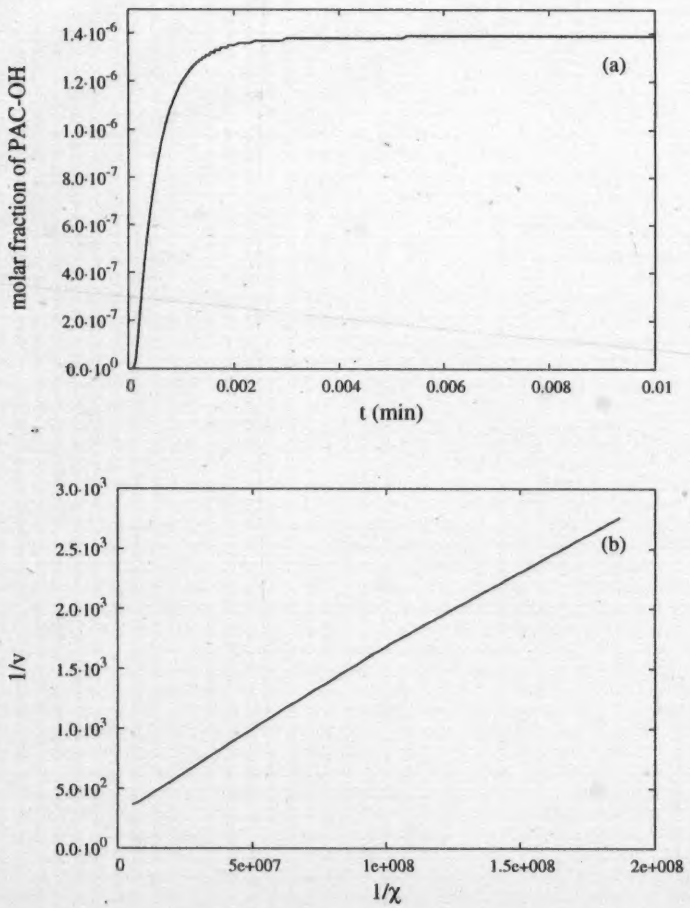

Figure 8.6: (a) The molar fraction of the metabolite PAC-OH as a function of time following a Michaelis-Menten reaction on a regular lattice. (b) Lineweaver-Burke plot.

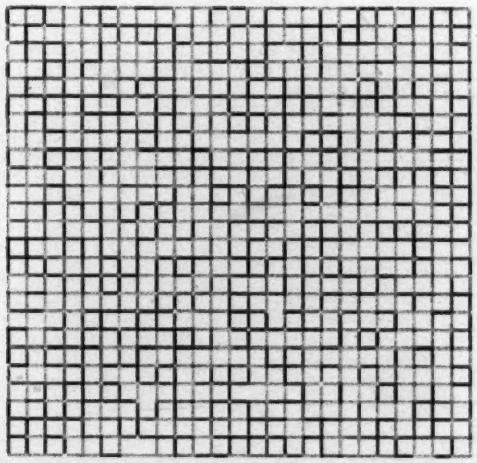

Figure 8.7: Lattice with random permeabilities. The shade of grey represents the permeability of the sinusoid (where a darker colour indicates a higher permeability), while the white hepatocyte sites have a constant permeability.

8.4.2 Random Permeability Lattice

The first type of heterogeneous lattice that was simulated was a random permeability lattice (Fig. 8.7). The vascular permeability κ was allowed to vary uniformly between $\kappa - \sigma$ and $\kappa + \sigma$, with $\kappa = r^2/8$. The value of σ was taken to be 0, 0.25κ, 0.5κ, 0.75κ, or κ. This lattice can mimic the effects of vascular irregularity in healthy livers (for smaller values of σ) or diseased livers (larger values of σ). The flow rate dropped slowly as σ was increased until a steep two-orders-of-magnitude drop when $\sigma = \kappa$ (Table 8.2). This suggests that relatively significant variations in sinusoid permeability may have only a small effect on liver transport and that healthy livers can support a reasonable amount of sinusoidal heterogeneity.

The reaction was first allowed to proceed in a linear manner with an infusion of 0.01 molar fraction of paclitaxel and a kinetic rate coefficient of $k = 10,000\ \text{min}^{-1}$. Figure 8.8 shows the molar fraction of the metabolite as a function of time when $\sigma = \kappa$. There are two regions in the transient regime: an initial fractal region exists up until

Table 8.2: Flow rate as a function of the σ for a random permeability lattice.

σ ($\times\kappa$)	Q ($\times 10^{-5}$ cm^3/min)
0	2.63
0.25	2.54
0.5	2.28
0.75	1.81
1	0.0684

$t = 0.01$ min and then transitions to a linear region that persists between $t = 0.02$ min and $t = 0.06$ min. The fractality of the initial rise is demonstrated by the power law dependence of k on time (Fig. 8.9), where $k(t)$ was calculated from

$$k(t) = \frac{\dot{\chi}(t)}{\chi(t)}, \tag{8.3}$$

where $\chi(t)$ is the molar fraction of the metabolite, PAC-OH. The value of the power exponent was equal to 1.762 ± 0.005 ($R^2 = 0.998$). Therefore, the heterogeneous lattice demonstrated fractal kinetics in the transient regime when the reaction proceeded according to linear kinetics.

When the reaction instead followed Michaelis-Menten kinetics, with $K_M = 2 \times 10^{-8}$ molar fraction and $v_{\max} = 10,000$ min^{-1}, the transient regime produced the dual behaviour predicted by the fractal Michaelis-Menten equation. The initial portion followed a power law increase in the molar fraction and then transitioned to a linear increase (Fig. 8.10). The power law exponent was equal to $X = 11.6 \pm 0.2$.

These results are consistent with those found for the fractal compartmental model for mibefradil in Chapter 5. The spatial evolution of the molar fraction of paclitaxel on the lattice shows the formation of islands of higher reaction rates (Fig. 8.11) as predicted by the fractal Michaelis-Menten theory.

The results presented above were for the extreme case of $\sigma = \kappa$. But are these

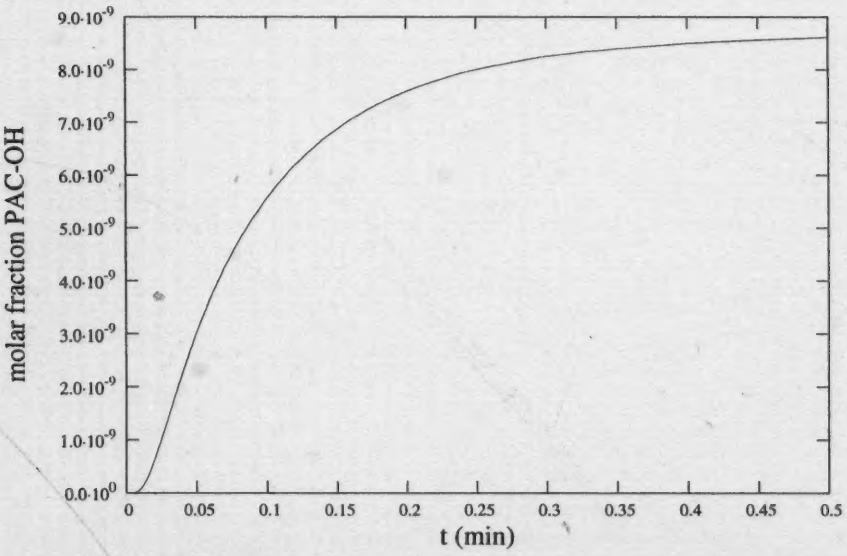

Figure 8.8: Molar fraction χ of the metabolite PAC-OH as a function of time for a linear reaction on a lattice with $\sigma = \kappa$.

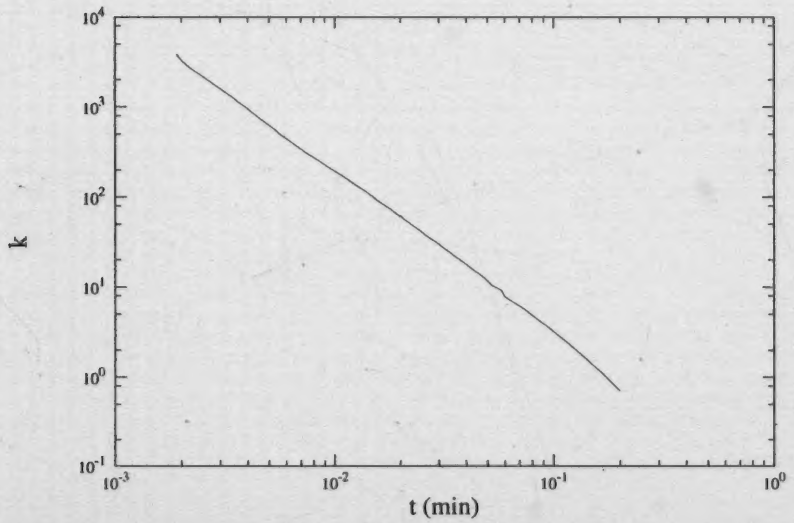

Figure 8.9: Initial fractal kinetics of the molar fraction χ of the metabolite PAC-OH showing the power law dependence of k on time for the linear reaction on a random permeability lattice.

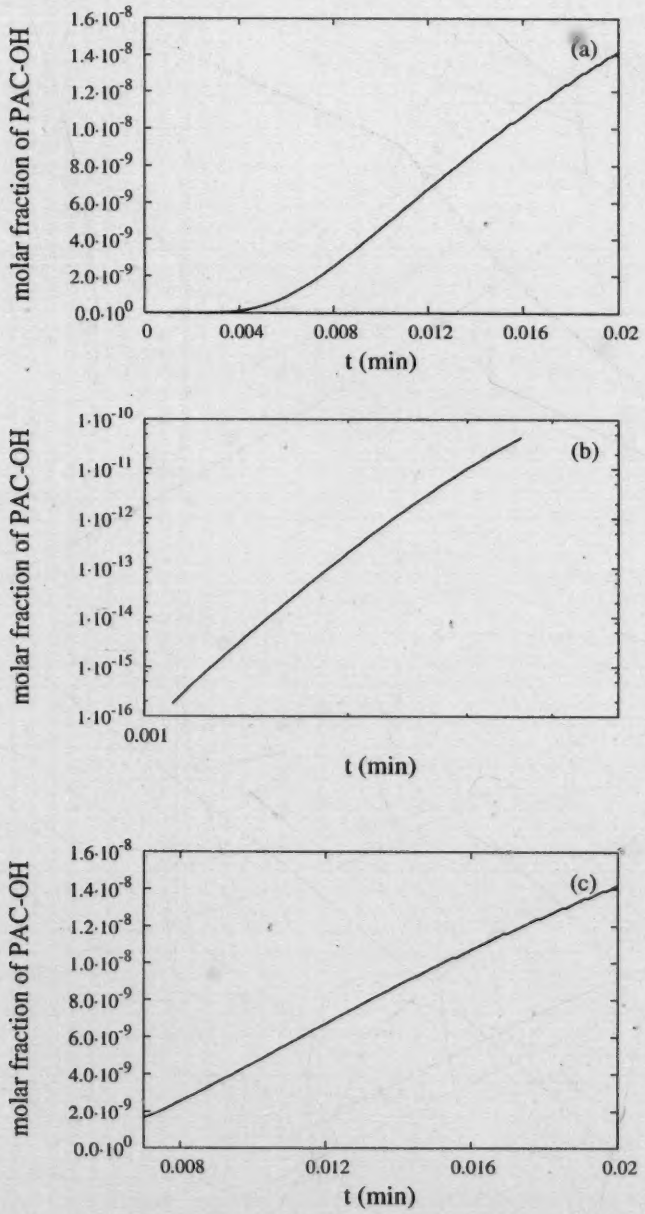

Figure 8.10: (a) Molar fraction of the metabolite PAC-OH as a function of time for a Michaelis-Menten reaction on a random permeability lattice with $\sigma = \kappa$. (b) The initial power law increase, which transitions to (c) a linear increase.

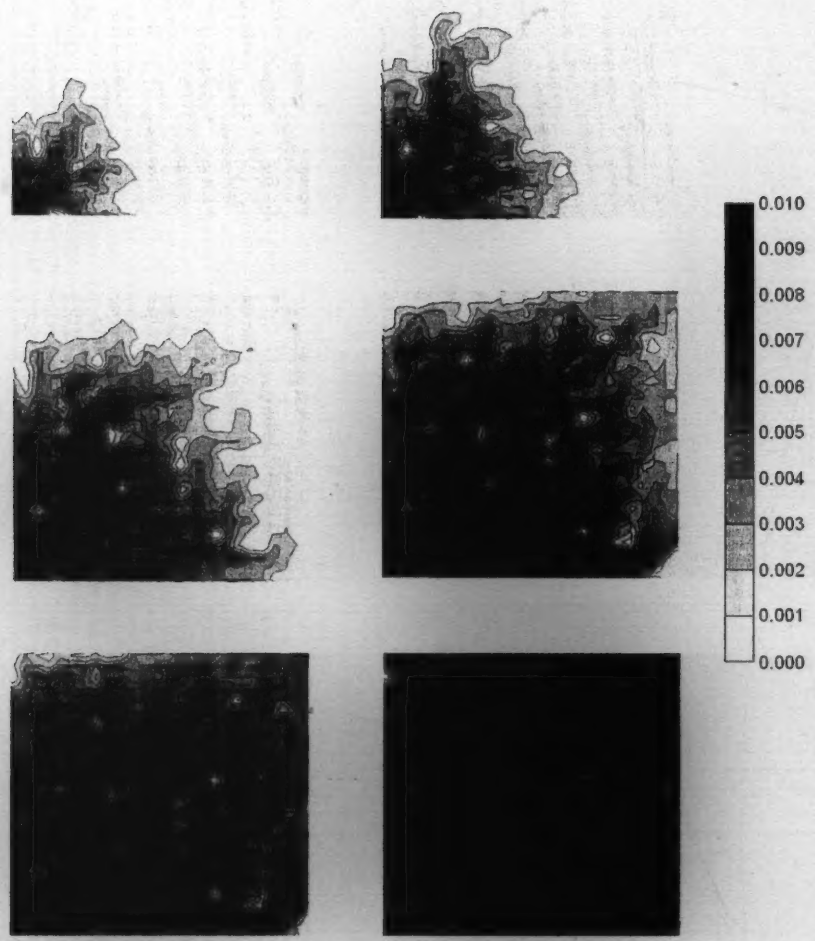

Figure 8.11: Contour plot of the molar fraction of paclitaxel on a lattice with random permeability ($\sigma = \kappa$), Michaelis-Menten kinetics ($K_M = 2 \times 10^{-8}$ and $v_{\max} = 10,000\ \text{min}^{-1}$, and a constant infusion of 0.01 molar fraction of the drug. The snapshots were taken at 0.006, 0.016, 0.036, 0.064, 0.1, and 0.4 minutes.

Table 8.3: Effect of the standard deviation σ of the permeability on the shape of the molar fraction of PAC-OH curve.

	Linear Reaction		MM Reaction	
σ	h	R^2	γ	R^2
0.25	1.594 (0.006)	0.998	6.56 (0.08)	0.998
0.50	1.615 (0.006)	0.998	6.83 (0.07)	0.999
0.75	1.641 (0.006)	0.998	7.12 (0.05)	0.999
1.0	1.762 (0.005)	0.998	11.6 (0.2)	0.998

results also observed for less heterogeneous lattices? Table 8.3 shows that the effect of increasing σ was to increase h in the linear case and to increase γ in the Michaelis-Menten case. Decreasing K_M in the Michaelis-Menten case resulted in a significantly higher production of the metabolite in the early regime and then a drop to lower steady state value (Fig. 8.12).

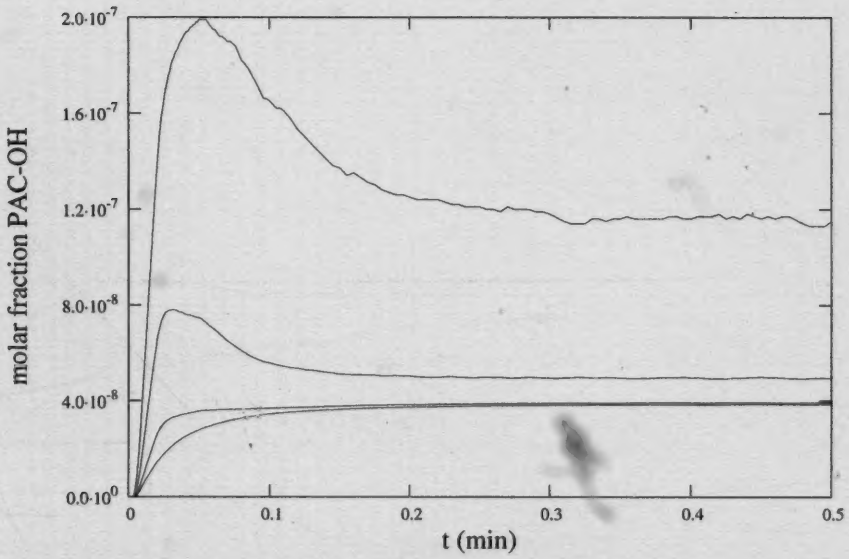

Figure 8.12: The effect of K_M on the Michaelis-Menten reaction on a random permeability lattice with $\sigma = \kappa$. From top to bottom: $K_M = 2 \times 10^{-14}$, $K_M = 2 \times 10^{-13}$, $K_M = 2 \times 10^{-12}$, and $K_M = 2 \times 10^{-8}$

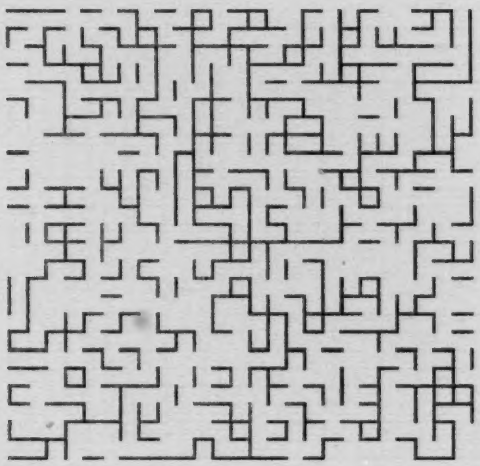

Figure 8.13: Lattice with $p = 0.4$. The grey bands are sinusoids and the white spaces are hepatocytes.

Table 8.4: Flow rate as a function of the σ for a percolation lattice.

p	Q ($\times 10^{-5}$ cm^3/min)
1	2.63
0.9	1.96
0.8	1.18
0.7	0.774
0.6	0.517

8.4.3 Percolation Lattice

The same simulations were run for a percolation lattice in which the sinusoids were removed randomly with probability p (Fig. 8.13). This lattice mimics the effects of damage and scarring that occurs with cirrhosis. In this case, the architecture of the liver is physically changed. The flow rate drops with p (Table 8.4), but not as drastically as in the random permeability case. Because p is at or above the percolation threshold, the pressure difference still drives flow through the lattice. However, some regions will receive poor or no flow, which should have an effect on the rate of the reaction.

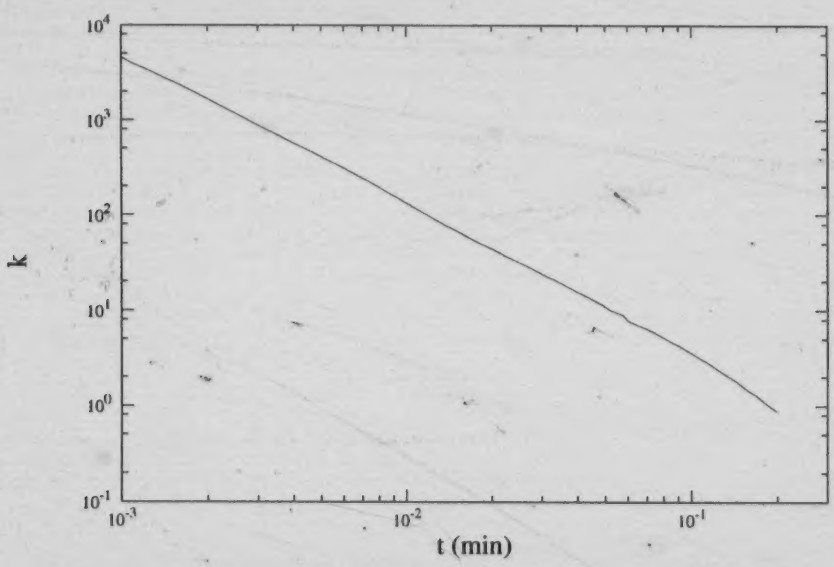

Figure 8.14: Initial fractal kinetics of the molar fraction χ of the metabolite PAC-OH showing the power law dependence of k on time for a linear reaction on a percolation lattice.

The simulation results were similar to those produced by the random permeability lattice. The linear reaction was best characterized by transient fractal kinetics (Fig. 8.14), while the Michaelis-Menten reaction showed evidence of fractal Michaelis-Menten kinetics (Fig. 8.15). The spatial evolution of the molar fraction of paclitaxel when $p = 0.6$ (near the percolation threshold) is shown in Fig. 8.16. In this case, the regions of reaction show a more homogeneous distribution of paclitaxel than in the random permeability lattice; however, there are now large areas with no metabolic activity at all.

These results suggest that even some permanent change in the tissue architecture produces significantly anomalous kinetics. The effect of changing the value of p is recorded in Table 8.5. In the linear case, there is little difference in the h values. In the Michaelis-Menten case, there is variation among the γ values, but with no consistent pattern.

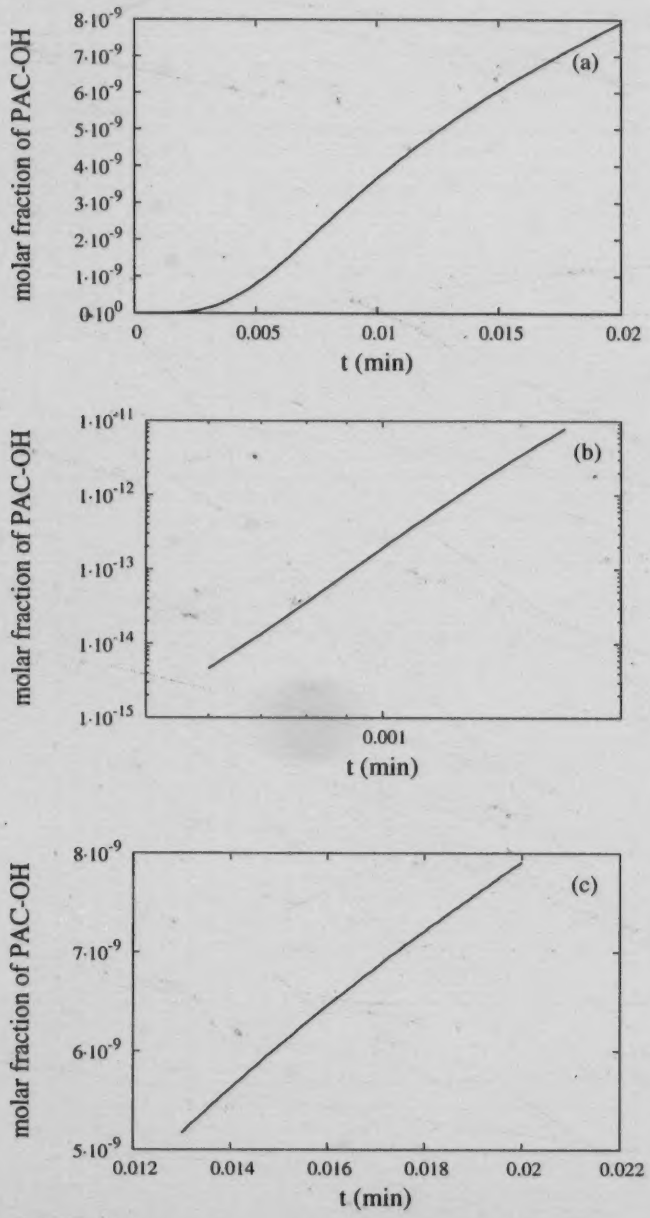

Figure 8.15: (a) Molar fraction of the metabolite PAC-OH as a function of time for a Michaelis-Menten reaction on a percolation lattice with $p = 0.6$. (b) The initial power law increase, which transitions to (c) a linear increase.

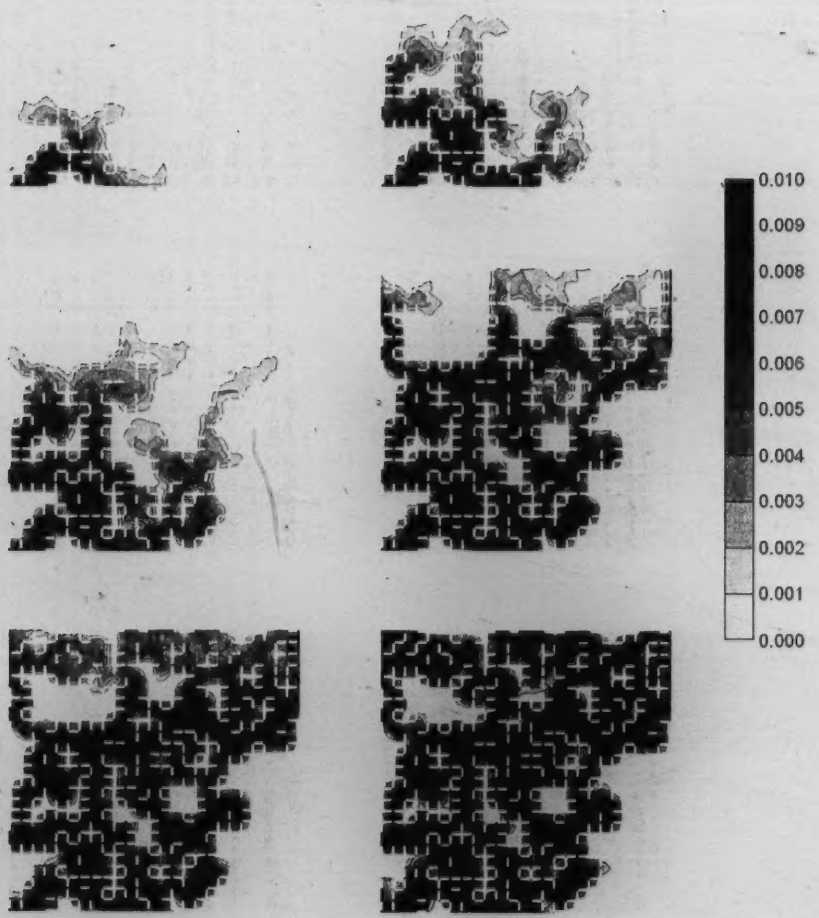

Figure 8.16: Evolution of the molar fraction of paclitaxel on a percolation lattice with probability $p = 0.6$ of each sinusoid being intact, at $t = 0.0004, 0.0012, 0.002, 0.0042, 0.008, 0.02$ min.

Table 8.5: Effect of p on the shape of the molar fraction of PAC-OH curve.

	Linear Reaction		MM Reaction	
p	h	R^2	γ	R^2
0.9	1.678 (0.009)	0.995	7.14 (0.10)	0.996
0.8	1.658 (0.007)	0.996	7.96 (0.09)	0.999
0.7	1.646 (0.009)	0.996	7.30 (0.05)	0.998
0.6	1.646 (0.009)	0.996	6.68 (0.10)	0.996

8.5 Conclusion

In this chapter, it was demonstrated that the aggregate behaviour of an ensemble of drug molecules as represented by a fractal compartment can be reproduced at the level of the functional unit of the organ. Because the behaviour at the smaller scale is similar to that at the whole organ scale, this is an example of scaling. Two types of heterogeneity were considered, corresponding to temporary and permanent damage to the liver tissue architecture. Both were shown to lead to fractal and fractal Michaelis-Menten kinetics under certain conditions, providing support for the theoretical predictions in Chapter 5 as well as the interpretation of the liver as an ensemble of islands of metabolic activity.

This work may be expanded in the future to model a percolation lattice with random permeability, a three-dimensional lattice, and the zonation of enzyme activity within the lobule. In addition, the dynamics of the liver architecture could be modeled such that the causes of liver damage and the subsequent regeneration are included.

Chapter 9

Conclusion

9.1 Summary

The main objective of the research presented in this thesis was to model the effects of spatial and temporal heterogeneity on drug processes occurring within the body. This was achieved using a combination of methodologies borrowed from physics (Table 9.1) and the development of new pharmacokinetic theory.

The first new methodology presented was a technique for fitting the parameters of a model to experimental data using a simulated annealing algorithm. The method performed comparably to commercial software, and because of its independence on the initial conditions, it was shown to be especially applicable to fractal compartmental models. Second, a stochastic model was developed using a random walk model with both short-term and long-term interactions between drug molecules. Finally, a physiologically-based

Table 9.1: Summary of models.

Model	Characteristics	Heterogeneity
Fractal Compartmental	Deterministic, Continuous	Spatial
CTRW	Stochastic, Discrete	Spatial, Temporal
Flow Network	Deterministic, Discrete	Spatial

network model was constructed for the liver functional unit and was able to reproduce the heterogeneous structure of both healthy and diseased livers using random and percolation lattices.

The main theoretical contribution of this thesis was the development of a fractal Michaelis-Menten equation to describe saturable, enzyme-mediated reactions occurring within heterogeneous and poorly-mixed environments. The model incorporates a fractal reaction order that can be naturally interpreted in terms of the anatomy and physiology of the liver. When incorporated into the compartmental framework, the fractal Michaelis-Menten theory provided an improved fit to data for the cardiac drug mibefradil. The theory of fractal kinetics under both simple and saturable conditions was supported by simulations using both the interacting random walk model and the physiologically-based network model.

Several mechanisms for generating and modeling concentration-time curves with long-time power law tails were proposed, including fractal Michaelis-Menten kinetics, Lévy-distributed trapping times, and the competition between two saturable processes.

To summarize, different methods from physics have been successfully applied to solve problems in pharmacokinetics and to extract additional information about the behaviour of pharmacokinetic systems.

9.2 Future Directions

The methods described in this thesis can be both expanded and applied to solve other problems in pharmacokinetics. For example, additional types of temporary trapping sites could be incorporated into the CTRW model to investigate the effect of reservoirs such as fat cells on the distribution of the drug at its target site. In addition, other types of distributions could be used to model the trapping times.

The theory of fractal compartments can be applied to other tissues in the body. For example, the kidney is responsible for the excretion of many drugs, and the venous and

arterial trees feeding the kidney as well as the network of tubules that remove the urine all approximate fractal trees. In addition, the branching nature of the bronchial tree suggests that it could be modeled by a fractal compartment. Furthermore, different types of tumours have been shown to have fractal structures.

Finally, a three-dimensional version of the flow network model could be constructed. Eventually, this type of model could be developed for the major organs in the body as well as for different types of tumours, and they could be all connected into a full-body physiologically-based pharmacokinetic model. By incorporating the specific anatomical and physiological characteristics of a given patient, such a model could be used to test the individual's response to different therapeutic regimes in a virtual, noninvasive environment.

Bibliography

[1] Available at `http://www.pharsight.com/winnonlin/`.

[2] Available at `http://www.boomer.org`.

[3] K. Abshagen, Eipel. C., M. D. Menger, and B. Vollmer. Comprehensive analysis of the regenerating mouse liver: An in vivo fluoresence microscopic and immunohistological study. *J. Surg. Res.*, 134:354–362, 2006.

[4] R. Advani, G. A. Fisher, B. L. Lum, J. Hausdorff, J. Halsey, M. Litchman, and B. I. Sikic. A phase I trial of doxorubicin, paclitaxel, and valspodar (PSC 833), a modulator of multidrug resistance. *Clin. Cancer Res.*, 7(5):1221–1229, 2001.

[5] R. A. Albanese, H. T. Banks, M. V. Evans, and L. K. Potter. Physiologically based pharmacokinetic models for the transport of trichloroethylene in adipose tissue. *Bull. Math. Biol.*, 64(1):97–131, 2002.

[6] S. Alexander, J. Bernasconi, W. R. Schneider, and R. Orbach. Excitation dynamics in random one-dimensional systems. *Rev. Mod. Phys.*, 53(2):175–198, 1981.

[7] S. Alexander and R. Orbach. Density of states on fractals: "fractons". *J. Phys. Lett.*, 43:L–625 – L–631, 1982.

[8] L.W. Anacker and R. Kopelman. Fractal chemical kinetics: simulations and experiments. *J. Chem. Phys.*, 81(12):6402–6403, 1984.

[9] L.W. Anacker and R. Kopelman. Steady-state chemical kinetics on fractals: segregation of reactants. *Phys. Rev. Lett.*, 58(4):289–291, 1987.

[10] L.W. Anacker, R. Kopelman, and J.S. Newhouse. Fractal chemical kinetics: reacting random walkers. *J. Stat. Phys.*, 36(5/6):591–602, 1984.

[11] J. Anderson, S. B. Osborn, R. W. Tomlinson, and M. A. Weinbren. Some applications of power law analysis to radioisotope studies in man. *Phys. Med. Biol.*, 8(3):287–295, 1963.

[12] J. C. Anderson, A. L. Babb, and M. P. Hlastala. A fractal analysis of the radial distribution of bronchial capillaries around large airways. *J. Appl. Physiol.*, 98(3):850–855, 2005.

[13] J. S. Aranda, E. Salgado, and A. Muñoz-Diosdado. Multifractality in intracellular enzymatic reactions. *J. Theor. Biol.*, 240:209–217, 2006.

[14] P. Argyrakis and R. Kopelman. Stirring in chemical reactions. *J. Phys. Chem.*, 93:225–229, 1989.

[15] I. M. Arias, editor. *The Liver: Biology and Pathology.* Lippincott Williams and Wilkins, Philadelphia, 4 edition, 2001.

[16] K. A. Bachmann and R. Ghosh. The use of in vitro methods to predict in vivo pharmacokinetics and drug interactions. *Curr. Drug Metab.*, 2(3):299–314, 2001.

[17] Kim Y. G. Kim S. H. Kim J. W. Kim T. Lee M. G. Bae S. K., Lee S. J. Interspecies pharmacokinetic scaling of oltipraz in mice, rats, rabbits and dogs, and prediction of human pharmacokinetics. *Biopharm. Drug Dispos.*, 26(3):99–115, 2005.

[18] P. Bak, C. Tang, and K. Wiesenfeld. Self-organized criticality. *Phys. Rev. A*, 38(1):364–374, 1988.

[19] F. Bardou, Bouchard, J.P., O. Emile, A. Aspect, and C. Cohen-Tannoudji. Subrecoil laser cooling and levy flights. *Phys. Rev. Lett.*, 72(2):203–206, 1994.

[20] F. Bartumeus, F. Peters, S. Pueyo, C. Marrase, and J. Catalan. Helical Levy walks: adjusting searching statistics to resource availability in microzooplankton. *Proc. Natl. Acad. Sci. U.S.A.*, 100(22):12771–12775, 2003.

[21] J. B. Bassingthwaighte and D. A. Beard. Fractal 15O-labeled water washout from the heart. *Circ. Res.*, 77(6):1212–1221, 1995.

[22] J. B. Bassingthwaighte, R. B. King, and S. A. Roger. Fractal nature of regional myocardial blood flow heterogeneity. *Circ. Res.*, 65:578–590, 1989.

[23] J.B. Bassingthwaighte, L. Liebovitch, and B.J. West. *Fractal Physiology.* Oxford University Press, Oxford, 1994.

[24] D. Ben-Avraham and S. Havlin. *Diffusion and Reactions in Fractals and Disordered Systems.* Cambridge University Press, Cambridge, UK, 2000.

[25] H. Berry. Monte Carlo simluations of enzyme reactions in two dimensions: fractal kinetics and spatial segregation. *Biophys. J.*, 83:1891–1901, 2002.

[26] M. V. Berry and Z. V. Lewis. On the Weierstrass-Mandelbrot fractal function. *Proc. R. Soc. Lond. A*, 370:459–484, 1980.

[27] E. Bhunchet and K. Wake. The portal lobule in rat liver fibrosis: a re-evaluation of the liver unit. *Hepatology*, 27:481–487, 1998.

[28] O. Biham, Z. F. Huang, O. Malcai, and S. Solomon. Long-time fluctuations in a dynamical model of stock market indices. *Phys. Rev. E*, 64(2 Pt 2):026101, 2001.

[29] M. Boguna and A. Corral. Long-tailed trapping times and Levy flights in a self-organized granular system. *Phys. Rev. Lett.*, 78(26):4950–4953, 1997.

[30] H. G. Boxenbaum. Pharmacokinetics tricks and traps: flip-flop models. *J. Pharm. Pharm. Sci.*, 1:90–91, 1998.

[31] T. Brown, K. Havlin, G. Weiss, J. Cagnola, J. Koeller, J. Kuhn, J. Rizzo, J. Craig, J. Phillips, and D. Von Hoff. A phase I trial of taxol given by a 6-hour intravenous infusion. *J. Clin. Oncol.*, 9(7):1261–1267, 1991.

[32] L. L. Brunton, editor. *Goodman and Gilman's The Pharmacological Basis of Therapeutics.* McGraw-Hill, New York, 11 edition, 2005.

[33] S. H. Bryant, S. A. Islam, and D. L. Weaver. The surface area of monomeric proteins: significance of power law behaviour. *Proteins*, 6(4):418–423, 1989.

[34] Alfred Burger. *Understanding Medications: What the Label Doesn't Tell You.* Oxford University Press, Oxford, UK, 1995.

[35] J. L. Cabrera and J. G. Milton. Human stick balancing: tuning Levy flights to improve balance control. *Chaos*, 14(3):691–698, 2004.

[36] D. Chappard, E. Legrand, B. Haettich, G. Chales, B. Auvinet, J. P. Eschard, J. P. Hamelin, M. F. Basle, and M. Audran. Fractal dimension of trabecular bone: comparison of three histomorphometric computed techniques for measuring the architectural two-dimensional complexity. *J. Pathol.*, 195(4):515–521, 2001.

[37] P. Chelminiak, J. M. Dixon, J. A. Tuszynski, and R. E. Marsh. Application of a random network with a variable geometry of links to the kinetics of drug elimination in healthy and diseased livers. *Phys. Rev. E*, 73(5 Pt 1):051912, 2006.

[38] P. Chelminiak, R. E. Marsh, J. A. Tuszyski, J. M. Dixon, and K. J. E. Vos. Asymptotic time dependence in the fractal pharmacokinetics of a two-compartment model. *Phys. Rev. E*, 72(3):031903, 2005.

[39] K Christensen, A Corral, V. Frette, J. Feder, and T. Jossang. Tracer dispersion in a self-organized critical system. *Phys. Rev. Lett.*, 77:107–110, 1996.

[40] E. Claridge, P. N. Hall, M. Keefe, and J. P. Allen. Shape and analysis for classification of malignant melanoma. *J. Biomed. Eng.*, 14(3):229–234, 1992.

[41] W. A. Colburn. Physiologic pharmacokinetic modeling. *J. Clin. Pharmacol.*, 28(8):673–677, 1988.

[42] A. Corana, M. Marchesi, C. Martini, and S. Ridella. Minimizing multimodal functions of continuous variables with the simulated annealing algorithm. *ACM Transactions on Mathematical Software*, 13:262–280, 1987.

[43] S. Cornell, M. Droz, and B. Chopard. Role of flutuations for inhomogeneous reaction-diffusion phenomena. *Phys. Rev. A*, 44(8):4826–4832, 1991.

[44] A. Cornish-Bowden. *Fundamentals of Enzyme Kinetics.* Portland Press, London, 1995.

[45] S. S. Cross, J. P. Bury, P. B. Silcocks, T. J. Stephenson, and D. W. Cotton. Fractal geometric analysis of colorectal polyps. *J. Pathol.*, 172(4):317–323, 1994.

[46] D. J. Cutler. A comment regarding mean residence times in non-linear systems. *Biopharm. Drug Dispos.*, 10(5):529–530, 1989.

[47] B. Damascelli, G. Cantu, F. Mattavelli, P. Tamplenizza, P. Bidoli, E. Leo, F. Dosio, A. M. Cerrotta, G. Di Tolla, L. F. Frigerio, F. Garbagnati, R. Lanocita, A. Marchiano, G. Patelli, C. Spreafico, V. Ticha, V. Vespro, and F. Zunino. Intraarterial chemotherapy with polyoxyethylated castor oil free paclitaxel, incorporated in albumin nanoparticles (ABI-007): Phase II study of patients with squamous cell carcinoma of the head and neck and anal canal: preliminary evidence of clinical activity. *Cancer*, 92(10):2592–2602, 2001.

[48] G. Darche, J. E. Grabenstetter, and P. H. Sammon. The use of parallel processing with dynamic gridding. *Source SPE Reservoir Simulation Symposium*, SPE 93023:1–10, 1983.

[49] G. De Vico, V. Peretti, and G. A. Losa. Fractal organization of feline oocyte cytoplasm. *Eur. J. Histochem.*, 49(2):151–156, 2005.

[50] T. G. Dewey and M. M. Datta. Determination of the fractal dimension of membrane protein aggregates using fluorescence energy transfer. *Biophys. J.*, 56(2):415–420, 1989.

[51] G. Drazer and D. H. Zanette. Experimental evidence of power-law trapping-time distributions in porous media. *Phys. Rev. E*, 60(5 Pt B):5858–5864, 1999.

[52] S.B. Duffell, S. Retout, and F. Mentre. The use of simulated annealing for finding optimal population designs. *Comput. Methods Programs Biomed.*, 69(1):25–35, 2002.

[53] A. Eftaxias, J. Font, A. Fortuny, F. Fabregat, and F. Stüber. Nonlinear kinetic paramter estimation using simluated annealing. *Comp. Chem. Eng.*, 21:1725–1733, 2002.

[54] P. J. Fadel, S. M. Barman, S. W. Phillips, and G. L. Gebber. Fractal fluctuations in human respiration. *J. Appl. Physiol.*, 97(6):2056–2064, 2004.

[55] J. Fuite, R. Marsh, and J. Tuszynski. Fractal pharmacokinetics of the drug mibefradil in the liver. *Phys. Rev. E*, 66(2 Pt 1):021904, 2002.

[56] J. Gabrielsson and D. Weiner. *Pharmacokinetic/Pharmacodynamic Data Analysis: Concepts and Applications.* Swedish Pharmaceutical Press, Stockholm, 2nd edition, 1997.

[57] E. Gaudio, S. Chaberek, A. Montella, L. Pannarale, S. Morini, G. Novelli, F. Borghese, D. Conte, and K. Ostrowski. Fractal and fourier analysis of the hepatic sinusoidal network in normal and cirrhotic rat liver. *J. Anat.*, 207(2):107–115, 2005.

[58] H. Gelderblom, J. Verweij, D. M. van Zomeren, D. Buijs, L. Ouwens, K. Nooter, G. Stoter, and A. Sparreboom. Influence of Cremophor EL on the bioavailability of intraperitoneal paclitaxel. *Clin. Cancer Res.*, 8(4):1237–1241, 2002.

[59] K. Gelmon, E. Eisenhauer, C. Bryce, A. Tolcher, L. Mayer, E. Tomlinson, B. Zee, M. Blackstein, E. Tomiak, J. Yau, G. Batist, B. Fisher, and J. Iglesias. Randomized phase II study of high-dose paclitaxel with or without amifostine in patients with metastatic breast cancer. *J. Clin. Oncol.*, 17(10):3038–3047, 1999.

[60] L. Gianni, C. M. Kearns, A. Giani, G. Capri, L. Vigano, A. Lacatelli, G. Bonadonna, and M. J. Egorin. Nonlinear pharmacokinetics and metabolism of paclitaxel and its pharmacokinetic/pharmacodynamic relationships in humans. *J. Clin. Oncol.*, 13(1):180–190, 1995.

[61] J. Gil-Garcia, M. Gimeno-Dominguez, and N. L. Murillo-Ferroll. The arterial pattern and fractal dimension of the dog kidney. *Histol. Histopathol.*, 7:563–574, 1992.

[62] W. R. Gillespie. Noncompartmental versus compartmental modelling in clinical pharmacokinetics. *Clin. Pharmacokinet.*, 20(4):253–262, 1991.

[63] J. R. Gillette. Factors affecting drug metabolism. *Ann. N. Y. Acad. Sci.*, 179:43–66, 1971.

[64] W.L. Goffe, G.D. Ferrier, and J. Rogers. Global optimization of statistical functions with simulated annealing. *Journal of Econometrics*, 60:65–99, 1994.

[65] A. L. Goldberger, L. A. Amaral, J. M. Hausdorff, PCh Ivanov, C. K. Peng, and H. E. Stanley. Fractal dynamics in physiology: alterations with disease and aging. *Proc. Natl. Acad. Sci. U.S.A.*, 99 Suppl 1:2466–2472, 2002.

[66] A. L. Goldberger and B. J. West. Applications of nonlinear dynamics to clinical cardiology. *Ann. N. Y. Acad. Sci.*, 504(4):195–213, 1987.

[67] C. A. Goresky. Uptake in the liver: the nature of the process. *Int. Rev. Physiol.*, 21:65–101, 1980.

[68] K. Gough, M. Hutchinson, O. Keene, B. Byrom, S. Ellis, L. Lacey, and J. McKellar. Assessment of dose proportionality: report from the statisticians in the pharmaceutical industry/pharmacokinetics UK joint working party. *Drug Inf. J.*, 29:1039–1048, 1995.

[69] P. Grassberger and I. Procaccia. Measuring the strangeness of strange attractors. *Physica*, 9D:189–208, 1983.

[70] H. Gray. *Anatomy of the Human Body.* Lea and Febiger, Philedelphia, 1918.

[71] S. Guichard, S. Arnould, I. Hennebelle, R. Bugat, and P. Canal. Combination of oxaliplatin and irinotecan on human colon cancer cell lines: activity in vitro and in vivo. *Anticancer Drugs*, 12(9):741–751, 2001.

[72] J. Habasaki, I. I. Okada, and Y. Hiwatari. Origins of the two-step relaxation and the boson peak in an alkali silicate glass studied by molecular-dynamics simulation. *Phys. Rev. E*, 52(3):2681–2687, 1995.

[73] R. D. Harkness. Changes in the liver of the rat after partial hepatectomy. *J. Physiol.*, 117:267–277, 1952.

[74] H.O. Hartley. The modified Gauss-Newton method for the fitting of nonlinear regression functions by least squares. *Technometrics*, 3:269–280, 1961.

[75] S. Havlin, R. Kopelman, R. Schoonover, and G. H. Weiss. Diffusive motion in a fractal medium in the presence of a trap. *Phys. Rev. A*, 43(10):5228–5232, 1991.

[76] J. Heidel and J. Maloney. An analysis of a fractal Michaelis-Menten curve. *J. Australian Math. Soc. Ser. B Applied Math.*, 41:410–422, 2000.

[77] A. Henningsson, M. O. Karlsson, L. Vigano, L. Gianni, J. Verweij, and A. Sparreboom. Mechanism-based pharmacokinetic model for paclitaxel. *J. Clin. Oncol.*, 19(20):4065–4073, 2001.

[78] K. Horsfield. Diameters, generations, and orders of branches in the bronchial tree. *J. Appl. Physiol.*, 68(2):457–461, 1990.

[79] T. M. Hu and W. L. Hayton. Allometric scaling of xenobiotic clearance: uncertainty versus universality. *AAPS PharmSci*, 3(4):E29, 2001.

[80] W. Huang, R. T. Yen, M. McLaurine, and G. Bledsoe. Morphometry of the human pulmonary vasculature. *J. Appl. Physiol.*, 81(5):2123–2133, 1996.

[81] M. T. Huizing, V. H. Misser, R. C. Pieters, W. W. ten Bokkel Huinink, C. H. Veenhof, J. B. Vermorken, H. M. Pinedo, and J. H. Beijnen. Taxanes: a new class of antitumor agents. *Cancer Invest.*, 13(4):381–404, 1995.

[82] C.A. Hunt, G.H. Givens, and Guzy S. Bootstrapping for pharmacokinetic models: visualization of predictive and parameter uncertainty. *Pharm. Res.*, 15(5):690–697, 1998.

[83] J. A. Jacquez. *Compartmental Analysis in Biology and Medicine.* BioMedware, Ann Arbor, 1996.

[84] C. Javanaud. The application of a fractal model to the scattering of ultrasound in biological media. *J. Acoust. Soc. Am.*, 86(2):493–496, 1989.

[85] S. Ji, P. Zeng, P. Wu, and E. J. Lee. Sampling schedule design towards optimal drug monitoring for individualizing therapy. *Comput. Methods Programs Biomed.*, 80:57–63, 2005.

[86] M. A. Jordon and L. Wilson. Microtubule polymerization dynamics, mitotic block, and cell death by paclitaxel at low concentrations. In G. Georg, T. Chen, I. Ojima, and D.M. Vyas, editors, *Taxane Anticancer Agents: Basic Science and Current Status.*, pages 138–153. ACS Symp. Series 583, The American Chemical Society, Washington, DC, 1995.

[87] M. O. Karlsson, V. Molnar, A. Freijs, P. Nygren, J. Bergh, and R. Larsson. Pharmacokinetic models for the saturable distribution of paclitaxel. *Drug Metab. Dispos.*, 27(10):1220–1223, 1999.

[88] C. M. Kearns, L. Gianni, and M. J. Egorin. Paclitaxel pharmacokinetics and pharmacodynamics. *Semin. Oncol.*, 22(3,Suppl 6):16–23, 1995.

[89] K. M. Keough, P. Hyam, D. A. Pink, and B. Quinn. Cell surfaces and fractal dimensions. *J. Microsc.*, 163:95–99, 1991.

[90] T. Y. Kim, D. W. Kim, J. Y. Chung, S. G. Shin, S. C. Kim, D. S. Heo, N. K. Kim, and Y. J. Bang. Phase I and pharmacokinetic study of Genexol-PM, a cremophor-free, polymeric micelle-formulated paclitaxel, in patients with advanced malignancies. *Clin. Cancer Res.*, 10(11):3708–3716, 2004.

[91] S. Kirkpatrick, C. Gelatt Jr., and M. Vecchi. Optimization by simulated annealing. *Science*, 220(4598):498–516, 1983.

[92] P. W. Klymko and K. Kopelman. Heterogeneous exciton kinetics: triplet naphthalene homofusion in an isotropic mixed crystal. *J. Phys. Chem.*, 86:3686–3688, 1982.

[93] P. W. Klymko and K. Kopelman. Fractal reaction kinetics: exciton fusion clusters. *J. Phys. Chem.*, 87:4565–4567, 1983.

[94] R. Kopelman. Rate processes on fractals: theory, simulations, and experiments. *J. Stat. Phys.*, 42(1/2):185–200, 1986.

[95] R. Kopelman. Fractal reaction kinetics. *Science*, 241:1620–1626, 1988.

[96] K. Kosmidis, V. Karalis, P. Argyrakis, and P. Macheras. Michaelis-Menten kinetics under spatially constrained conditions: application to mibefradil pharmacokinetics. *Biophys. J.*, 87(3):1498–1506, 2004.

[97] M. López-Quintela and J. Casado. Revision of the methodology in enzyme kinetics: a fractal approach. *J. Theor. Biol.*, 139:129–139, 1989.

[98] P. Lansky. A stochastic model for circulatory transport in pharmacokinetics. *Math. Biosci.*, 132(2):141–167, 1996.

[99] D. V. Lebedev, M. V. Filatov, A. I. Kuklin, A. Kh. Islamov, E. Kentzinger, R. Pantina, B. P. Toperverg, and V. V. Isaev-Ivanov. Fractal nature of chromatin organization in interphase chicken erythrocyte nuclei: DNA structure exhibits biphasic fractal properties. *FEBS Lett.*, 579(6):1465–1468, 2005.

[100] D.G. Levitt. PKQuest: a general physiologically based pharmacokinetic model. introduction and application to propanolol. *BMC Clin. Pharmacol.*, 2:1–21, 2002.

[101] R. H. Levy. Time-dependent pharmacokinetics. *Pharmacol. Ther.*, 17(3):383–397, 1982.

[102] L. S. Liebovitch, D. Scheurle, M. Rusek, and M. Zochowski. Fractal methods to analyze ion channel kinetics. *Methods*, 24(4):359–375, 2001.

[103] J. H. Lin. Dose-dependent pharmacokinetics: experimental observations and theoretical considerations. *Biopharm. Drug Dispos.*, 15(1):1–31, 1994.

[104] Computer Modelling Group Ltd. *STARS User's Guide: Advanced Process and Thermal Reservoir Simulator*. Computer Modelling Group Ltd., Calgary, AB, 2006.

[105] T. M. Ludden, S. L. Beal, and L. B. Sheiner. Comparison of the Akaike Information Criterion, the Schwartz criterion and the F test as guides to model selection. *J. Pharmacokinet. Biopharm.*, 22:431–445, 1994.

[106] P. Macheras. Carrier-mediated transport can obey fractal kinetics. *Pharm. Res.*, 12(4):541–548, 1995.

[107] P. Macheras. A fractal approach to heterogeneous drug distribution: calcium pharmacokinetics. *Pharm. Res.*, 13(5):663–670, 1996.

[108] P. Macheras and A. Iliadis. *Modeling in Biopharmaceutics, Pharmacokinetics, and Pharmacodynamics: Homogeneous and Heterogeneous Approaches.* Springer Science+Business Media, Inc., New York, 2006.

[109] I. Mahmood. Allometric issues in drug development. *J. Pharm. Sci.*, 88(11):1101–1106, 1999.

[110] I. Mahmood. Prediction of clearance in humans from in vitro human liver microsomes and allometric scaling. a comparative study of the two approaches. *Drug Metabol. Drug Interact.*, 19(1):49–64, 2002.

[111] I. Mahmood and J. D. Balian. Interspecies scaling: predicting clearance of drugs in humans. three different approaches. *Xenobiotica*, 26(9):887–895, 1996.

[112] H. Maier-Lenz, B. Hauns, B. Haering, J. Koetting, K. Mross, C. Unger, T. Bauknecht, A. du Bois, H. G. Meerpohl, N. Hollaender, and K. Diergarten. Phase I study of paclitaxel administered as a 1-hour infusion: toxicity and pharmacokinetics. *Semin. Oncol.*, 24(6 Suppl 19):S19–16–S19–19, 1997.

[113] B.B. Mandelbrot. *The Fractal Geometry of Nature.* W.H. Freeman, San Francisco, 1982.

[114] R. N. Mantegna and H. E. Stanley. Stochastic process with ultraslow convergence to a gaussian: The truncated Levy flight. *Phys. Rev. Lett.*, 73(22):2946–2949, 1994.

[115] A. H. Marcus. Power laws in compartmental analysis. Part I: A unified stochastic model. *Math. Biosci.*, 23:337–350, 1975.

[116] D. J. Marsh, J. L. Osborn, and Jr. Cowley, A. W. 1/f fluctuations in arterial pressure and regulation of renal blood flow in dogs. *Am. J. Physiol.*, 258(5 Pt 2):F1394–1400, 1990.

[117] R. E. Marsh and J. A. Tuszynski. Fractal Michaelis-Menten kinetics under steady state conditions: Application to mibefradil. *Pharm. Res.*, 23:2760–2767, 2006.

[118] M. L. Martins, G. Ceotto, S. G. Alves, C. C. Bufon, J. M. Silva, and F. F. Laranjeira. Cellular automata model for citrus variegated chlorosis. *Phys. Rev. E*, 62(5 Pt B):7024–7030, 2000.

[119] J. Masoliver, M. Montero, and G. H. Weiss. A continuous time random walk model for financial distributions. *Phys. Rev. E*, 67:0210513, 2003.

[120] B. R. Masters. Fractal analysis of the vascular tree in the human retina. *Ann. Rev. Biomed. Eng.*, 6:427–452, 2004.

[121] J. H. Matis and T. E. Wehrly. Compartmental models with multiple sources of stochastic variability: the one-compartment models with clustering. *Bull. Math. Biol.*, 46(6):651–664, 1981.

[122] J. H. Matis and T. E. Wehrly. Generalized stochastic compartmental models with Erlang transit times. *J. Pharmacokinet. Biopharm.*, 18(6):589–607, 1990.

[123] T. Matsumoto and M. Kawakami. The unit concept of hepatic parenchyma. A re-examination based on angioarchitectural studies. *Acta Pathol. Jpn.*, 32(S2):285–314, 1982.

[124] P. L. McCarty. Stoichiometry of biological reactions. *Prog. Water Tech.*, 7(1):157–172, 1975.

[125] A.W. Metropolis, M.N. Rosenbluth, and A.H. Rosenbluth. Equation of state calculations by fast computing machines. *J. Chem. Phys.*, 21:1087–1092, 1953.

[126] L. Michaelis and M. L. Menten. Die kinetik der invertinwirkung. *Biochem. Z.*, 49:333–369, 1913.

[127] F. Moal, D. Chappard, J. Wang, E. Vuillemin, S. Michalak-Provost, M. C. Rousselet, F. Oberti, and P. Cales. Fractal dimension can distinguish models and pharmacologic changes in liver fibrosis in rats. *Hepatology*, 36(4 Pt 1):840–849, 2002.

[128] B. Monsarrat, E. Mariel, S. Cros, M. Gares, D. Guenard, F. Gueritte-Voegelein, and M. Wright. Taxol metabolism. Isolation and identification of three major metabolites of taxol in rat bile. *Drug Metab. Dispos.*, 18(6):895–901., 1990.

[129] B.M. Monsarrat, E. Chatelut, I. Royer, P. Alvinerie, J. Dubois, Dezeuse A., H. Roche, S. Cros, M. Wright, and P. Canal. Modification of paclitaxel metabolism in a cancer patient by induction of cytochrome P450 3A4. *Drug Met. Disp.*, 26(3):229–233, 1998.

[130] E. W. Montroll and G. H. Weiss. Random walks on lattices. *J. Math. Phys.*, 6:167–181, 1965.

[131] T. Mori, Y. Kinoshita, A. Watanabe, T. Yamaguchi, K. Hosokawa, and H. Honjo. Retention of paclitaxel in cancer cells for 1 week in vivo and in vitro. *Cancer Chemother. Pharmacol.*, Eprint, 2006.

[132] K. Mross, N. Hollander, B. Hauns, M. Schumacher, and H. Maier-Lenz. The pharmacokinetics of a 1-h paclitaxel infusion. *Cancer Chemother. Pharmacol.*, 45(6):463–470, 2000.

[133] J. D. Murray. *Mathematical Biology.* Springer-Verlag, Berlin, 1989.

[134] S. E. Myrdal, K. C. Johnson, and P. S. Steyger. Cytoplasmic and intra-nuclear binding of gentamicin does not require endocytosis. *Hear. Res.*, 204(1-2):156–169, 2005.

[135] V. R. Nannan Panday, R. de Wit, J. H. Schornagel, M. Schot, H. Rosing, J. Lieverst, W. W. ten Bokkel Huinink, J. H. Schellens, and J. H. Beijnen. Pharmacokinetics of paclitaxel administered in combination with cisplatin, etoposide and bleomycin in patients with advanced solid tumours. *Cancer Chemother. Pharmacol.*, 44(4):349–353, 1999.

[136] S. Nawaratne, J. E. Brien, E. Seeman, R. Fabiny, J. Zalcberg, W. Cosolo, P. Angus, and D. J. Morgan. Relationships among liver and kidney volumes, lean body mass and drug clearance. *Br. J. Clin. Pharmacol.*, 46(5):447–452, 1998.

[137] J.A. Nelder and R. Mead. A simplex method for function minimization. *Computer Journal*, 7:308–313, 1965.

[138] J. S. Newhouse and R. Kopelman. Reaction kinetics on clusters and islands. *J. Chem. Phys.*, 85(11):6804–6806, 1986.

[139] J. S. Newhouse and R. Kopelman. Steady-state chemical kinetics on surface clusters and islands: segregation of reactants. *J. Phys. Chem.*, 92:1538–1541, 1988.

[140] J.P. Nolan. Numerical calculations of stable densities and distribution functions. *Commun. Statist. Stochastic Models*, 13:759–774, 1997.

[141] J.P. Nolan. Parameterizations and modes of stable distributions. *Stat. Prob. Lett.*, 38:187–195, 1998.

[142] J. Noolandi. Equivalence of multiple-trapping model and time-dependent random walk. *Phys. Rev. B*, 16:4474–4479, 1977.

[143] W. P. Norris, S. A. Tyler, and A. M. Brues. Retention of radioactive bone-seekers. *Science*, 128(3322):456–462, 1958.

[144] K. H. Norwich and S. Siu. Power functions in physiology and pharmacology. *J. Theor. Biol.*, 95(2):387–398, 1982.

[145] T. Ogihara, I. Tamai, and A. Tsuji. Application of fractal kinetics for carrier-mediated transport of drugs across intestinal epithelial membrane. *Pharm. Res.*, 15(4):620–625, 1998.

[146] T. Ohtsu, Y. Sasaki, T. Tamura, Y. Miyata, H. Nakanomyo, Y. Nishiwaki, and N. Saijo. Clinical pharmacokinetics and pharmacodynamics of paclitaxel: a 3-hour infusion versus a 24-hour infusion. *Clin. Cancer Res.*, 1(6):599–606, 1995.

[147] P. R. Painter. Rivers, blood and transportation networks. *Nature*, 408(6809):159; discussion 160, 2000.

[148] M. Palus, D. Novotna, and J. Zvelebil. Fractal rock slope dynamics anticipating a collapse. *Phys. Rev. E*, 70(3 Pt 2):036212, 2004.

[149] A. Patnaik, E. Warner, M. Michael, M. J. Egorin, M. J. Moore, L. L. Siu, P. M. Fracasso, S. Rivkin, I. Kerr, M. Litchman, and A. M. Oza. Phase I dose-finding and pharmacokinetic study of paclitaxel and carboplatin with oral valspodar in patients with advanced solid tumors. *J. Clin. Oncol.*, 18(21):3677–3689, 2000.

[150] B. Peng, A.V. Boddy, M. Cole, A.D. Pearson, E. Chatelut, H. Rubie, and D.R. Newell. Comparison of methods for the estimation of carboplatin pharmacokinetics in paediatric cancer patients. *Eur. J. Cancer*, 31(11):1804–1810, 1995.

[151] E. Pereira, J. M. Martinho, and M. N. Berberan-Santos. Photon trajectories in incoherent atomic radiation trapping as levy flights. *Phys. Rev. Lett.*, 93(12):120201, 2004.

[152] J. D. Powers. Statistical considerations in pharmacokinetic study design. *Clin. Pharmacokinet.*, 24(5):380–387, 1993.

[153] W.H. Press. *Numerical Recipes in C : The Art of Scientific Computing.* Cambridge University Press, New York, 1992.

[154] M. D. Purugganan. The fractal nature of RNA secondary structure. *Naturwissenschaften*, 76(10):471–473, 1989.

[155] A. M. Rappaport. Hepatic blood flow: morphologic aspects and physiologic regulation. *Int Rev Physiol.*, 21:1–63, 1980.

[156] A. Rescigno. Fundamental concepts in pharmacokinetics. *Pharmacol. Res.*, 35(5):363–390, 1997.

[157] A. Rescigno. Foundations of pharmacokinetics. *Pharmacol. Res.*, 42(6):527–538, 2000.

[158] D. Ristanovic, V. Nedeljkov, B. D. Stefanovic, N. T. Milosevic, M. Grgurevic, and V. Stulic. Fractal and nonfractal analysis of cell images: comparison and application to neuronal dendritic arborization. *Biol. Cybern.*, 87(4):278–288, 2002.

[159] E. K. Rowinsky, P. J. Burke, J. E. Karp, R. W. Tucker, D. S. Ettinger, and R. C. Donehower. Phase I and pharmacodynamic study of taxol in refractory acute leukemias. *Cancer Res.*, 49(16):4640–4647, 1989.

[160] E. K. Rowinsky, M. Wright, B. Monsarrat, G. J. Lesser, and R. C. Donehower. Taxol: pharmacology, metabolism and clinical implications. *Cancer Surv.*, 17:283–304, 1993.

[161] B. Rubin and W.L. Buchanan. A general purpose thermal model. *SPEJ*, 25:202–214, 1985.

[162] J. M. Ruijter, J. Markman, M. M. Hagoort, A. F. Moorman, and W. H. Lamers. Relative distance: the key to the shape of hepatic building blocks. *Image Anal. Sterol.*, 19:19–24, 2000.

[163] W. M. Saltzman. *Drug Delivery: Engineering Principles for Drug Therapy.* Oxford University Press, Oxford, 2001.

[164] M. N. Samtani, M. Schwab, P. W. Nathanielsz, and W. J. Jusko. Area/moment and compartmental modeling of pharmacokinetics during pregnancy: applications to maternal/fetal exposures to corticosteroids in sheep and rats. *Pharm. Res.*, 21(12):2279–92, 2004.

[165] P. Santini. Levy scaling in random walks with fluctuating variance. *Phys. Rev. E*, 61(1):93–99, 2000.

[166] M. A. Savageau. Development of fractal kinetic theory for enzyme-catalysed reactions and implications for the design of biochemical pathways. *Biosystems*, 47(1-2):9–36, 1998.

[167] R. Saxena, N. D. Theise, and J. M. Crawford. Microanatomy of the human liver - exploring the hidden interfaces. *Hepatology*, 30(6):1339–1346, 1999.

[168] N. Scafetta, V. Latora, and P. Grigolini. Levy scaling: the diffusion entropy analysis applied to dna sequences. *Phys. Rev. E*, 66(3 Pt 1):031906, 2002.

[169] H. E. Schepers, J. H. G. M. vanBeek, and J. B. Bassingthwaighte. Four methods to estimate the fractal dimension from self-affine signals. *IEEE Eng. Med. Biol.*, 11:57–64x71, 1992.

[170] S. Schnell and T. E. Turner. Reaction kinetics in intracellular environments with macromolecular crowding: simulations and rate laws. *Prog. Biophys. Mol. Biol.*, 85(2-3):235–260, 2004.

[171] M. Schulz, S. Trimper, and B. Schulz. Variations of the asset prices. *Phys. Rev. E*, 64(2 Pt 2):026104, 2001.

[172] R. Segev, M. Benveniste, E. Hulata, N. Cohen, A. Palevski, E. Kapon, Y. Shapira, and E. Ben-Jacob. Long term behavior of lithographically prepared in vitro neuronal networks. *Phys. Rev. Lett.*, 88(11):118102, 2002.

[173] A. Skerjanec, S. Tawfik, and Y. K. Tam. Mechanisms of nonlinear pharmacokinetics of mibefradil in chronically instrumented dogs. *J. Pharmacol. Exp. Ther.*, 278(2):817–825, 1996.

[174] A. Skerjanec, S. Tawfik, and Y. K. Tam. Nonlinear pharmacokinetics of mibefradil in the dog. *J. Pharm. Sci.*, 85(2):189–192, 1996.

[175] O. Soepenberg, A. Sparreboom, M. J. de Jonge, A. S. Planting, G. de Heus, W. J. Loos, C. M. Hartman, C. Bowden, and J. Verweij. Real-time pharmacokinetics guiding clinical decisions; phase i study of a weekly schedule of liposome encapsulated paclitaxel in patients with solid tumours. *Eur. J. Cancer*, 40(5):681–688, 2004.

[176] D. S. Sonnichsen, C. A. Hurwitz, C. B. Pratt, J. J. Shuster, and M. V. Relling. Saturable pharmacokinetics and paclitaxel pharmacodynamics in children with solid tumors. *J. Clin. Oncol.*, 12(3):532–538, 1994.

[177] A. Sparreboom, L. van Zuylen, E. Brouwer, W. J. Loos, P. de Bruijn, H. Gelderblom, M. Pillay, K. Nooter, G. Stoter, and J. Verweij. Cremophor EL-mediated alteration of paclitaxel distribution in human blood: clinical pharmacokinetic implications. *Cancer Res.*, 59(7):1454–1457, 1999.

[178] W. B. Spillman, J. L. Robertson, W. R. Huckle, B. S. Govindan, and K. E. Meissner. Complexity, fractals, disease time, and cancer. *Phys. Rev. E*, 70:061911, 2004.

[179] H. E. Stanley, L. A. Amaral, A. L. Goldberger, S. Havlin, PCh Ivanov, and C. K. Peng. Statistical physics and physiology: monofractal and multifractal approaches. *Physica A*, 270(1-2):309–324, 1999.

[180] H.E. Stanley, L.A.N. Amaral, P. Gopikrishnan, P. Ch. Ivanov, T.H. Keitt, and V. Plerou. Scale invariance and universality: organizing principles in complex systems. *Physica A*, 281:60–68, 2000.

[181] D. Stepenski, L. Kleinberg, and A. Hoffman. Bone as an effect compartment: models for upatke and release of drugs. *Clin. Pharmacokinet.*, 42(10):863–881, 2003.

[182] H. F. Teutsch. The modular microarchitecture of human liver. *Hepatology*, 42:317–325, 2005.

[183] H. F. Teutsch, D. Schuerfeld, and E. Groezinger. Three-dimensional reconstruction of parenchymal units in the liver of the rat. *Hepatology*, 29(2):494–505, 1999.

[184] C. C. Tisher and C. S. Wilcox. *Nephrology and Hypertension*. Lippincott Williams and Wilkins, Philadelphia, 4 edition, 1999.

[185] L. Tothfalusi, L. Endrenyi, and K. K. Midha. Scaling or wider bioequivalence limits for highly variable drugs and for the special case of Cmax. *Int. J. Clin. Pharmacol. Ther.*, 41(5):217–225, 2003.

[186] V. V. Uchaikin and G. G. Gusarov. Simulation of random vectors from three-dimensional spherically symmetric stable distributions. *J. Math. Sci.*, 93(4):591–599, 1999.

[187] L. van Zuylen, M. O. Karlsson, J. Verweij, E. Brouwer, P. de Bruijn, K. Nooter, G. Stoter, and A. Sparreboom. Pharmacokinetic modeling of paclitaxel encapsulation in cremophor EL micelles. *Cancer Chemother. Pharmacol.*, 47(4):309–318., 2001.

[188] L. van Zuylen, J. Verweij, and A. Sparreboom. Role of formulation vehicles in taxane pharmacology. *Invest. New Drugs*, 19(2):125–141., 2001.

[189] P. Veng-Pedersen. Stochastic interpretation of linear pharmacokinetics: a linear system analysis approach. *J. Pharm. Sci.*, 80(7):621–631, 1991.

[190] P. Veng-Pedersen. Noncompartmentally-based pharmacokinetic modeling. *Adv. Drug Deliv. Rev.*, 48(2-3):265–300, 2001.

[191] A. Wax, C. Yang, V. Backman, K. Badizadegan, C. W. Boone, R. R. Dasari, and M. S. Feld. Cellular organization and substructure measured using angle-resolved low-coherence interferometry. *Biophys. J.*, 82(4):2256–2264, 2002.

[192] E. R. Weibel. Fractal geometry: a design principle for living organisms. *Am. J. Physiol.*, 261(6 Pt 1):L361–369, 1991.

[193] M. Weiss. Use of gamma distributed residence times in pharmacokinetics. *Eur. J. Clin. Pharmacol.*, 25(5):695–702, 1983.

[194] M. Weiss. Drug metabolite kinetics: noncompartmental analysis. *Br. J. Clin. Pharmacol.*, 19(6):855–856, 1985.

[195] M. Weiss. A note on the interpretation of tracer dispersion in the liver. *J. Theor. Biol.*, 184(1):1–6, 1997.

[196] M. Weiss. The anomalous pharmacokinetics of amiodarone explained by nonexponential tissue trapping. *J. Pharmacokinet. Biopharm.*, 27(4):383–396, 1999.

[197] R. Weron. Levy-stable distributions revisited: tail index 2 does not exclude the Levy-stable regime. *Int. J. Mod. Phys. C*, 12(2):209–223, 2001.

[198] P. H. Wiernik, E. L. Schwartz, A. Einzig, J. J. Strauman, R. B. Lipton, and J. P. Dutcher. Phase I trial of taxol given as a 24-hour infusion every 21 days: responses observed in metastatic melanoma. *J. Clin. Oncol.*, 5(8):1232–1239, 1987.

[199] P. H. Wiernik, E. L. Schwartz, J. J. Strauman, J. P. Dutcher, R. B. Lipton, and E. Paietta. Phase I clinical and pharmacokinetic study of Taxol. *Cancer Res.*, 47(9):2486–2493, 1987.

[200] M. E. Wise. The evidence against compartments. *Biometrics*, 27:262, 1971.

[201] M. E. Wise. Interpreting both short- and long-term power laws in physiological clearance curves. *Math. Biosci.*, 20:327–337, 1974.

[202] M.E. Wise, S.B. Osborn, J. Anderson, and R.W.S. Tomlinson. A stochastic model for turnover of radiocalcium based on the observed power laws. *Math. Biosci.*, 2:199–224, 1968.

[203] N. Xu and J. H. Xu. The fractal dimension of EEG as a physical measure of conscious human brain activities. *Bull. Math. Biol.*, 50(5):559–565, 1988.

[204] L. Yung, Y. Huang, P. Lessard, G. Legname, E. T. Lin, M. Baldwin, S. B. Prusiner, C. Ryou, and B. J. Guglielmo. Pharmacokinetics of quinacrine in the treatment of prion disease. *BMC Infect. Dis.*, 4:52, 2004.

[205] J.-Y. Zhu, X.-S. Leng, D. Nan, G.-Y. Qi, and R.-Y. Du. Measurement of liver volume and its clinical significance in cirrhotic portal hypertension. *World Journal of Gastroenterology*, 5(6):525–526, 1999.

[206] V. M. Zolotarev. On representation of densities of stable laws by special functions. *Theory Probab. Appl.*, 39:354–362, 1995.

Appendix A

Fractals

A.1 Definition

In the past century, the concept of fractals has been developed to describe spatial or temporal phenomena that are continuous but not differentiable. The term *fractal* was coined by Benoît Mandelbrot [113] in 1975 from the latin word *fractus*, or "fragmented". Fractals are typically characterized by roughness on all scales, which can lead to properties like self-similarity, scaling, and a fractal dimension. Therefore, they are useful tools for modeling disordered systems [24]. Fractals can be mathematical or natural entities, and they are generally characterized by three properties: they are self-similar over many scales, they can be generated by an iterative process, and their fractal dimension is not equal to the Euclidean dimension.

An object is self-similar if it is invariant under both translation and dilation, such that the smaller parts resemble the structure of the whole. Euclidean objects are only invariant under translation. For example, when a circle is magnified, it begins to appear more and more like a straight line. With fractal objects, however, continually increasing the magnification simply reveals more and more fine structure that resembles that of the whole. Not all self-similar objects are fractal, however, such as squares and triangles.

If a property $L(r)$ is measured at resolution r and then compared to the value of the

property at resolution ar, it is said to possess *self-similarity* if

$$L(ar) = kL(r), \tag{A.1}$$

where k is a proportionality constant. The solution to Eq. (A.1) is the *scaling* relationship

$$L(r) = (ar)^{\alpha}, \tag{A.2}$$

where α is the scaling exponent and a is a constant. This equation expresses how the value of the property depends on the measurement resolution.

The scaling relationship has the form of a power law and thus exhibits some special properties. It gives a straight line with slope α when plotted on a double-logarithmic plot since

$$\log L(r) = \alpha \log(r) + \log A. \tag{A.3}$$

Due to the dependence on the resolution, power laws do not single out any particular value, unlike the mean of the Gaussian distribution. In addition, small irregularities at small scales are reproduced as large irregularities at larger scales, and thus the variance may also not exist. If different variables are scaled by different factors, the fractal is said to be *self-affine* [169].

Fractals can also exist in time. In this case, the fluctuations of the value of a variable as a function of time will resemble each other when examined over different time scales. The time series is said to be generated by a fractal process.

A deterministic fractal is a mathematical entity that is exactly self-similar over a theoretically infinite range. A statistical (or random) fractal is only self-similar *on average* and its elements are generated from a probability distribution rather than through an exact deterministic law. For statistical fractals, it is the distribution of the measurement

or property that is the same at different scales:

$$\text{PDF}\left[L(ar)\right] = \text{PDF}\left[kL(r)\right], \tag{A.4}$$

where PDF[x] refers to the probability distribution function for the value x. In addition to not being Euclidean, natural fractals cannot be strictly fractal, and hence statistical fractals are most useful in modeling natural phenomena. Although there will always be a lower and an upper cutoff for which the self-similarity of a natural object or process holds, these cutoffs may be separated by several orders of magnitude.

A.2 Examples

The Koch curve and Sierpinski gasket, examples of deterministic fractals, are shown in Figures A.2 and A.2, respectively. They can be generated through an iterative process by successively applying a generator to an initiator. The initiator can be replaced by smaller and smaller version of the generator (as in the case of the Koch curve), or it can be assembled into larger and larger versions of itself (as in the case of the Sierpinski gasket).

The initiator of the Koch curve is a straight line. The generator is formed by dividing the line into three equal segments, then removing the middle segment and replacing it by two copies that point upwards along an equilateral triangle. During an iteration, each line segment is replaced by smaller and smaller copies of the generator. If the lengths of the three segments are not equal but instead are randomly chosen at each iteration, a statistical Koch curve is created.

The initiator for the Sierpinski gasket is a solid equilateral triangle. Each successive step is formed by the union of three copies of the current object, resulting in a new object that resembles the previous one but is twice the size. The gasket can also be formed by starting with a solid triangle, removing the middle triangle, and then repeating iteratively for all remaining triangles.

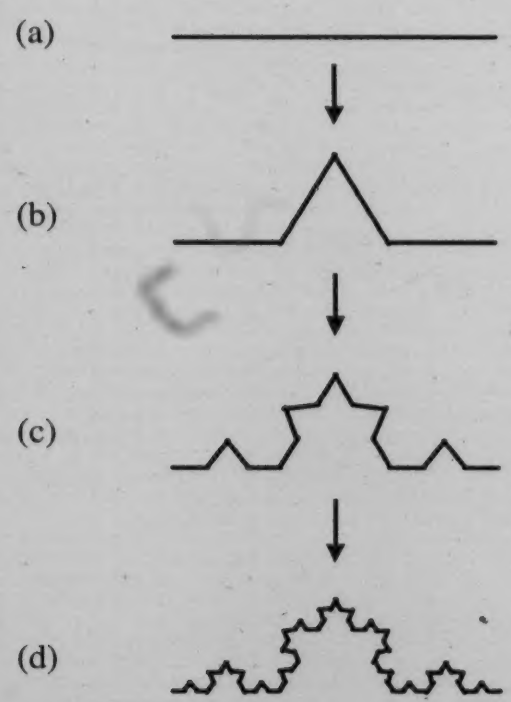

Figure A.1: The Koch curve. The initiator is shown in (a) and the generator is shown in (b). Configurations (c) and (d) are formed by replacing every line segment by successively smaller copies of the generator.

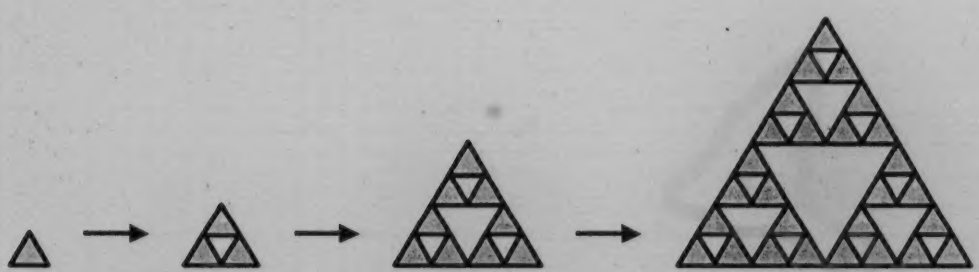

Figure A.2: The Sierpinski gasket. To generate the next iteration, three copies of the object are arranged to form a figure that is similar in shape but twice the size.

An example of a fractal time series is the Weierstrass-Mandelbrot function [113]:

$$W(t) = \sum_{n=-\infty}^{\infty} \frac{\left(1 - e^{ib^n t}\right) e^{i\phi_n}}{b^{(2-d)n}}, \tag{A.5}$$

where $1 < d < 2$, b is a constant determining how much of the curve is visible for a given range of t, and ϕ_n is an arbitrary phase. This function is continuous but has no derivative at any point nor a characteristic scale. Setting $\phi_n = 0$ and taking only the real part gives [26]

$$C(t) = \sum_{n=-\infty}^{\infty} \frac{1 - \cos(b^n t)}{b^{(2-d)n}}. \tag{A.6}$$

Figure A.3 shows the shape of Eq. (A.6) for two different values of d. For values close to $d = 1$, the fluctuations about the trend line are small, but as d approaches 2, the fluctuations become more pronounced. Figure A.4 shows the Weierstrass-Mandelbrot function plotted over two different time scales. The curves are self-affine since they are superimposable if the coordinates t and C are scaled by different factors. By choosing a random phase ϕ_n over the interval $(0, 2\pi)$, the equivalent statistical fractal can be generated [26].

A.3 The Fractal Dimension

Different definitions for the fractal dimension have been developed to quantify the irregularity or complexity of an object or process. The *similarity dimension* d_s describes the number N of original curves that fit into the curve when it is magnified by a factor F. For Euclidean objects,

$$N = X^D. \tag{A.7}$$

For deterministic fractal objects, the relation is

$$N = X^{d_s}, \tag{A.8}$$

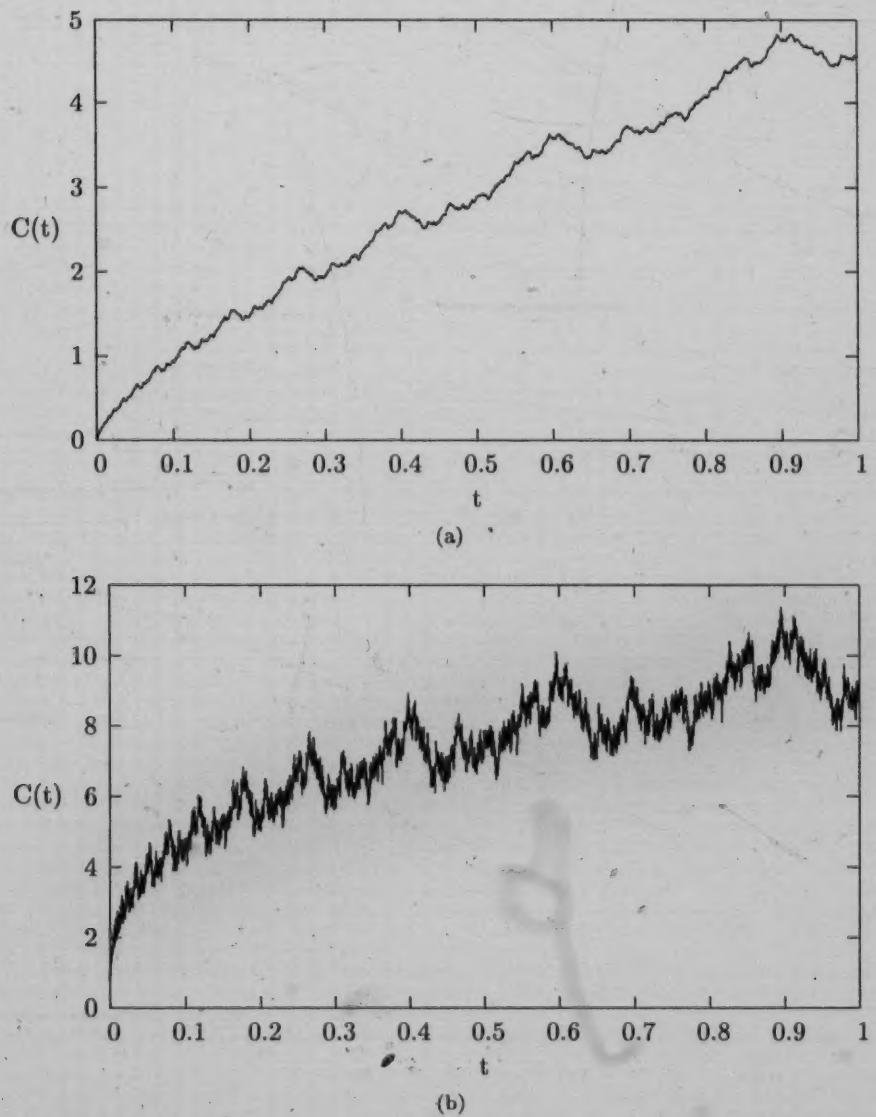

Figure A.3: The Weierstrass-Mandelbrot function $C(t)$ with $b = 1.5$ and $-1000 \leq n \leq 1000$. (a) $D = 1.3$. (b) $D = 1.7$.

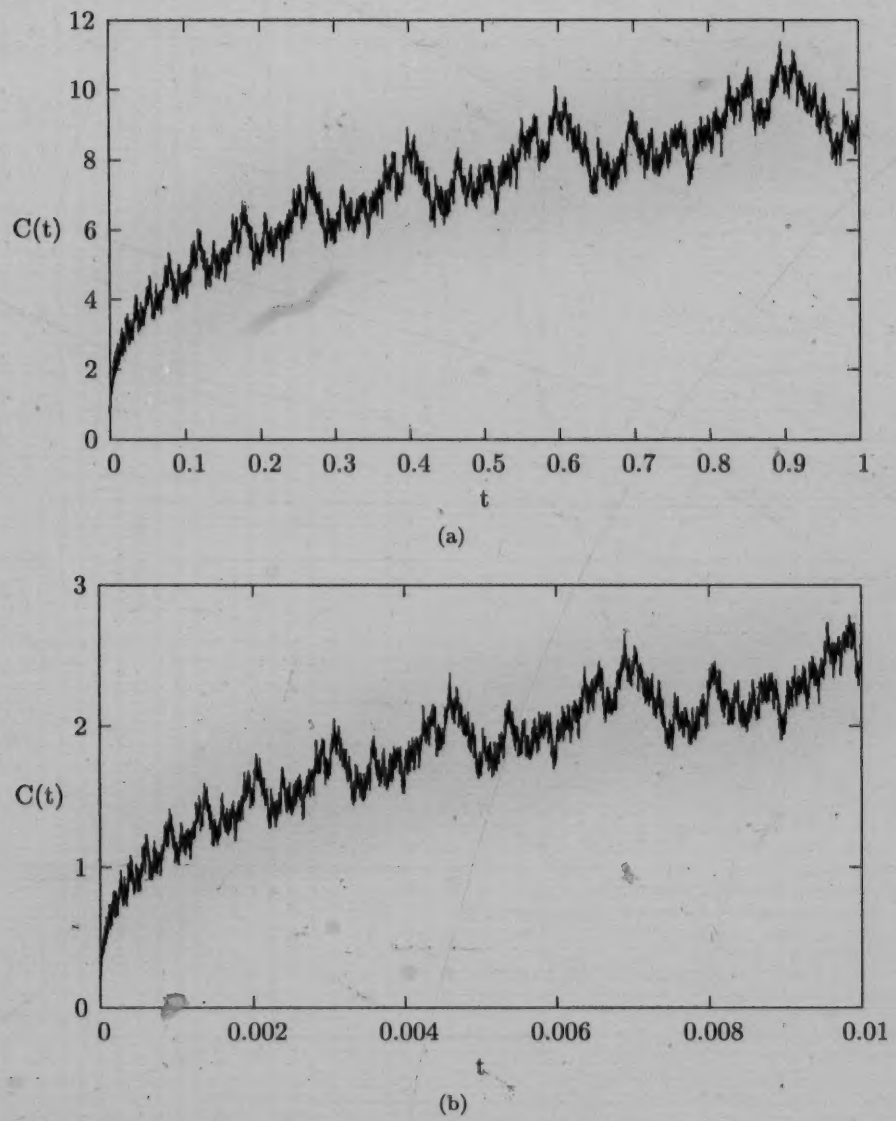

Figure A.4: The Weierstrass-Mandelbrot function $C(t)$ with $b = 1.5$, $D = 1.7$, and $-1000 \leq n \leq 1000$. (a) $0 \leq t \leq 1$. (b) $0 \leq t \leq 0.01$.

where d_s can take non-integer values. Rearranging gives

$$d_s = \frac{\log N}{\log F}. \tag{A.9}$$

When the Koch curve is enlarged by a factor of 3, the new curve contains 4 of the original curves and therefore $d_s = 1.26$. Therefore, the Koch curve is a fractal with embedding space $D = 2$, topological dimension $d_T = 1$, and similarity dimension $d_s = 1.26$. It is more dense than a one-dimensional object but less dense than a two-dimensional one, and the self-similarity dimension describes the ability of a line to fill an area of space. For the Sierpinski gasket, when the object is enlarged by a factor of 2, it contains three of the original curves, and thus $d_s \doteq 1.58$.

The fractal dimension can also be calculated from the scaling relationship, since [23]

$$d_f = \begin{cases} 1-\alpha & \text{for 1D} \\ 2-\alpha & \text{for 2D.} \\ 3-\alpha & \text{for 3D} \end{cases} \tag{A.10}$$

in Eq. (A.2).

Because the similarity dimension can only be calculated for deterministic fractals, a more general fractal dimension called the Hausdorff-Besicovitch dimension [69], d_H, has been developed. It is also referred to as the capacity dimension or the *fractal dimension* d_f. In fact, Mandelbrot's formal definition of a fractal was a set for which the Hausdorff-Besicovitch dimension strictly exceeds the topological dimension [113]. It is calculated as

$$d_f = d_H \equiv \lim_{r \to 0} \frac{\log N(r)}{\log\left(\frac{1}{r}\right)}, \tag{A.11}$$

where $d_T \leq d_f \leq D$, N is the minimum number of balls of radius r required to cover the object [69]. For deterministic fractals, $d_f = d_s$. The fractal dimension is a summary statistic that measures the overall complexity of an object or process. As such, it is

an important descriptor when used in conjunction with other measures. The fractal dimension of a statistical fractal is the same as that for its deterministic counterpart. For a temporal series, the fractal dimension describes the relationship between signal variance and the time scale [169].

If a group of objects or curves are characterized by the same exponent, they may fall into a universality class, which suggests commonality in their underlying microscopic mechanisms [180]. On the other hand, an object or process may not be described by a unique fractal dimension but rather a set of fractal dimensions. This is called multifractality, and multifractal phenomena are typically associated with systems governed by random multiplicative processes [179].

A.4 Fractals in Anatomy and Physiology

Anatomy is the branch of morphology that deals with the structure of organisms, and physiology is the branch of biology that deals with the function and activities of those structures. Many anatomical structures have fractal characteristics, and a wide range of fractal processes have been identified in physiology.

One of the most prominent fractal structures in the body is the dichotomously branching tree (Fig. A.4), whose vessels become successively shorter and narrower to most effectively their embedding space. Such a pattern is found in the blood vessels supplying the heart [22], lung [80], liver [57], kidney [61], and retina [120] as well as in the branches of the bronchial tree [12, 78] and the dendrite arbors of neurons [158]. It has even been suggested that fractal geometry such as the hierarchical tree is a biological design principle that maximizes efficiency and functioning [192].

Fractal geometry has also proven to be an appropriate tool for measuring the irregularity and complexity of tissues over many scales, from the organization of cells at the organ and bone level [36, 57] down to the surface of cells [89] and the distribution of protein aggregates in the membrane [50], the organization of the cytoplasm [49, 191]

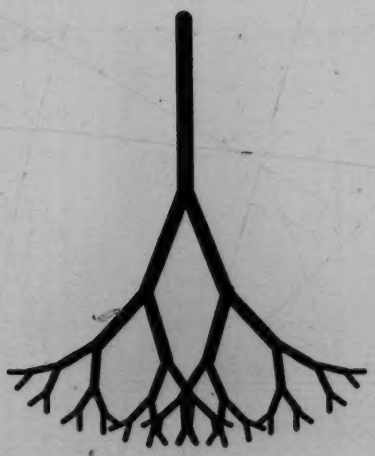

Figure A.5: A fractal tree with dichotomous branching. At each level, both the radius and the length of the branch are reduced.

and the nucleus [99], and the structure of individual proteins [33] and RNA [154]. Furthermore, fractals have been found to characterize the shape of tumours [45, 40]. The fractal dimension may even be related to the severity of disease or injury of a tissue. For example, Moal et al. [127] found that the fractal dimension of the liver increases with increasing fibrosis, and Spillman et al. [178] used the fractal dimension to characterize the level of malignancy of a cancer.

Examples of statistical fractals in physiology include ion channel kinetics [102], regulation of renal blood pressure and flow [116], fluctuations in the EEG signal [203] and the heartbeat [66], and the volume and duration of consecutive breaths [54]. These time series are characterized by long-range correlations, which may contribute to the adaptability necessary for the health of an individual. In fact, the fractal dimension may prove to be a quantitative tool for assessing an individual's level of risk for a particular disease, monitoring the individual's health, and forecasting outcomes [65]. Thus, disease or a physiologic "disorder" may in fact be related to an increase in mathematical order and a decrease in the fractal characteristics of the system. Finally, because all of the above examples are natural objects and phenomena, their fractal characteristics only exist over

a finite size or time scale.